Non-Equilibrium Phenomena in Graphene

Submitted by Samuel Martyn Hornett to the University of Exeter as
a thesis for the degree of Doctor of Philosophy in Physics
April, 2013

This thesis is available for Library use on the understanding that it is copyright material and that no quotation from the thesis may be published without proper acknowledgement.

I certify that all material in this thesis which is not my own work has been identified and that no material has previously been submitted and approved for the award of a degree by this or any other University.

Samuel Martyn Hornett
April, 2013

Abstract

Graphene has displayed much promise as an electrical conductor and as a optical material. To date there is a large body of literature dedicated to the equilibrium properties of graphene. In this thesis the properties of graphene out of equilibrium are probed. Through combined optical and transport measurements the behaviour of hot electrons are probed at temperatures over five orders of magnitude from 50mK to 2000K. This wide range of temperatures allows access to the behaviour of quantum corrections at the lowest temperatures to the highest energy phonon modes. From ultrafast femtosecond laser pulses to steady state heating from an electric field the cooling of hot electron populations through coupling to various phonon modes in the graphene and the substrate are explored. Additionally the effect of an electric field on the weak localisation correction to the conductivity was separated from heating effects using applied magnetic fields combined with careful modelling of the heat transport properties of the graphene. Finally the desorption dynamics of oxygen bound to the surface are shown using a combination of transport and two pulse correlation technique using an ultrafast laser. Surprisingly the cooling of hot carriers in graphene at low energies shows substrate surface phonons as an important cooling mechanism, highlighting the importance of substrate choice in future graphene devices. In contrast at the very highest energy scales accessed only by photoexcitation the cooling is shown not to be influenced by the presence of a substrate, but out-of-plane phonon modes increase cooling of the hot optical phonons.

Acknowledgements

How could I begin my acknowledgements without thanking Alex for offering me the chance to work in his lab. His enthusiasm for physics knew no bounds be it meetings that lasted well into the night, or the time we took time out of the christmas party to find a little more signal to noise in the current experiments. The lab hasn't been the same without Alex and its at times like this he is missed the most. Euan your crazy power to ask a question that makes me realise I understand nothing should not be underestimated. It is a power you have used wisely and I really appreciate. The way you approach understanding a new problem was very educational. Your honest appraisals of my current progress were motivational and appreciated, however I seemed to take them at the time. Dave when I started you were always willing to help and teach me things and amazingly later when you became my supervisor that help and mentorship increased to amazing levels. Your attention to detail be it in experiment or when looking over my exceptionally poor grammar and spelling (Im sure there are many mistakes on this particular page) is incredible. I couldn't write some acknowledgements without thanking my parents. Obviously without them I wouldn't be here but they have also been so generous with moral support and not forgetting financial support these past 25 years. I really appreciate all you have done for me and here is the big secret Im not sure that this science thing pays that well, so it could be a while till I can return the favour. Shona thanks for being a great little sister and putting up with all my boring science talk. I would especially like to thank Andrey for your willingness to spend time explaining difficult (for me) concepts and providing restraint when the ideas get a bit strange. Another person without whom this I wouldn't know one side of a lock-in from the other is Adam, your help in building experiments and interpreting them was invaluable. I just hope I was more amusing than annoying when we sat together, I feel it may have been a little of both. Other big thanks goes to Pete for some great measurements with which to model and endless cups of tea, the tea statistics are looking very one sided now you have gone to the other side of the world. Paul thanks for all the help be it little "can you do this it will only take five minute" jobs to building sample chambers that have been invaluable. For all the helium and putting up with constant changes in my demands for helium,

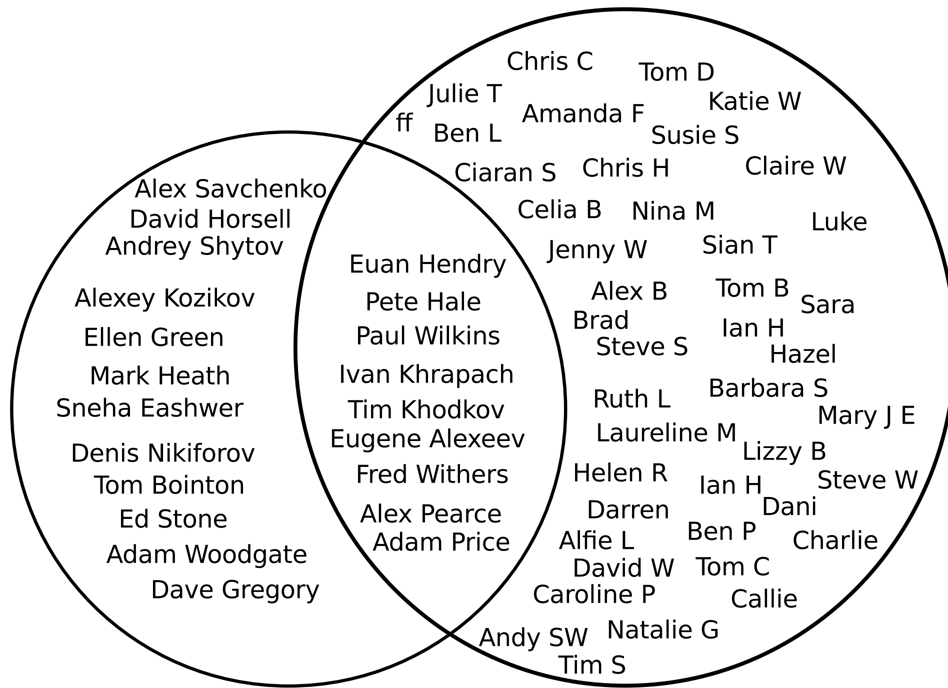

Essential for this Thesis　Distracting Pub People

Figure 1: A Venn diagram of thanks.

Adam and Dave you have been great. I would also like to thank Ed for teaching me the workings and all the little tricks of the laser system. Thanks must go at this point for all the people who have made the last three years so much fun, the people who for each time a sample broke (or failed to work at all) would be there to make me smile or at the very least cart me off to the nearest pub/source of caffeine. There are so many people to thank, so at this point i would like to introduce a new acknowledgements paradigm I have separated all my remaining thanks into a Venn diagram. Enjoy!

Contents

Abstract **2**

Acknowledgements **3**

Contents **5**

List of Figures **8**

Introduction **16**

1 Theory **18**

1.1 Band Structure of Graphene 18

1.1.1 Linear Regime 23

1.1.2 Chirality 24

1.1.3 Berry Phase 25

1.1.4 Density of States 25

1.2 Conductivity of two dimensional systems at low temperatures 26

1.2.1 Electron Specific Heat Capacity 27

1.2.2 Hall Effect 27

1.2.3 Weak Localisation 29

1.2.4 Universal Conductance Fluctuations 33

1.2.5 Phonons in Graphene 34

1.2.6 Phonon Phonon Scattering 34

2 Experimental Method **37**

2.1 Sample Fabrication 37

2.2 Optical Contrast 39

2.3 Raman Spectroscopy of Graphene 40

2.3.1 Layer Determination 43
2.4 Low Temperature Transport Measurements 47
2.4.1 Dependence of the Resistance on carrier concentration 48
2.5 Optical Techniques 48

3 Heat Dissipation Mechanisms in Graphene 51
3.1 Introduction 51
3.2 Samples and Measurement Technique 52
3.3 Contact Pinning 53
3.4 Comparison of temperature profiles with data 55
3.5 Simple Temperature Model 55
3.6 Heat Transport Model 60
3.6.1 Acoustic Phonons 64
3.6.2 Remote Optical Substrate Phonons 66
3.7 Conclusions 67

4 Quantum Corrections to the Conductivity in a High Electric Field 68
4.1 Field Dependent Weak Localisation model 69
4.2 Averaging of the Universal Conductance Fluctuations (UCF) 70
4.3 Sample Characterisation 73
4.4 Magnetoconductivity 74
4.5 Conclusions and Future Work 77

5 Hot Phonon Decay in Graphene 79
5.1 Measurements of the Differential Reflection 80
5.2 Two Temperature Model 81
5.2.1 Excitation Pulse 84
5.2.2 Computation of the Model 85
5.2.3 Fitting the Data 86
5.3 Layer Dependence of the Phonon Decay Time. 86
5.3.1 Layer Dependence of the Phonon Decay Time in Suspended samples. 87
5.4 Conclusions 89

6 Desorption of Oxygen from Graphene by Femtosecond Laser Pulses 91

6.1 Experimental Method 93

6.2 Laser Desorption of Oxygen 95

6.3 Two Pulse Correlation 98

6.4 Conclusion 102

7 Conclusions and Future Work 103

Bibliography 105

List of Figures

1 A Venn diagram of thanks. . . . 4

1.1 Graphene Lattice and first Brillouin zone 19

(a) Graphene lattice with A and B lattices marked in yellow and blue respectively, the primitive lattice vectors a_1,a_2 marked in red and the nearest neighbour vectors $\delta_{1,2,3}$ in green. . . . 19

(b) Graphene first Brillouin zone with the $k = 0$ zone center Γ point and the two K points marked. . . . 19

1.2 22

(a) Electronic dispersion of graphene showing the 6 crossing points in the first Brillioun zone 22

(b) Cross section through two cones showing the two inequivalent valleys and the linear regions near $0eV$ 22

1.3 Chirality in graphene and the direction of the pseudospin vector for various directions of k 24

1.4 Hall effect in a 6 terminal Hall bar. 28

1.5 Scattering Paths in a diffusive 2DEG 30

(a) Two scattering pathways t_1 and t_2 through a diffusive material between two points A and B. Elastic scatterers are shown as black dots. 30

(b) A time reversed loop contributing to the weak localisation effect in which the start and end points are identical 30

1.6 Figure showing the conductivity correction $\Delta\sigma$ as a function of magnetic field for different values of the three characteristic lengths. . . . 31

1.7 Figure showing the phonon dispersion relation for monolayer graphene taken from [18]. 35

1.8 Anharmonic scattering orders and their related scattering processes. (a) Phonon decay into two phonons (b)Two phonon recombination (c) Three phonon decay (d) Phonon phonon scattering (e) Three phonon recombination. 36
(a) Cubic 36
(b) Cubic 36
(c) Quartic 36
(d) Quartic 36
(e) Quartic 36

2.1 Fabrication process for graphene based field effect transistor. 38
(a) Tape with graphite. 38
(b) Graphene deposits on substrate. 38
(c) Graphene deposited on substrate. 38
(d) PMMA spun onto surface. 38
(e) Electron beam irradiation. 38
(f) PMMA development leaving pattern. 38
(g) Gold/Chromium evaporation. 38
(h) Metal liftoff leaving sample intact. 38
2.2 Reflectance spectrum of the wafer used (300nm silicon dioxide on doped silicon) under white light illumination. The minimum in the reflectance at 575nm is due to destructive interference within the 300nm cavity. 40
2.3 Figure showing the absorption of photon of frequency f_{in} an interaction with a phonon of frequency ω_{ph} and finally the emission of a Stokes shifted photon of frequency f_{out} 41
2.4 44
(a) Diagram of the graphene bandstructure showing the zero momentum Γ scattering process leading to the G peak and the intervalley G' process with momentum around the Γ point. Recombination process is shown offset for clarity. 44
(b) Diagram of the graphene bandstructure showing the intervalley K process leading to the $2D$ peak. 44

2.4 *cont.* 45
(c) Diagram of the graphene bandstructure showing the process leading to the D peak. 45
(d) Figure showing the Raman spectra of monolayer graphene with the major peaks labelled. Spectra were taken with a 532nm laser with a spot size of $1\mu m$ and a incident power of 5mW. Graphene was defected by F.Withers by fluorination of an exfoliated graphene flake. 45
2.5 (a)-(d) shows the four different transitions for a K phonon through a schematic of the bilayer dispersion with the recombination process being ommitted for clarity. (e) shows the resulting $2D$ peak with four fitted Lorentzian corresponding to the four different processes above with peak frequencies at 2658,2688,2706,2721 cm^{-1}. This figure is taken from reference [18] 46
2.6 Measurement circuit for four terminal resistance measurements of a graphene flake with concentration control though the gate voltage V_g. An AC/DC mixing circuit in the constant current configuration. . . . 47
2.7 (a) Resistance vs Gate voltage curve for a 7.1μm by 4.2μm flake of monolayer graphene at a temperature of 246mK. (b) Linear band structure around one of the K points. 49
(a) 49
(b) 49
2.8 (a) Diagram of the laser amplification system with a pulse splitting and delay system showing 2 beams P1 and P2 delayed by the addtional path in P1. (b) Diagram showing the two pulses in a pump probe experiment with a delay of τ_D. 50
(a) 50
(b) 50

3.1 The various tis controlled byhermal reservoirs and the coupling mechanisms between them in a standard graphene sample shown in figure 2.1. 52

3.2 (a) Probe configuration (b) Resistance as a function of source drain bias between contacts V_A and V_B measured for different source drain contacts $S_{(1,2,3)}$ and $D_{(1,2,3)}$. Each colour denotes a different contact pair. 54

(a) 54

(b) 54

3.3 Sample A: Temperature dependence and bias dependence. 56

(a) 56

(b) 56

(c) 56

3.4 59

(a) Temperature profile along the sample at 2mV according to Eqn 3.1. The temperature is pinned to T_{bath}=4.2K at either end. . . 59

(b) Resistance profile along the sample at values of V_{AB} from 0 (blue) to 10mV(red) in 0.4mV steps. 59

(c) Dependence of the Resistance on V_{AB} for sample B at V_g=3V (black dots). Fit due to electron diffusion (blue). 59

(d) Figure showing the effective gate voltage (blue dashed line) as a function of distance x along the flake. 59

3.5 Figure showing the direction of the asymmetry in V_{AB} dependent on the gate voltage . -3V,0V and 3V with respect to the Dirac point are coloured respectively red,black and blue. 60

3.6 Comparison of the eqn 3.1 with measured data for different concentrations in sample B 61

(a) Temperature dependence of the resistance at zero bias. Curves have been normalised for easy comparison between concentrations -3V (red),-10V (green),-16V (blue) 61

(b) -3V 61

(c) -10V 61

(d) -16V 61

3.7 Sample A (16μm) showing source drain bias dependence of the resistance at different gate voltages. Smooth curves correspond to the three different calaculations with no phonons (solid blue), acoustic phonons only (dotted green) and acoustic phonons with remote interface phonons(dashed red) 62
(a) 3V 62
(b) -6V 62
(c) -12V 62
3.8 The rate of energy loss to phonons as a function of temperature. Blue curve shows the rate of energy loss to acoustic phonons in the graphene sheet. Green curve shows the rate of energy loss to acoustic phonons and remote interface phonons. These processes happen on different timescales (b) showing the low temperature region in greater detail than (a). 64
(a) 64
(b) 64
3.9 Temperature profile along the length of the sample for the three separate models; no phonons (solid blue), acoustic phonons only (dotted green) and acoustic phonons with remote interface phonons(dashed red) at an applied source drain bias of 70mV, a gate voltage of 3V and a bath temperature of 4.2K. 65

4.1 72
(a) Gate voltage dependence of the resistance at 7K(Black) and 50mK(Red) showing the appearance of strong universal conductance fluctuations.(Sample A) 72
(b) Magnetoresistance curves at 50mK showing the averaging effect of applying an additional AC gate bias (5Hz). Increasing bias is shown in increasing steps of 0.5V from blue to pink with an offset of 0.5$k\Omega$ for clarity. A applied measurement current of 1.5nA was used. (Sample A) 72
4.2 Hall effect at different values of V_G 75

(a) Hall voltage as a function of magnetic field at V_g=25,30,35,40V (red,blue,green,purple). 75
(b) Dependence of the concentration n on the value of the gate resistance. (Sample A) 75
4.3 Temperature dependence of the weak localisation. 76
(a) Temperature Dependence (T_{Bath}) of the magnetoconductivity at a range of temperatures 0.25K,1K,4.2K and 24K(from black to red) showing the quenching of the weak localisation effect at high bath temperatures. Data was recorded with a excitation current of 1.3nA. 76
(b) Current dependence of the conductivity increasing from black to red (0.65nA,83nA,320nA) taken at the temperature of 0.25K. 76
4.4 Extracted values of L_ϕ,L_i and $L_\star$ for the bath temperature dependence. 77
4.5 Dephasing length against calculated electron temperature. Increasing current is denoted by a change in colour from black to red. Dotted lines show the value of L_E for the different currents. A small reduction in the dephasing length is seen for larger currents. 78

5.1 Figure showing the wavelength dependence of the differential absorption. Figure taken from [72] 81
5.2 Graphene Brillioun zone showing the three inequivalent points Γ,K,K'. The blue annuli around the three inequivalent points show the area allowed for phonon scattering encompassed by M_{ph} (not to scale). The outer bound of the annuli is given by the maximum energy of electrons within the system. The lower bound is given by the maximum momentum lost by a phonon of energy $\hbar\omega_{\mathrm{ph}}$. 82
5.3 Probability of scattering $[\rho_e - \rho_a]$ as a function of energy for E_f = 0.2eV,$n_{\mathrm{ph}} = 0.05$ and temperature from 200K to 1000K (blue to red) 83
5.4 The value of the integrand in Γ as a function of energy E_f = 0.2eV,$n_{\mathrm{ph}} = 0.05$ and temperature from 200K to 1000K (blue to red) 84
5.5 The electron (blue) and phonon(green) temperatures as a function of time t from excitation pulse (centred around $t = 0$) calculated for a τ_{ph} of 2ps and a fluence $F = 0.128 \times 10^{15}$. 85

5.6 Supported Graphene 88
(a) Normalised differential reflectivity as a function of probe delay for different layer samples. The fits are generated by the two temperature model with fluence and τ_{ph} as free parameters. The different layer numbers are 1,2,3,4 and 6 denoted by black,red,green,purple and blue respectively. 88
(b) Extracted phonon lifetime as a function of layer number. Note the large spread associated with the different samples measured the average for each layer is show by the black squares and the error bars are the standard deviation. 88
5.7 Suspended Graphene 90
(a) AFM height map of the graphene flake and substrate clearly showing the graphene suspended above the etched holes. 90
(b) Comparison of the average supported and suspended τ_{ph} as a function of layer number. 90

6.1 Time dependence of the electron (red) and optical phonon (black) temperatures due to an absorbed fluence of 0.1 J/m^2 calculated using the two temperature model from chapter 5. 92
6.2 (a) Resistance versus voltage curve (RVg) as a function before and after exposure to 1atm of oxygen(black and grey respectively). The positions of the extracted Dirac points are indicated by the dotted lines. The change in Dirac point position is given by ΔV_g. (b) Shows the extracted Dirac point position as a function of time after oxygen exposure at time=0. The scatter in the points is caused by the extraction process the black line shows a 20 point moving average giving a better comparison with the averaging used later. 94
(a) 94
(b) 94

6.3 Figure showing the evolution of the doping level with increasing number of pulses N ($0.11Jm^{-2}$),160fs delay between pulse pairs). (A) shows the gate voltage dependence of the resistance with increasing number of pulses (from gray to black). The initial and final Dirac point positions are marked by gray and black dotted lines respectively. (B) Shows the absolute position of the Dirac point extracted from (A) by taking the maximum resistance point as a function of the number of incident pulses. The reduction in the gradient is attributed to the reduction in number of oxygen molecules absorbed. 96

(a) 96

(b) 96

6.4 Gate voltage shift per pulse as a function of integrated power. Data points were taken with different lengths of exposure. Fit of a power law dependence (black) of the form $x^{4.2}$ (the factor can vary by a large amount between samples) 98

6.5 The experimental setup for the measurement of graphene under irradiation of ultrafast pulses. 99

6.6 Typical change in the Dirac point position (doped position is $V_D = 10.7 \pm 0.2$V) as a function of the number of pulses incident upon the flake at varying pulse delays. Linear gradient fits are taken to the determine the strength of the effect. Combined incident power of the two pulses was $2.4Jm^{-2}$ 100

6.7 Normalised average change per pulse as a function of pump probe delay. Points are produced by a linear fit of absolute Dirac point position as a function of number of exposures. 101

Introduction

Carbon is the 6th element in the periodic table and with its 4 valence electrons can be organised into many different allotropes. In 2004, graphene was first isolated making it the most recent allotrope be be found. Being a single atomic layer of carbon electrons in graphene can only experience motion in the plane of the layer. Since its discovery graphene has attracted great interest both from a pure physics standpoint and the possible technological applications. This thesis is concerned with the behaviour of graphene when energy is added to the charge carriers in the system, both through the application of a large electric field and also photons incident upon the surface. This energy can create a system out of equilibrium in which new physics can be observed. In this thesis a number of varied techniques are used to study the nature of heat transfer and it's effect on the properties of graphene.

In chapter 2 the standard fabrication and characterisation of graphene samples for measurements in the later chapters are described.

In chapter 3, dependence of the resistance on applied bias is studied at low temperatures. Through measurements of the temperature dependence of the resistance a model is developed to explain the observed nonlinear behaviour in terms of electron overheating. The precise shape of the non-linearity is then used to investigate cooling of hot electrons via acoustic phonon modes in the graphene sheet and, unexpectedly, optical phonon modes in the silicon substrate. The latter are shown to be an important cooling mechanism in graphene devices.

In chapter 4, the effect of a large electric field on weak localisation is investigated. A new technique for measurement of quantum corrections in graphene is described. The results from chapter 3 are used to analyse the overheating of the electrons when subjected to these fields. Preliminary results suggest that there is no electric field effect present in the weak localisation and most features can be accounted for by

the overheating model.

In chapter 5, ultrafast differential absorption techniques are used to probe the relaxation mechanisms and timescales associated with hot electrons generated by photoexcitation. The decay of hot optical phonons are seen to be the limiting factor in cooling the hot electrons. A dependence of the decay rate on the number of carbon layers is seen and the role of the substrate in hot carrier cooling is investigated.

In chapter 6, desorption of oxygen molecules from the graphene surface is studied. The timescales of desorption are probed by a novel two pulse correlation technique. A change in charge transfer from the graphene to the oxygen is seen in the transport properties of the device, and is used in combination with the optical measurements to detect desorption of oxygen from the surface.

Chapter 1

Theory

This chapter discusses some of the basic concepts which will be required later in this thesis. The transport properties of graphene are discussed starting with calculation of the graphene band structure using the tight binding model. A review of the important contributions to electron transport of graphene is then made with emphasis on the temperature dependence of these contributions. Finally the properties of phonons in graphene are discussed.

1.1 Band Structure of Graphene

Graphene with it's three σ orbitals arranged in an sp^2 bonded honeycomb structure is left with a single electron in an out of plane π orbital through which conduction can occur. The primitive lattice vectors of the crystal lattice ,as shown in figure 1.1a , are given as:

$$a_1 = \frac{a}{2}\begin{pmatrix} 3 \\ \sqrt{3} \end{pmatrix}, \qquad a_2 = \frac{a}{2}\begin{pmatrix} 3 \\ -\sqrt{3} \end{pmatrix}, \tag{1.1}$$

where $a \approx 1.42$Å is the interatomic spacing. Also shown in figure 1.1a are the nearest neighbour vectors which are by definition the same for both sublattice A and B due to their identical nature. They are given by three vectors:

$$\delta_1 = \frac{a}{2}\begin{pmatrix} 3 \\ \sqrt{3} \end{pmatrix}, \quad \delta_2 = \frac{a}{2}\begin{pmatrix} 3 \\ -\sqrt{3} \end{pmatrix}, \quad \delta_3 = a\begin{pmatrix} -1 \\ 0 \end{pmatrix}, \tag{1.2}$$

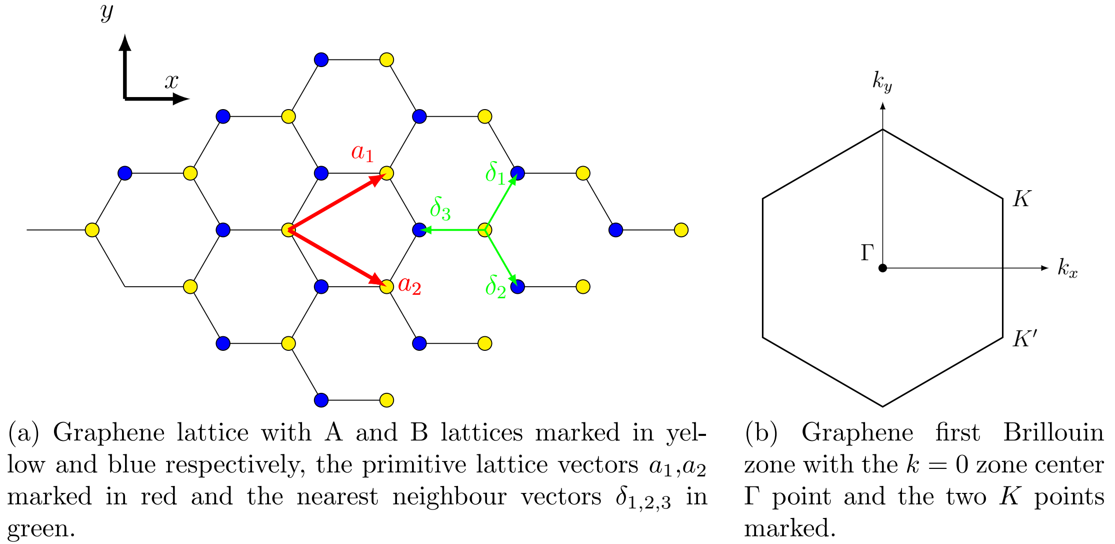

(a) Graphene lattice with A and B lattices marked in yellow and blue respectively, the primitive lattice vectors a_1,a_2 marked in red and the nearest neighbour vectors $\delta_{1,2,3}$ in green.

(b) Graphene first Brillouin zone with the $k = 0$ zone center Γ point and the two K points marked.

Figure 1.1

Through the relation $a_i.b_j = 2\pi\delta_{ij}$ gives the reciprocal lattice vectors as:

$$b_1 = \frac{2\pi}{3a}\begin{pmatrix} 3 \\ \sqrt{3} \end{pmatrix}, \qquad b_2 = \frac{2\pi}{3a}\begin{pmatrix} 3 \\ -\sqrt{3} \end{pmatrix}. \tag{1.3}$$

The first Brillouin zone (fig 1.1b) can now be defined by the planes bisecting the vectors to the first set of reciprocal lattice points. The Brillouin zone maintains the hexagonal structure of the real space lattice but with a rotation of $\pi/2$ radians.

To calculate the band structure of graphene the tight binding approximation will be used. This assumes strongly localised electrons moving between nearest neighbours. Only nearest neighbours will be considered it was shown in [1] that the modification due to next nearest neighbours is a small correction.

First the wavefunction of the electrons will be defined by a summation of Bloch waves over all the lattice sites A and B

$$\mid \psi\rangle = \sum_A u_a e^{i\vec{k}\cdot\vec{R_A}} \mid R_A\rangle + \sum_B u_b e^{i\vec{k}\cdot\vec{R_B}} \mid R_B\rangle\ , \tag{1.4}$$

where $u_{A,B}$ is a Bloch function with the same periodicity as the reciprocal lattice and $R_{A,B}$ the wavefuction associated with a particular lattice site. The Hamiltonian can then be written by considering transitions between the two lattice sites associated with a hopping energy $t = 2.8\text{eV}$ [2] and by defining the onsite energy as zero due

to the identical nature of the carbon atoms at A and B

$$\hat{H} = -t \sum_{R_A} \sum_{i=1}^{3} \mid R_A\rangle\langle \vec{R_A} + \vec{\delta_i} \mid -t \sum_{R_B} \sum_{i=1}^{3} \mid R_B\rangle\langle R_B + \vec{\delta_i} \mid \ , \tag{1.5}$$

where the first term denotes hopping from the A to the B lattice by the nearest neighbour vector $\vec{\delta_i}$. By substitution of the Hamiltonian into the Schrödinger equation

$$\hat{H} \mid \psi\rangle = \epsilon_k \mid \psi\rangle \tag{1.6}$$

and by using the orthogonality conditions of $\langle R_A \mid R_B\rangle = 0$ and $\langle R_A \mid R_A\rangle = 1$ gives

$$\epsilon_k \mid \psi\rangle = -t \sum_{R_B} \sum_{i=1}^{3} u_A e^{i\vec{k}\cdot(\vec{R_B}-\vec{\delta_i})} \mid R_B\rangle - t \sum_{R_A} \sum_{i=1}^{3} u_B e^{i\vec{k}\cdot(\vec{R_A}-\vec{\delta_i})} \mid R_A\rangle \ . \tag{1.7}$$

By multiplication through by $\mid R_A\rangle$ or $\mid R_B\rangle$ a set of simultaneous equations are given

$$\begin{aligned} \langle R_A \mid \hat{H} \mid \psi\rangle &= \epsilon_k \langle R_A \mid \psi\rangle \\ -t \sum_{R_A} \sum_{i=1}^{3} u_B e^{i\vec{k}\cdot(\vec{R_A}+\vec{\delta_i})} &= \epsilon_k u_A \sum_{R_A} e^{i\vec{k}\cdot\vec{R_A}} \\ -tf(k) u_B &= \epsilon_k u_A \end{aligned}$$

$$\begin{aligned} \langle R_B \mid \hat{H} \mid \psi\rangle &= \epsilon_k \langle R_B \mid \psi\rangle \\ -t \sum_{R_B} \sum_{i=1}^{3} u_A e^{i\vec{k}\cdot(\vec{R_A}-\vec{\delta_i})} &= \epsilon_k u_B \sum_{R_B} e^{i\vec{k}\cdot\vec{R_A}} \\ -tf(k) u_A &= \epsilon_k u_B \end{aligned}$$

where $f(\vec{k}) = \sum_{i=0}^{3} e^{i\vec{k}\cdot\vec{R_A}}$ finally this can be expressed in matrix notation as

$$\begin{pmatrix} 0 & -tf(k) \\ -tf^*(k) & 0 \end{pmatrix} \begin{pmatrix} u_A \\ u_B \end{pmatrix} = \epsilon_k \begin{pmatrix} u_A \\ u_B \end{pmatrix} \ . \tag{1.8}$$

Solving for the determinant of two by two matrix approximates the energy dispersion

for electrons in graphene:

$$E(\vec{k}) = \pm t\sqrt{|f(k)|^2} \tag{1.9}$$

which can be expanded by substitution of the nearest neighbour vectors (eqn 1.2) in terms of the Cartesian coordinates k_x, k_y as

$$E(\vec{k}) = \pm t\sqrt{1 + 4\cos\left(\frac{\sqrt{3}a}{2}k_y\right)\cos\left(\frac{3a}{2}k_x\right) + 4\cos^2\left(\frac{\sqrt{3}a}{2}k_y\right)}\,. \tag{1.10}$$

A plot of equation 1.10 is shown in figure 1.2 in which energy isosurface is plotted as a function of k_x and k_y, a cross section through the surface is taken crossing the two K points.

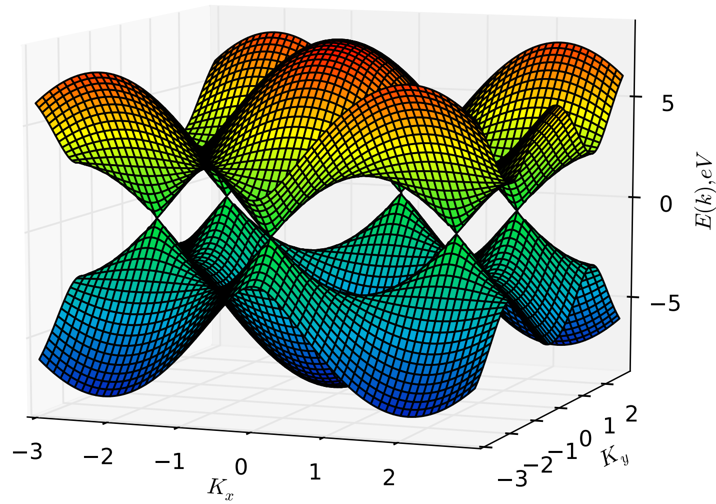

(a) Electronic dispersion of graphene showing the 6 crossing points in the first Brillioun zone

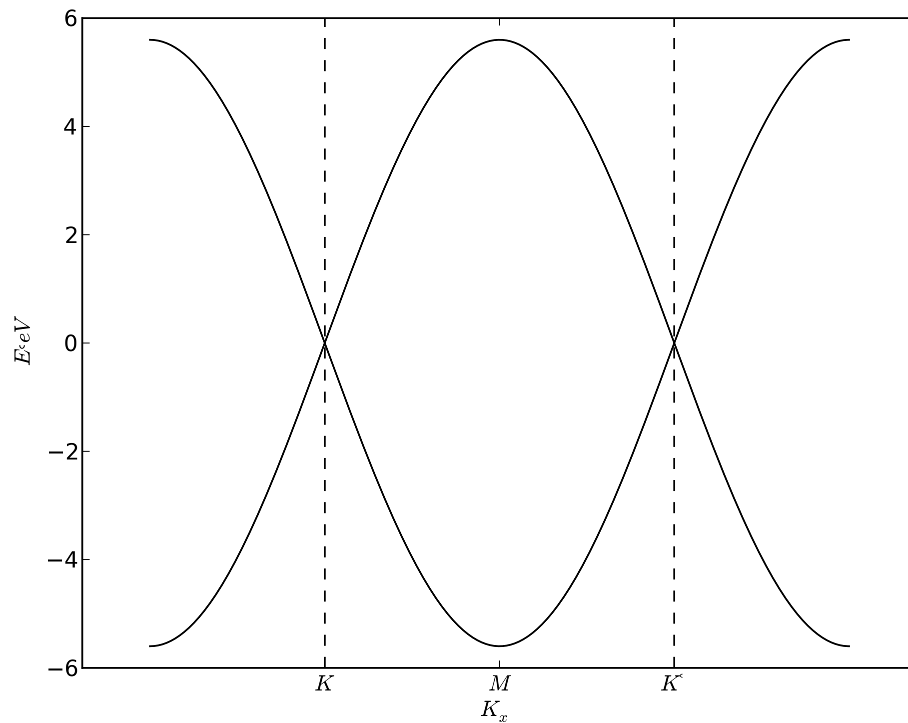

(b) Cross section through two cones showing the two inequivalent valleys and the linear regions near $0eV$

Figure 1.2

1.1.1 Linear Regime

The zero crossing points within the Brilluion zone correspond to the high symmetry points in the reciprocal lattice K and K'. Through geometrical transforms of the reciprocal lattice vectors it can be shown that the position of these point are given as

$$K = \frac{2\pi}{3a}\begin{pmatrix} 1 \\ \sqrt{3} \end{pmatrix} \,,\; K' = \frac{2\pi}{3a}\begin{pmatrix} 1 \\ -\sqrt{3} \end{pmatrix} \tag{1.11}$$

and it can be shown that at both crossing points the energy goes to zero $E(K) = E(K') = 0$. Expanding around the K point (the derivation is identical bar a minus sign for K') by a small amount Δk allows $f(\vec{k})$ to be rewritten as

$$f(\vec{k}) = \sum_{i=0}^{3} e^{i(\vec{k}+\Delta\vec{k})\cdot\vec{R_A}} \;, \tag{1.12}$$

solving for the new $f(\vec{k})$ gives a new Hamiltonian

$$H = -v_F \begin{pmatrix} 0 & \pm(\Delta k_x - i\Delta k_y) \\ \pm(\Delta k_x + i\Delta k_y) & 0 \end{pmatrix} = v_F\vec{\sigma}\cdot\Delta\vec{k} \;, \tag{1.13}$$

where the plus/minus refers to the K and K' valleys respectively and $\vec{\sigma}$ is the 2D representation of the Pauli matrices

$$\sigma_x = \begin{pmatrix} 0 & 1 \\ 1 & 0 \end{pmatrix} , \sigma_y = \begin{pmatrix} 0 & -i \\ i & 0 \end{pmatrix} \;. \tag{1.14}$$

Finally it can be shown by taking the secular determinant of equation 1.13 that

$$E(\vec{k}) = \pm\hbar v_F|\Delta\vec{k}| \;, \tag{1.15}$$

allowing a simple conversion between energy and momentum with the constant of proportionality the Fermi velocity. This Fermi velocity has the value $v_F \sim 10^6$m/s [3]. The upper and lower limits are obviously the beginning of the band bending in the regime $E(\vec{k}) \leq \pm t$ but due to extrinsic factors experimentally there is also a region around the Dirac point where inhomogeneity in the flake prevents the concentration from becoming zero. This inhomogeneity can come from a number

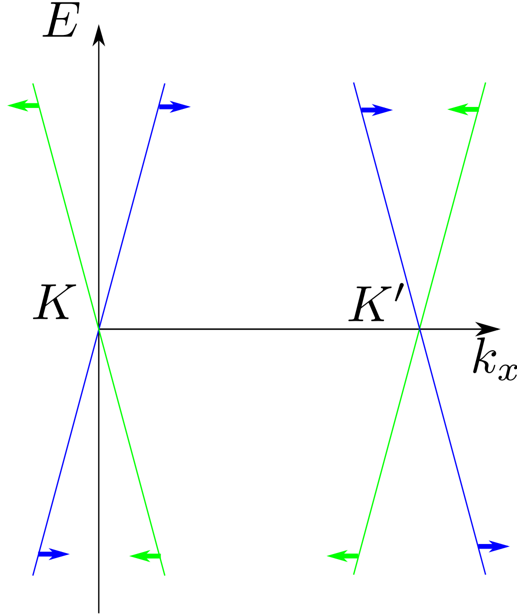

Figure 1.3: Chirality in graphene and the direction of the pseudospin vector for various directions of k

of sources including adsorbed molecules [4], ripples [5, 6] and charge traps in the substrate [4].

1.1.2 Chirality

By redefining $\Delta\vec{k}$ as $\vec{p}$ and from the dispersion relation 1.15 in combination with Hamiltonian and the Schrödinger equation gives

$$\vec{\sigma} \cdot \vec{p} = \pm|\vec{p}| \ . \tag{1.16}$$

By dividing through by the modulus of the momentum, the chirality can be defined:

$$\chi = \vec{\sigma}\frac{\vec{p}}{|\vec{p}|} = \pm 1 \ . \tag{1.17}$$

For this equation to be true $\vec{p}$ and $\vec{\sigma}$ must be either parallel or antiparallel to each other. This is the origin of the pseudospin and is valid in the low energy linear regime. Suppression of electron backscattering occurs due to the opposite directions of the pseudospin vector on either side of the valley (see figure 1.3): any scattering event between opposite branches of the dispersion have a probability that tends to zero.

1.1.3 Berry Phase

Berry phase is the phase change in the electron wavefunction following a closed path in momentum space. When an electron adiabatically changes its momentum around the Fermi surface at a constant energy the additional phase can be calculated by taking the electron wavefunction [7]

$$\Psi \propto \begin{pmatrix} e^{-i\theta/2} \\ e^{i\theta/2} \end{pmatrix} e^{i\vec{p}.\vec{r}} , \tag{1.18}$$

by substitution of $\theta = 2\pi$ constituting a full revolution around the Fermi inside a single cone and factorising out the original wavefunction.

$$\Psi \rightarrow \Psi \begin{pmatrix} e^{-i\pi} \\ e^{i\pi} \end{pmatrix} . \tag{1.19}$$

This result showing a Berry phase shift of π in contrast with a value of 0 for regular 2DEGs. This will become important later when considering interference effects between two paths around the Fermi surface.

1.1.4 Density of States

The density of states in graphene has an interesting difference with that of a normal 2DEG in which the density is energy independent.

The density of states can be written as

$$\nu(E) = \frac{dn}{dE} = g_v \frac{2\pi k}{N} \frac{dk}{dE} \tag{1.20}$$

where g_v is the degeneracy of states, $(2\pi k dk)$ is the additional area of the Fermi surface under a infinitesimal increase dk and N the total number of states. Using the differential of the dispersion relation $E = \hbar v_F k$ and simplifying, equation 1.20 becomes

$$\nu(E) = \frac{E}{\pi(\hbar v_F)^2} . \tag{1.21}$$

1.2 Conductivity of two dimensional systems at low temperatures

The conductivity of a two dimensional system at low temperatures can be considered as a sum of various conductivity corrections change the total conductivity

$$\frac{1}{\sigma(T)} = \frac{1}{\sigma_{\text{Drude}}} + \frac{1}{\sigma_{\text{Quantum corrections}}(T)} + \frac{1}{\sigma_{\text{el-ph}}(T)} \ . \tag{1.22}$$

The Drude model of conductivity considers the electrons as particles moving through a network of scatterers accelerating in an electric field until the momentum and velocity are randomised by a collision. The electron acquires a drift velocity of $\boldsymbol{v} = -e\boldsymbol{E}\Delta t/m$ where $\boldsymbol{E}$ is the electric field applied, m is the effective mass and Δt is the time elapsed since the last collision. By taking an average of all Δt the impurity scattering time τ is extracted. This allows us to write the average drift velocity as [8]

$$\boldsymbol{v}_{\text{drift}} = -\mu\boldsymbol{E} \ , \tag{1.23}$$

where $\mu = e\tau/m$ is the mobility of the electrons. We can now define the conductivity σ as [9]

$$\sigma = \frac{-en\boldsymbol{v}_{\text{drift}}}{\boldsymbol{E}} = en\mu \ . \tag{1.24}$$

The Einstein relation allows the conductivity σ to be related to the electronic properties of the system in this case the density of states via a constant of proportionality D

$$\sigma = e^2\rho(E_F)D \ . \tag{1.25}$$

The diffusion constant in 2D can be written as [9]

$$D = \frac{1}{2}v_F^2\tau = \frac{1}{2}v_F l \ , \tag{1.26}$$

where l and τ are the mean free path and mean free scattering time respectively. D can be thought of as describing the speed at which electrons diffuse into an area linking the intrisic speed of electrons at the Fermi level v_F by scattering with an average length of l.

1.2.1 Electron Specific Heat Capacity

The simplest model for the electronic heat capacity comes from the application of the Drude model (section 1.2) to the empirical law of Wiedemann and Franz (1853). Assuming that the dominant heat transfer mechanism in these metals was the conduction electrons. The thermal conductivity can be simply defined [8] as the constant of proportionality in

$$\vec{j}^q = -\kappa \nabla T \ , \tag{1.27}$$

where $\vec{j}^q$ is the thermal current and ∇T is the temperature gradient. The simple picture in this case is an electron at a distance x along the sample has an energy related by the Fermi-Dirac distribution to other electrons in the vicinity of x. Electrons travelling from regions of high temperature on average have a larger energy than electrons travelling from a cold region this leads to a net energy flow down the temperature gradient ∇T.

Using the Fermi-Dirac distribution we can also write the constant volume electronic specific heat capacity c_V as [8]

$$c_v = \left(\frac{\delta u}{\delta T}\right)_v \ , \tag{1.28}$$

where, assuming no interactions between the electrons, the internal energy U can be written as the sum of all the levels in the system $E(k)$(eqn 1.10) times their occupancy $f(E(k))$

$$U = 2\sum_k E(k) f(E(k)) \ , \tag{1.29}$$

where the Fermi Dirac function $f(E)$ is given as

$$f(E) = \frac{1}{e^{(E-\mu)/k_B T} + 1} \ . \tag{1.30}$$

The value of the specific heat capacity will become important for determining the electron temperature under laser excitation in chapter 5.

1.2.2 Hall Effect

The classical Hall effect occurs as the charged electrons travelling in a conductor experience a transverse force when a magnetic field B is applied. This force propor-

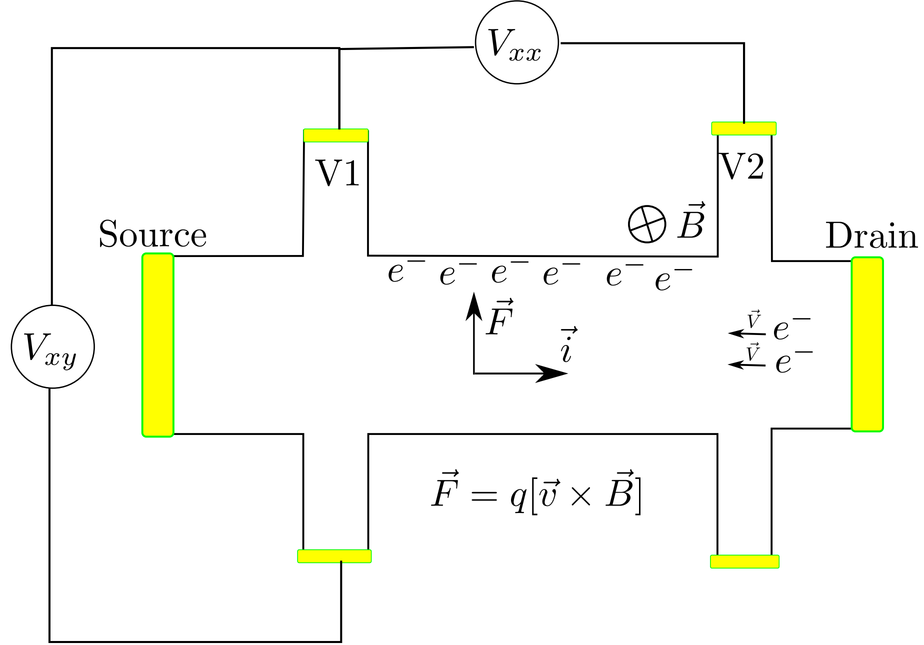

Figure 1.4: Hall effect in a 6 terminal Hall bar showing the force $\vec{F}$ applied to electrons e^- and the corresponding charge built up across the sample.

tional to the perpendicular magnetic field $\vec{B}$ is called the Lorentz force. By bending of the electron trajectory causes a build up of charge one side of the sample which creates an electrostatic repulsive force that in equilibrium equals the Lorenz force. Figure 1.4 shows a Hall bar sample geometry used throughout this thesis for transport measurments including measurements of the Hall voltage denoted by V_{xy}. An electric field is applied between source and drain contacts inducing a current $\vec{i}$ and producing a voltage drop between V_{xx} through which the standard resistance R is measured . The voltage between the two sides of the sample proportional to the magnetic field applied is measured by the voltage probe denoted V_{xy}. The charge built up is expected to depends on both the current and the magnetic field applied. A coefficent ,known as the Hall resistance, is given by [8]

$$R_H = \frac{B}{en} \ . \tag{1.31}$$

Experimentally by measuring V_{xy} as a function of B, the gradient of which R_H allows a simple determination of the carrier concentration n. Providing the sample geometry allows measurements transverse to the current flow.

1.2.3 Weak Localisation

Weak localisation was first observed as an anomalous increase in the resistance at low temperatures. In the Drude model, the resistance decreases as temperature decreases due to the scattering time τ increasing as scattering processes such as electron-phonon scattering are suppressed [9]. At very low temperatures, below the energy of most phonons, the resistance is constant with temperature and depends on impurity and defect scattering. Neither of these effects can cause an increase in the scattering rate at low temperature. The semi-classical Drude model takes into account some of the physics associated with the Fermi-Dirac distribution of electrons around the Fermi level but in essence treats the electrons as solid particles scattering in a medium. In this classical approach the probability of transmission, proportional to the conductivity, is the sum of all the probability of the paths between two points. In figure 1.5a two scattering trajectories t_1 and t_2 are shown between two points A and B. The total probability of transmission between the points is the sum of transmission probabilities of all the possible paths i,

$$P(A, B) = \left| \sum_i t_i \right|^2 . \tag{1.32}$$

During each scattering event in a path t the velocity vector of the electron is randomised whereas the phase of the electron may be correlated before and after the scattering event. By including the phase of electrons and by considering quantum interference between electron paths additional corrections to the Drude conductivity arise.

$$P(A, B) = \sum_i |t_i|^2 + \sum_{i \neq j} t_i t_j^* , \tag{1.33}$$

where t_j is another trajectory through the system and the second term gives the quantum interference correction. In the case $A \neq B$ each different path through the system (and there are many in a large diffusive system) arrives with a random phase and the sum of all these phases averages to zero. Figure 1.5b shows the special case where $A = B$ and the electron returns to a point in the crystal. In this case the phase shift going clockwise around the loop is perfectly correlated with an electron going anti-clockwise around the loop. The symmetry of the system guarantees time reversal invariance which gives the probability as $t_i = t_j = t$ when substituted into

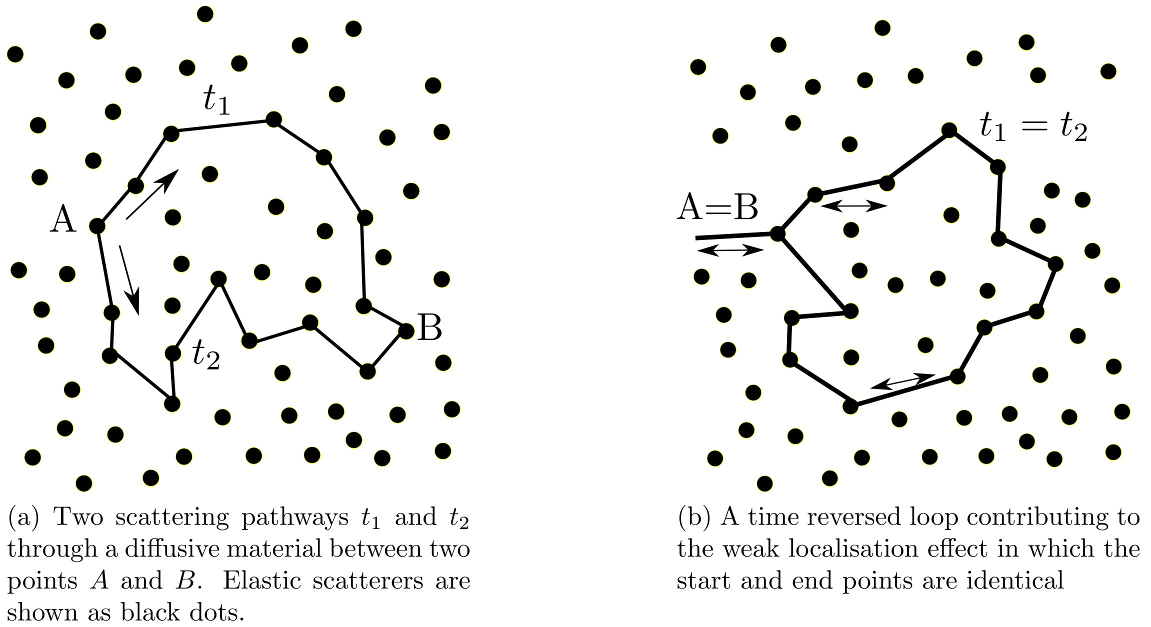

(a) Two scattering pathways t_1 and t_2 through a diffusive material between two points A and B. Elastic scatterers are shown as black dots.

(b) A time reversed loop contributing to the weak localisation effect in which the start and end points are identical

Figure 1.5

equation 1.33 gives

$$P(A, A) = 4|t_i|^2 \tag{1.34}$$

twice as large as the the classical result of $2|t_i|^2$. This additional probability to find the electron at the point A is the origin of the term weak localisation. This in turn reduces the speed at which an electron travels through the crystal and decreases the conductivity. In order to calculate the correction to the conductivity due to the weak localisation $\delta\sigma_{wl}$ we can look at the time integral of the return probability [10]

$$\frac{\delta\sigma_{wl}}{\sigma} \propto -\int_0^\infty C(t)e^{t/t_\phi}dt\ , \tag{1.35}$$

where a number of concepts need to be introduced. The return probability $C(t)$ depends on the diffusion constant D and decays as $1/t$ in two dimensions the integrand of which tends to infinity on long timescales. To combat this a maximum timescale on which the electron can return and still maintain a correlated phase is introduced as an exponential decay depending on τ/τ_ϕ (when $\tau \sim \tau_\phi$ there are no smaller loops) this dephasing time is limited by inelastic scattering events such as electron phonon scattering and electron electron scattering which modify the wavefunction of the electron. This time is strongly temperature dependent and this restricts the temperature range at which the weak localisation is observed.

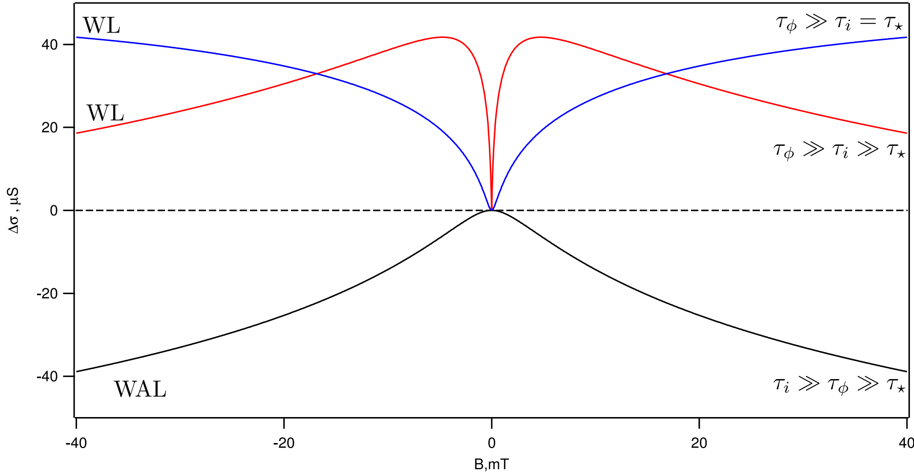

Figure 1.6: Figure showing the conductivity correction $\Delta\sigma$ as a function of magnetic field for different values of the three characteristic lengths.

Application of a magnetic field suppresses the weak localisation due to the breaking of time reversal symmetry between the two paths. The application of a magnetic field B introduces an Aranhov-Bohm phase effect due to the magnetic flux through the area surrounded by the loop. The clockwise and anticlockwise loops have an opposite sign of the phase. The additional phase factor between the two loops can be written as [9]

$$\phi = \frac{2e}{\hbar}\int(\nabla \times \boldsymbol{A}).d\boldsymbol{S} = \frac{2eBS}{\hbar} = 2\pi\frac{\Phi}{\Phi_0}\ , \tag{1.36}$$

where $\boldsymbol{A}$ is the magnetic vector potential, S the area of the loop Φ the flux and $\Phi_0 = h/2e$ the elementary flux quantum. With applied magnetic field the flux threaded by each loop increases: this effect depends on the size of the loop so the largest loops are most affected by the magnetic field. At larger magnetic fields the ensemble average of the phase shifts due to a range of loop areas average to zero and there is no longer a increase in the probability. This occurs when the magnetic length $l_m = \sqrt{\hbar/eB}$ is comparable to the dephasing length l_ϕ. The highest magnetic field range where this approach is still valid is when the magnetic length is comparable to l the mean free path: in this case all loops contain at least one magnetic flux quantum. The effect of the magnetic field therefore adds a long time cutoff to equation 1.35.

In graphene there are a number of modifications to the weak localisation due to the chiral nature of the carriers and the unique electronic dispersion seen in figure 1.2. Firstly as the weak localisation process involves an electron rotating its $\vec{k}$

vector halfway around the Fermi surface it picks up an additional Berry phase of $\pi/2$ compared with the time reversed case where an electron picks up a Berry phase of $-\pi/2$ giving a total phase shift of $\pi/2-(-\pi/2)=\pi$ causing destructive interference. This additional phase shift reverses turns an increased probability (weak localisation) into a decreased probability known as weak antilocalisation(WAL). This leads to an increase in the conductivity at low temperatures. This expected WAL behaviour was not initially observed in graphene [11]. To find the explanation for this two other elastic scattering mechanisms must be considered. Intervalley scattering between the K and K' valleys restores weak localisation [12].Intervalley scattering is caused by short range defects and edges which provide the necessary momentum to scatter between the valleys.These processes are characterised by the intervalley scattering time τ_i. The other scattering mechanism is large angle scattering within a single valley caused by much smoother scattering potentials such as ripples. Due to the chirality breaking this intervalley scattering mechanism suppresses backscattering and the weak localisation.

A further effect to consider is the effect of trigonal [13, 14] warping. This is the a deviation from the circular nature of the Fermi surface to more triangular due to the inclusion of next nearest neighbour terms in the tight binding model. This warping of the valleys around K and K' leads to symmetry breaking between $+k$ and $-k$ directions. By breaking the symmetry there is no state at $-k$ with an identical energy so no elastic process can scatter there. This leads to a suppression of paths that only scatter within a single valley. Trigonal warping does not affect paths that include an intervalley scattering event as the warping term has an opposite sign between the K, K' valleys. The intravalley scattering and the warping can be combined into a single scattering time $\tau_\star$.

With these additional corrections the temperature dependence of the resistivity goes as [12]

$$\frac{\delta\rho(0)}{\rho^2}=\frac{e^2}{2h}\left[\ln\left(1+2\frac{\tau_\phi}{\tau_i}\right)-2\ln\frac{\tau_\phi/\tau}{1+\frac{\tau_\phi}{\tau_\star}}\right] \tag{1.37}$$

and the magnetoresistance goes as [12, 15]

$$\Delta\sigma(B)=-\frac{e^2}{\pi h}\left[F\left(\frac{\tau_B^{-1}}{\tau_\phi^{-1}}\right)-F\left(\frac{\tau_B^{-1}}{\tau_\phi^{-1}+2\tau_i^{-1}}\right)-2F\left(\frac{\tau_B^{-1}}{\tau_\phi^{-1}+\tau_i^{-1}+\tau_\star^{-1}}\right)\right], \tag{1.38}$$

where $F(z)$ is the digamma function

$$F(z) = \ln z + \varphi\left(\frac{1}{2} + \frac{1}{z}\right) , \tag{1.39}$$

and

$$\tau_B^{-1} = \frac{4De}{\hbar} , \tag{1.40}$$

Where τ_B^{-1} is the inverse of the magnetic time. Figure 1.6 shows the behaviour of equation 1.38 with different values of the three characteristic times. The WAL curve shows the expected behaviour in graphene with no intervalley scattering all the paths considered have a Berry phase of π and an increasing magnetic field causes a decrease in the conductivity. In the other two cases where the intervalley scattering is strong compared with the dephasing length multiple intervalley scattering events occur between the two valleys cause a restoration of the WL. The effect of weak localisation will be important chapters 3 and 4.

1.2.4 Universal Conductance Fluctuations

Universal conductance fluctuations (UCF) is a mesoscopic interference effect. They manifest as random, aperiodic reproducible fluctuations in the conductance caused by a modulation in the scattering landscape of the sample. In the simplest form the UCF are caused by differences in the impurity configuration of the sample [16] giving a distribution of resistances for samples with nominally identical dimensions. More simply than measuring samples with different impurity concentrations the effective impurity configuration can changed by varying the Fermi energy giving a different scattering potential or by varying an applied magnetic field adding phase factors very much like the weak localisation case. It can be shown that size of conductance fluctuations due to the averaging of different paths has a universal value:

$$\Delta G \approx \left(\frac{e^2}{h}\right)^2 \tag{1.41}$$

when taken in the diffusive regime where the entire sample is considered to be coherent $L_\phi \gg L_x$. Fluctuations around this value will be seen in any graphene sample at low enough temperatures.

1.2.5 Phonons in Graphene

Non equilibrium distributions of electrons can occur when an external source of energy such as light or large electric fields exceeds the energy loss from these hot optical phonons. This representative relaxation time will be used in chapter 6 to describe the decay of the system. This loss can occur in a number of ways either through reradiation, diffusion of excited electrons out of the system or conversion of that energy into atomic motion through excitation of phonon modes. As suggested by Anderson [17] electron overheating can be a significant effect at low temperatures. In regimes where elastic electron-electron scattering is very fast compared to inelastic scattering time $\tau_{e-e} \ll \tau_{\text{inelastic}}$ excited electrons scatter off each other distributing the energy between every electron. This distribution of electron energy can be described by a Fermi-Dirac distribution with effective temperature T_{el}. This allows the amount of energy to be characterised by a single value. This thesis will deal with the theory of inelastic scattering mechanisms that can lose energy from the electron system.

The energy loss into atomic motion of the atoms within the crystal lattice can be defined using the concept of quantised vibrations of the lattice. The phonon dispersion for monolayer graphene in figure 1.7 shows 6 distinct branches separated into two distinct classes: the high energy optical modes and the lower energy acoustic modes. These are then subdivided by the direction of oscillation (with respect to the $A - B$ carbon-carbon direction) into; in-plane longitudinal (iLO,iLA), in-plane transverse (iTO,iTA) and out of plane modes(oTO,oTA). Of particular interest is the area around Γ and K in which the iTO and iLO Raman active modes lie. These will be discussed in section 2.3. Firstly emission to the low energy acoustic phonon modes will be considered.

1.2.6 Phonon Phonon Scattering

Phonon-phonon scattering cannot be explained by the simple harmonic approximation of small atomic oscillations. Indeed, in a crystal without defects or edges the thermal conductivity is infinite. Inclusion of the higher anharmonic terms in the expansion leads to the phonon interaction processes shown in figure 1.8 in which

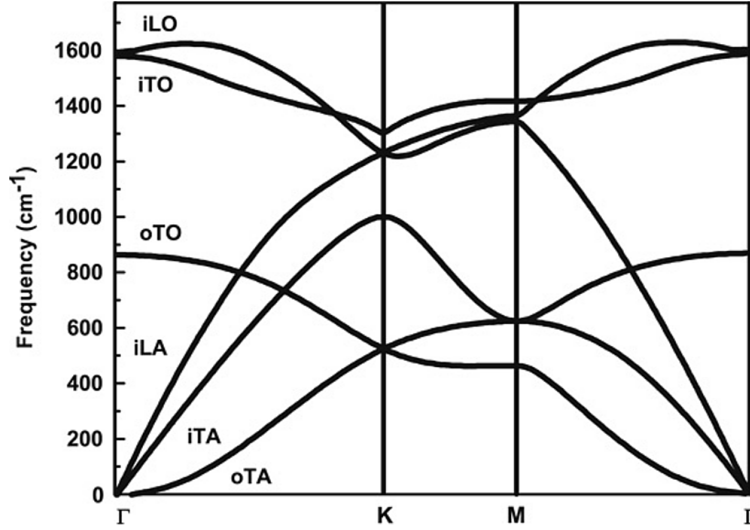

Figure 1.7: Figure showing the phonon dispersion relation for monolayer graphene taken from [18].

energy conservation is satisfied by

$$\sum \hbar\omega(\vec{q}_{\text{in}}) = \sum \hbar\omega(\vec{q}_{\text{out}}) \tag{1.42}$$

where $\vec{q}_{\text{in}}$ is the incident phonon momenta and $\vec{q}_{\text{out}}$ is the outgoing phonon momenta. Additionally crystal momentum is satisfied by the condition

$$\sum \vec{q}_{\text{in}} = \sum \vec{q}_{\text{out}} + \vec{K} \tag{1.43}$$

where $\vec{K}$ is a reciprocal lattice vector. The transition rates of all these different modes can be calculated by perturbation theory [8] and can be collected into a single representative relaxation time τ_{ph} as a characterisation of the probability per unit time of a phonon undergoing any of the various collisions.

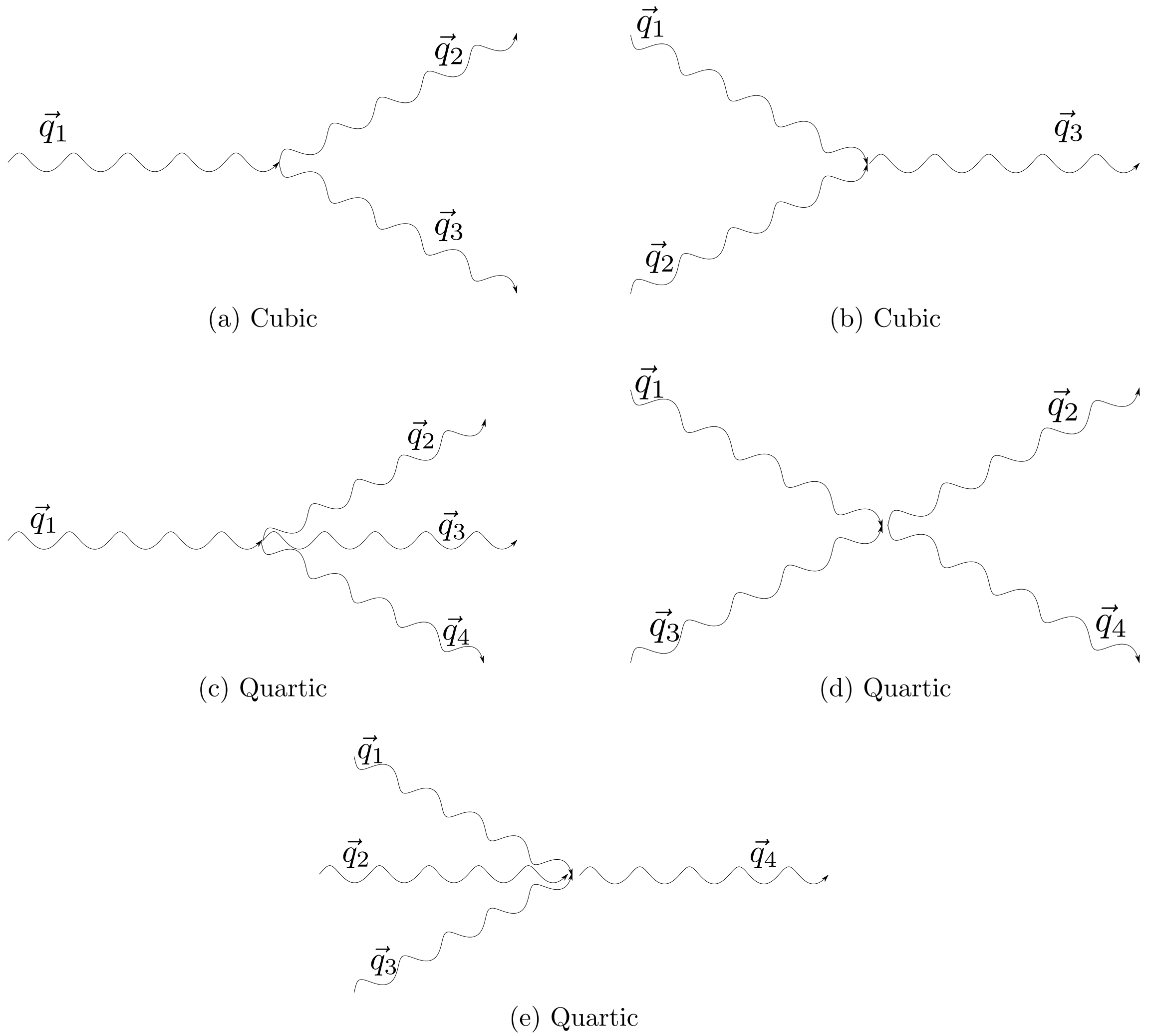

Figure 1.8: Anharmonic scattering orders and their related scattering processes. (a) Phonon decay into two phonons (b)Two phonon recombination (c) Three phonon decay (d) Phonon phonon scattering (e) Three phonon recombination.

Chapter 2

Experimental Method

In this chapter the standard fabrication of graphene samples with electrical connections and control via the field effect of the carrier concentration n is described. All processes involved in the fabrication are described from the initial production of the graphene samples to the layer characterisation through optical contrast and Raman spectroscopy. Finally a few simple electrical characterisation measurements are presented to show the final quality of the produced samples.

2.1 Sample Fabrication

Samples in this thesis are prepared using the process described in figure 2.1 and first described in reference [19]. The first step is to take a source of high quality graphite with large crystal sizes. A natural graphite source (Graphenium) flake is used. This is cleaned by removing with adhesive tape the dirty outer layers. A clean section of tape is taken and a peeling is taken from the top of the graphite crystal. The tape is then folded and unpeeled a number of times to delaminate the graphite flake into thinner (down to one atomic layer) flakes (figure 2.1a). Concurrently with this process, the doped silicon substrates with 300nm thermally grown oxide layer are prepared by cleaning first in acetone then IPA to remove any residues that may already be present followed by short plasma etch in O_2 to remove any organic contaminants. The substrate is placed on a hot plate at an elevated temperature ($50-90\,^{\circ}$C) and the tape graphite covered is pressed down onto it and then removed. This heated deposition method helps to release the adhesive on the tape giving cleaner samples. The tape is then slowly pulled away from the substrate leaving a

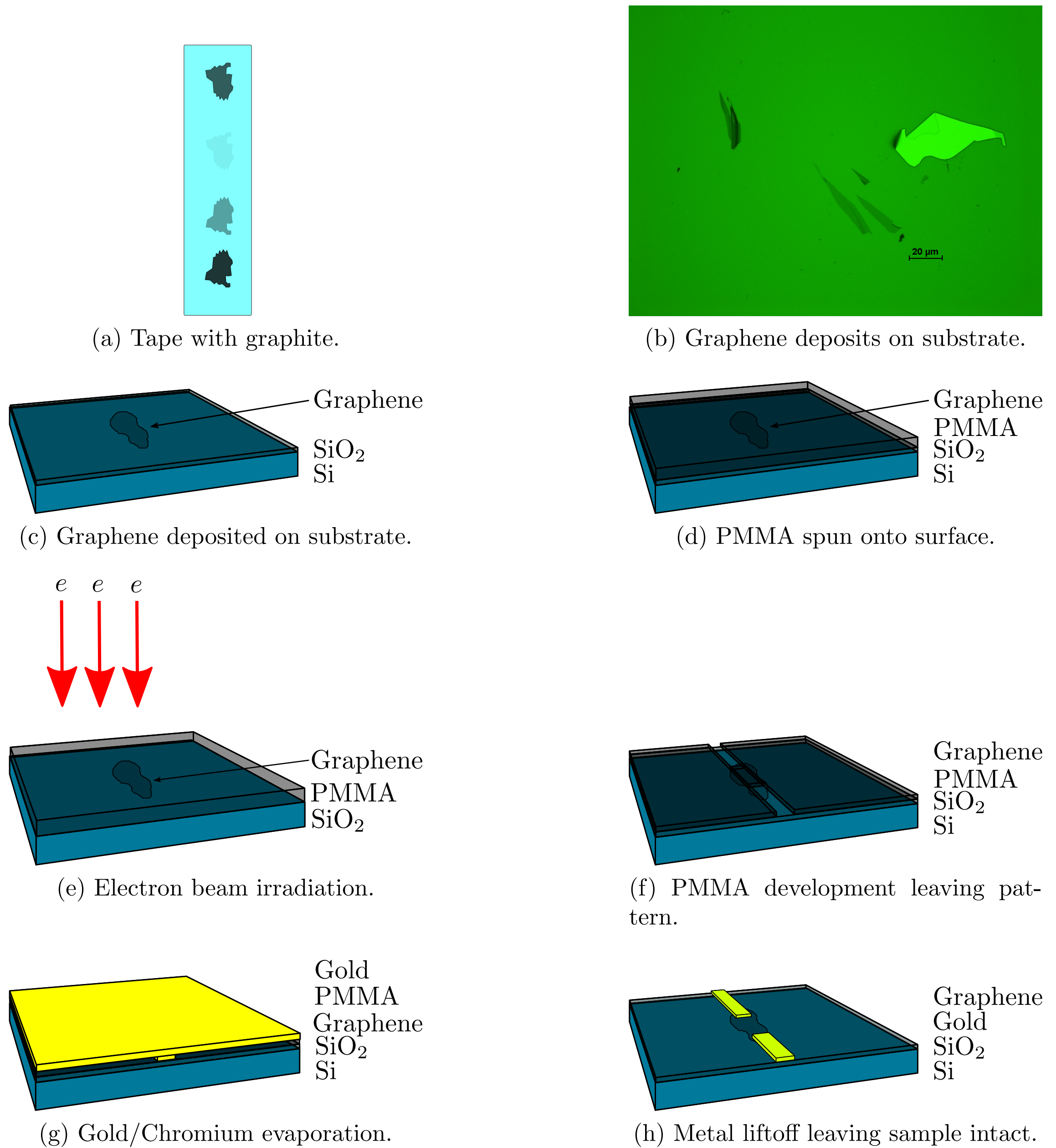

(a) Tape with graphite.

(b) Graphene deposits on substrate.

(c) Graphene deposited on substrate.

(d) PMMA spun onto surface.

(e) Electron beam irradiation.

(f) PMMA development leaving pattern.

(g) Gold/Chromium evaporation.

(h) Metal liftoff leaving sample intact.

Figure 2.1: Fabrication process for graphene based field effect transistor.

number of flakes of graphite/graphene behind.

Once a suitable graphene monolayer has been identified (described in section 2.2,shown in figure 2.1c) electrical contacts are patterned onto the flake using electron beam lithography. A electron sensitive polymer, Poly-methyl-methacrylate(PMMA) dissoved in a solvent (Anisol) solution is spun onto the sample and baked (figure 2.1d). The exposure of the PMMA to an electron beam breaks down the polymer chains in the area exposed and allows the PMMA to be selectively removed by chemical processing to form trenches (figure 2.1f). These trenches can then be filled by a thermally evaporated metallic layer (2.1g). For the graphene samples a layer of chromium (5nm) is used as a bonding layer between the substrate/graphene and the gold contact which provides the conductive link and prevents oxidisation of the chromium. The sample is then immersed in acetone to remove the remaining PMMA and excess gold. Isopropyl alcohol is used to wash away the acetone and the sample is dried in N_2 gas. Finally the sample is affixed to a 20 pin ceramic/gold package using silver paint to give a good electrical connection to the doped Si layer. The gold contacts are connected to the package using an ultrasonic wedge bonder and thin gold wire.

2.2 Optical Contrast

Graphene is lauded for its transparent properties and the technical applications of the transparency in displays [20] and sensing applications [21–24] it is highly absorbing with a single layer absorbing 2.3% of incident light. The contrast of a graphene flake can be defined as

$$\text{Contrast} = \frac{R_{\text{graphene}} - R_{\text{substrate}}}{R_{\text{substrate}}} \tag{2.1}$$

where $R_{\text{graphene,substrate}}$ are the reflection coefficients. In order to maximise the visibility of the flake either the reflectivity of the graphene can be increased or the reflectivity of the substrate can be reduced. As R_{graphene} is a fixed quantity for a single flake the reflectivity of the substrate should be minimised. This can be done by considering the silicon dioxide layer as a Fabrey Perot type cavity of thickness 300nm by choosing an incident wavelength in which there is destructive interference

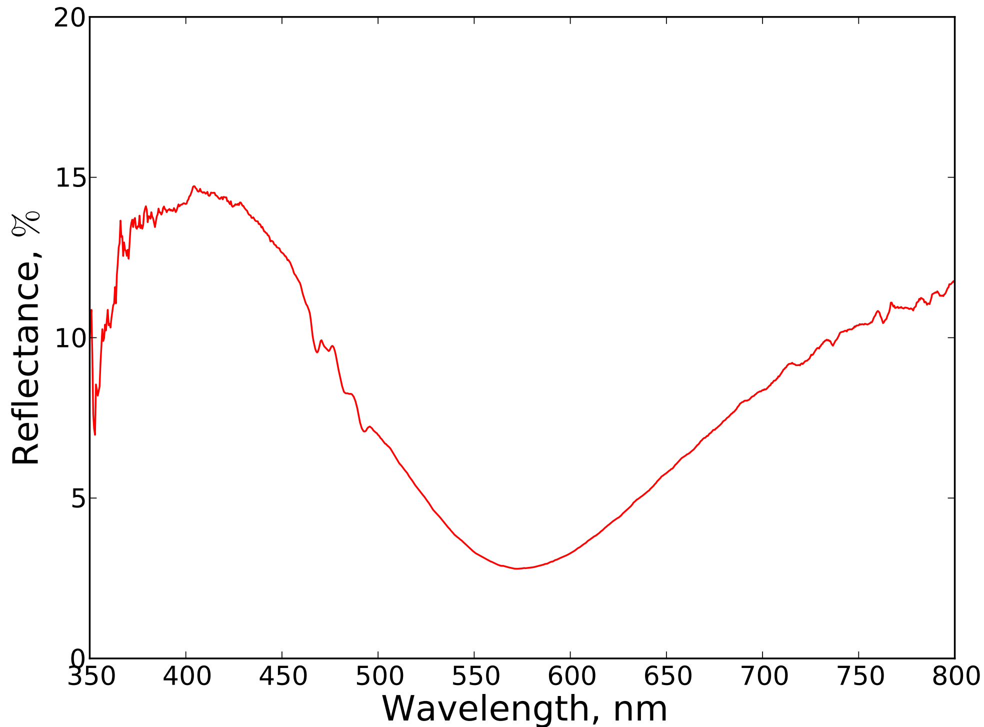

Figure 2.2: Reflectance spectrum of the wafer used (300nm silicon dioxide on doped silicon) under white light illumination. The minimum in the reflectance at 575nm is due to destructive interference within the 300nm cavity.

(approximately a multiple of 300nm ignoring the refractive index change from the silicon to the air and non planer light travelling through a microscope). Figure 2.2 shows the reflection spectra of a bare substrate without graphene allowing a wavelength to be chosen which maximises the graphene visibility. The number of layers in the graphene sheet can also be determined by contrast, additional absorption in each of the layers decreases the reflected light. A simple equation is presented for the contrast in [25]

$$C = 0.0046 + 0.0925N - 0.00255N^2 , \tag{2.2}$$

where $N < 10$ is the number of layers in the graphene flake.

2.3 Raman Spectroscopy of Graphene

Another way to characterise the graphene samples is to directly observe the phonon modes in graphene. This can be achieved via a spectrosopy technique known as Ra-

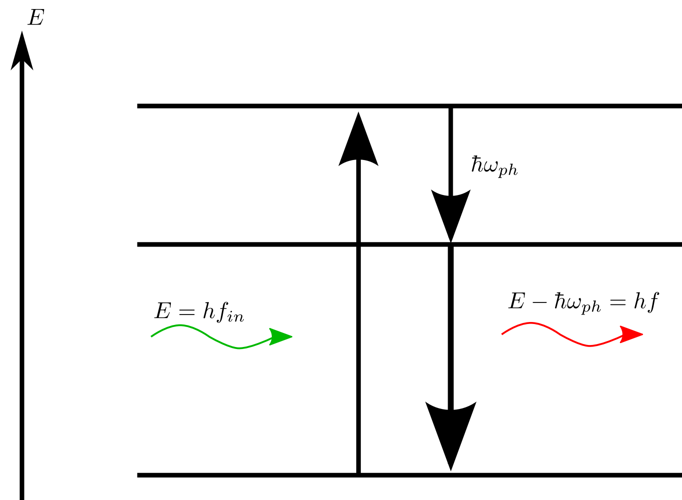

Figure 2.3: Figure showing the absorption of photon of frequency f_{in} an interaction with a phonon of frequency ω_{ph} and finally the emission of a Stokes shifted photon of frequency f_{out}

man scattering. Raman scattering was first discovered by C.V Raman in 1928 [26] by observation of a modified frequency of light passing through liquids. Today Raman spectra can be used non-destructively as a probe of the graphene phonon frequency. From this simple measurement many fundamental electronic and mechanical properties of the graphene can be determined such as number of layers [27], strain [28], Fermi level position [29] [30], defect density [31], thermal conductivity [32] and the presence of functional groups attached to the surface [33].

The Raman scattering process modifies the frequency of the incident light through an interaction with a phonon either losing energy in the creation of a phonon (Stokes shift) , as seen in figure 2.3, or by gaining energy from a phonon (anti-Stokes shift). The stages of a Raman scattering event are shown in Figure 2.3 an initial photon of energy E_{in} is incident on the graphene flake exciting an electron from the valence to the conduction band. This excited electron emits a phonon of energy $\hbar\omega_{\text{ph}}$ lowering the electron in energy by the same amount. The excited electron then recombines with a hole emitting a frequency shifted photon. This frequency shifted light can be detected by filtering the excitation frequency and passing the remaining light into a spectrometer. This requires that the bandwidth of the laser as narrow or narrower than any intrinsic broadening of the Raman shifted photons. The Raman spectrum has 3 distinct peaks shown in figure 2.4d. The peak labelled G due to its initial discovery within the graphite spectrum corresponds to phonons in the vicinity of zero momentum Γ point. Whereas the peaks labelled D and $2D$ are the first and second order phonon modes around the K point in the phonon dispersion (figure 1.7). Figure 2.4c and Figure 2.4a show the intervalley D (found at $\sim$1350cm^{-1}) and intravalley G' (found at $\sim$1650cm^{-1}) peak processes respectively. These processes does not conserve momentum and therefore each can be described as an activated process requiring an additional source of momentum to scatter the electron back to the original cone so that it may recombine. This momentum requires a short range scatterer [34] occurring at edges and atomic defects where there is another source of momentum sufficient to cause intervalley scattering. This allows the use of the D and G' peak intensities as a characterisation of quality in our samples. It is worth noting that the position of the G' peak is strongly dispersive with excitation photon energy as the momentum required to intravalley scatter increases linearly as the excitation energy is increased. Finally the $2D$ peak the strongest in monolayer

graphene is the second harmonic of the D process. The relative strength of this peak is due to two factors; firstly, it conserves momentum due to the two phonons of opposite momentum emitted, and secondly the resonant nature in which every step of the scattering process seen in figure 2.4b lies on a real state increases the probability of this transition.

2.3.1 Layer Determination

In bilayer graphene the $2D$ peak is broadened due to the presence of additional scattering pathways. The tight binding approach to calculation of the band structure has additional terms for hopping between layers leading to the four processes shown in fig 2.5. Due to the slight difference in phonon momentum q between the four separate processes each one has a slightly different energy calculated from the dispersion in figure 1.7 leading to the four overlapping peaks. This method of calculation extends with increasing number of layers but as the number of overlapping increases exponentially going to 15 peaks for trilayer graphene. This deconvolution becomes increasingly difficult and determination of the layer number in thicker flakes will be measured using optical contrast.

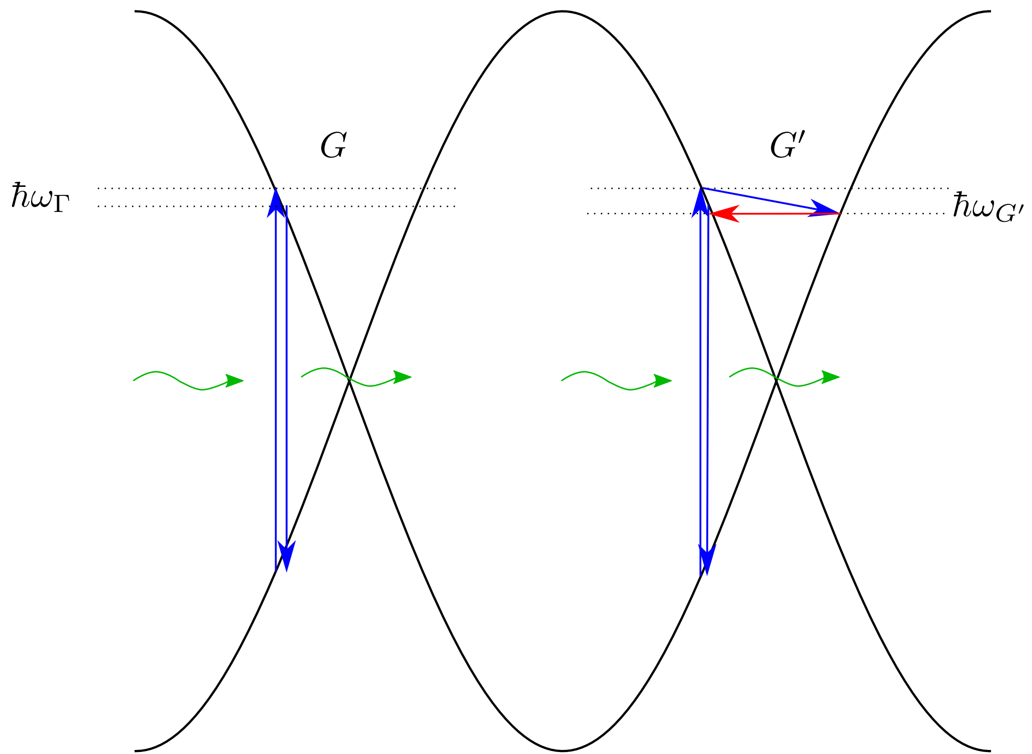

(a) Diagram of the graphene bandstructure showing the zero momentum Γ scattering process leading to the G peak and the intervalley G' process with momentum around the Γ point. Recombination process is shown offset for clarity.

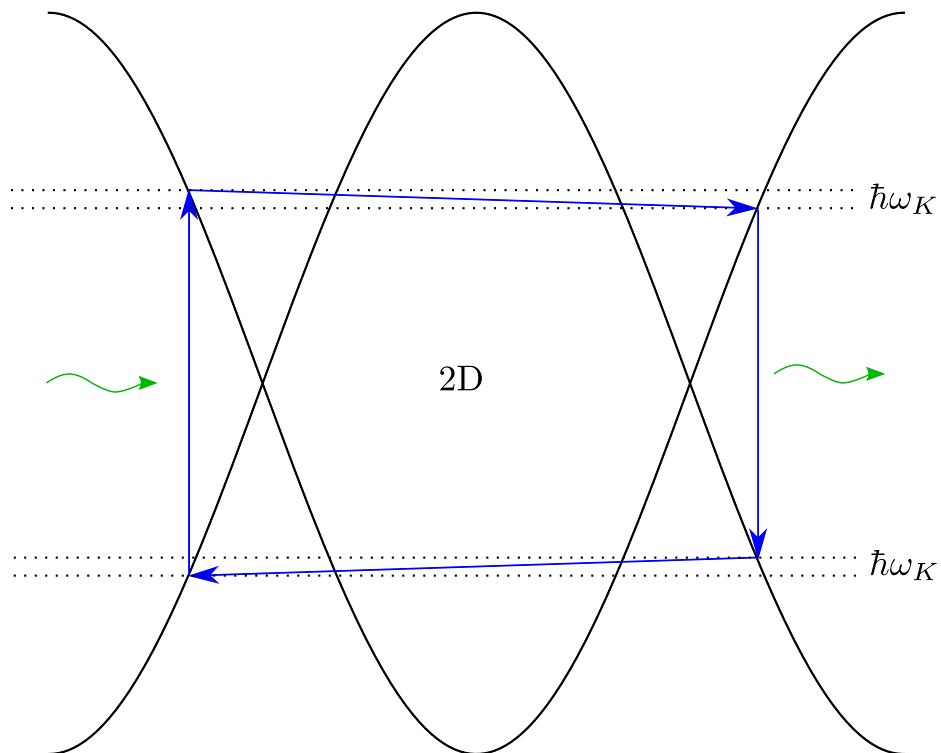

(b) Diagram of the graphene bandstructure showing the intervalley K process leading to the $2D$ peak.

Figure 2.4

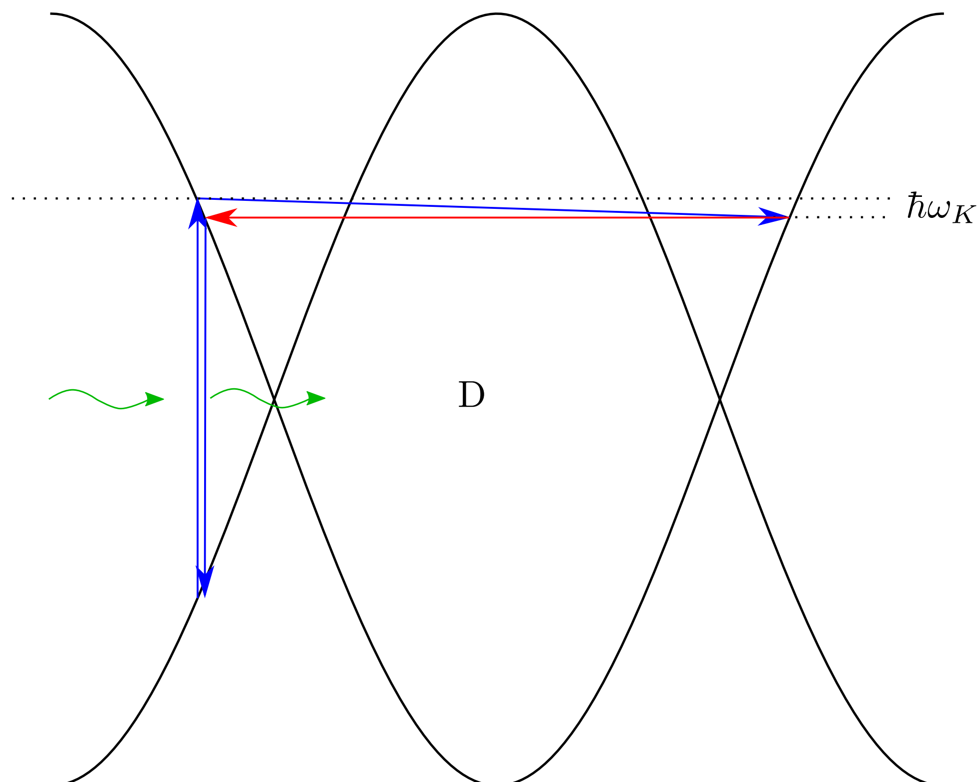

(c) Diagram of the graphene bandstructure showing the process leading to the D peak.

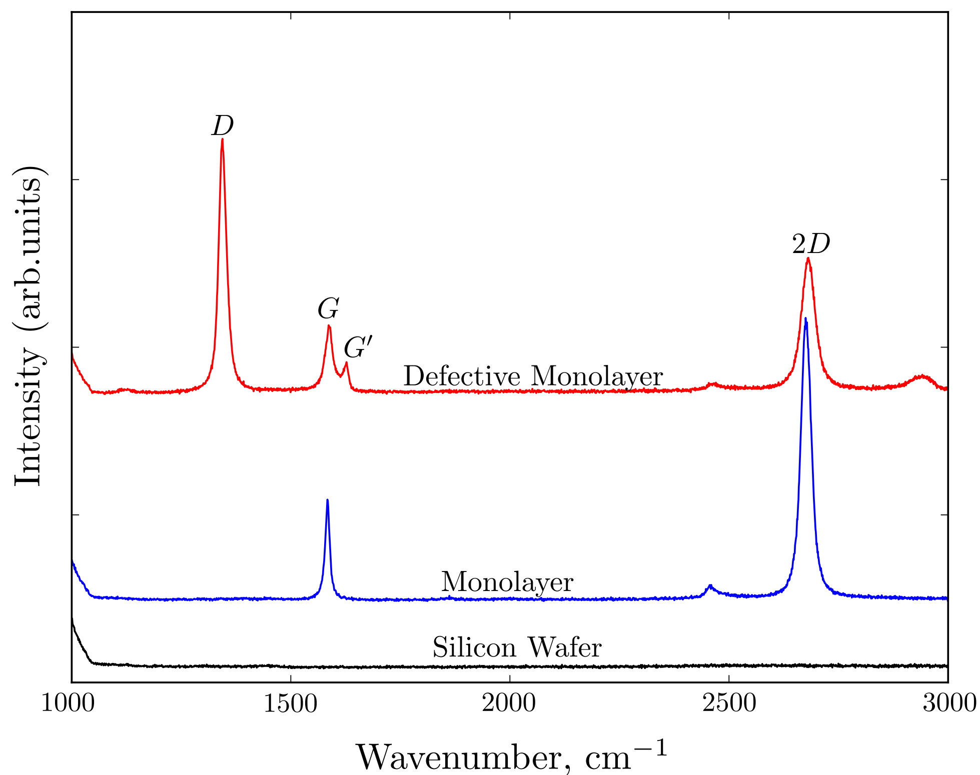

(d) Figure showing the Raman spectra of monolayer graphene with the major peaks labelled. Spectra were taken with a 532nm laser with a spot size of $1\mu m$ and a incident power of 5mW. Graphene was defected by F.Withers by fluorination of an exfoliated graphene flake.

Figure 2.4: *cont.*

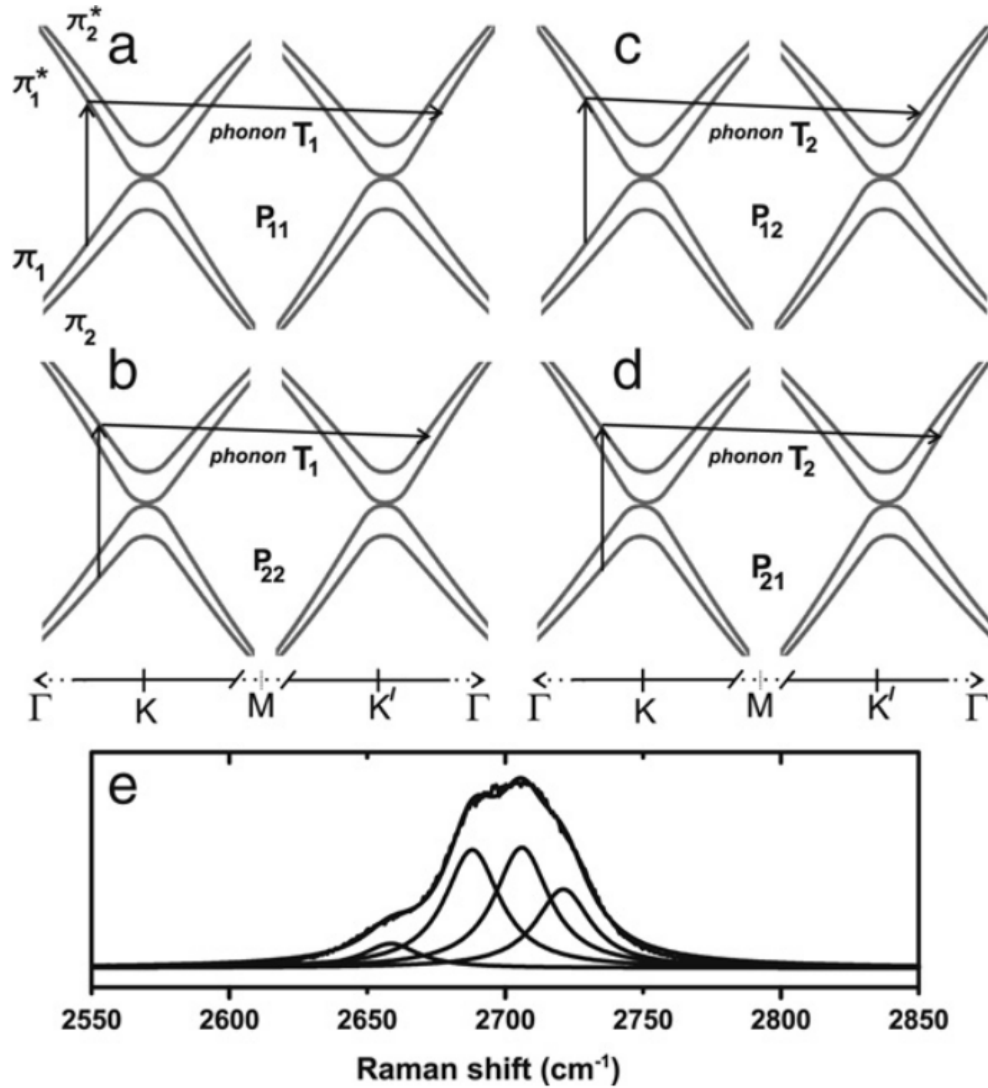

Figure 2.5: (a)-(d) shows the four different transitions for a K phonon through a schematic of the bilayer dispersion with the recombination process being ommitted for clarity. (e) shows the resulting $2D$ peak with four fitted Lorentzian corresponding to the four different processes above with peak frequencies at 2658,2688,2706,2721 cm^{-1}. This figure is taken from reference [18]

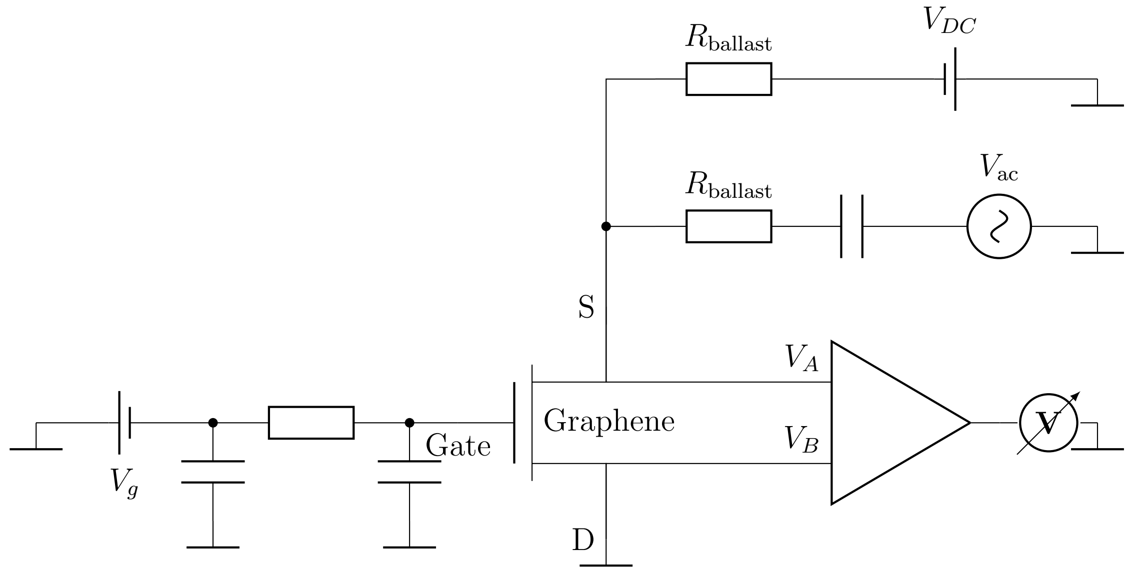

Figure 2.6: Measurement circuit for four terminal resistance measurements of a graphene flake with concentration control though the gate voltage V_g. An AC/DC mixing circuit in the constant current configuration.

2.4 Low Temperature Transport Measurements

Figure 2.6 shows a typical circuit for measurements of the graphene resistance as a function of carrier concentration as modulated by an applied gate voltage $R(V_G)$. This circuit serves as the basis for every circuit used within this thesis for measurements of the resistance as a function of temperature T, source drain bias V_{SD}, and magnetic field B. The sample resistance is determined by applying a voltage V_{ac} to the sample at a set frequency (5Hz - 2kHz)* this voltage produces a current in the wire $I_{ac} = V_{ac}/R_{\text{ballast}}$, where the condition $R_{\text{ballast}} \gg R_{\text{sample}}$ is maintained. This allows the current to be independent of any changes to the sample resistance this is known as the constant current regime. The resistance is then given by $R_{\text{sample}} = (V_A - V_B)/I_{cc}$ where the voltage drop $(V_A - V_B)$ is measured using a lock-in amplifier at the excitation frequency. The lock-in amplifier enhances the noise rejection of the measurement by only measuring at the same frequency and phase as the voltage applied. A four wire technique is used to remove lead and contact resistance from the measurement of the graphene resistance by allowing no current to flow along the voltage sense leads or through the graphene gold interface and therefore no associated voltage drop. This is achieved by having a large input impedance of the operational amplifier and by ensuring that all the grounds in the

*Higher frequencies >20Hz are used in chapter 6 where fast time constants are needed.

system are common and as noise free as possible. The top branch of figure 2.6 is concerned with applying a source drain bias

2.4.1 Dependence of the Resistance on carrier concentration

One of the most powerful tools for measuring the properties of graphene exploits the graphene field effect transistor structure shown in figure 2.1. In this scheme the graphene sheet and doped silicon substrate form two plates of a capacitor separated by the 300nm silicon dioxide layer. By applying a gate potential V_g across the insulating SiO_2 layer the concentration of electrons in the graphene sheet can be modulated. In clean intrinsic graphene at V_g=0 the Fermi level sits at the Dirac point. The quantities of carrier concentration n and Fermi level E_f can be derived using the capacitance, calculated using the thickness t and permittivity of the SiO_2 layer ϵ via $Q = CV = n/e$ to give [19]

$$n = \frac{\epsilon_0 \epsilon V_G}{te} \approx V_G \cdot 7.2 \times 10^{14} m^{-2} V^{-1} \tag{2.3}$$

the Fermi level position is calculated from the capacitance as [35] $E_f = 31 \times 10^{-3}$ meV$\times\sqrt{V_G}$. A typical dependence of the resistance on gate voltage in graphene $R(V_g)$ is shown in figure 2.7a. In the region around zero volts the resistance depends strongly upon the gate voltage and the scattering is dominated by long range scatterers. As the gate voltage and therefore concentration is increased the long range scatterers are screened out and the resistance becomes dominated by short range scatterers [36]. This regime is seen in the figure 2.7a by the flattening of the curve at high gate voltages.

2.5 Optical Techniques

In addition to the transport measurements already described ultrafast optical pulses are used to investigate graphene at a much higher energy scales and with a high time resolution in chapter 5 where the phonon properties are explored and chapter 6 where the properties of adsorbates on the surface are investigated. Ultrafast femtosecond pulses allow for a technique called differential absorbance pump probe

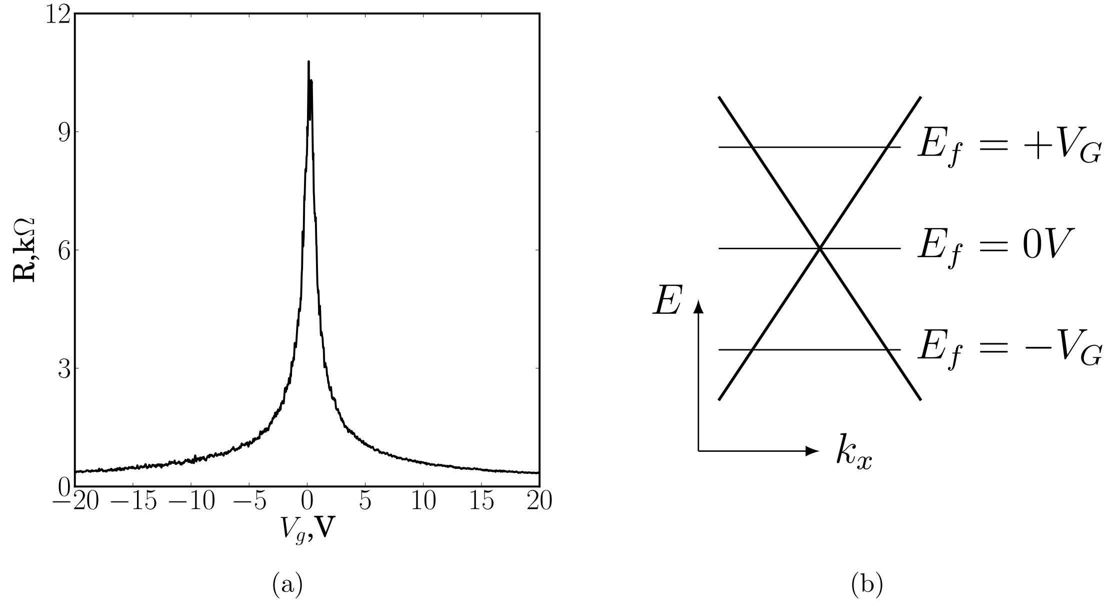

Figure 2.7: (a) Resistance vs Gate voltage curve for a 7.1μm by 4.2μm flake of monolayer graphene at a temperature of 246mK. (b) Linear band structure around one of the K points.

spectroscopy to be employed(chapter 5). By sending in two pulses in short succession the dynamics of the charge carriers on short timescales can be acertained. Figure 2.8 shows the large excitation "pump" pulse and the low power "probe" pulse separated in time by a delay τ_D. The larger pump pulse creates a non equilibrium distribution of electrons which then thermalise through electron electron scattering and relax via inelastic scattering with phonon modes. The second probe pulse senses the excited population through Pauli blocking of states at the excitation energy of the probe. If a large population of carriers Pauli blocks the transition the absorbance is decreased. The sensitivity of this technique is limited by the creation of a significant excited population (pulse energy) and the temporal broadening of the pump and probe pulses (≈100fs). τ_D is controlled by splitting a single laser pulse into two with a beamsplitter and controlling the distance travelled in one of the paths by the introduction of a delay line. Due to the large speed of light small changes in the path length of a few microns allow the probe pulse to be delayed with an accuracy of tens of femtoseconds. In chapter 6, high power laser pulses are used to desorb oxygen from the surface of the graphene a similar setup is required using two large pump pulses and observing a corresponding change in the electrical properties of the flake to sense desorption of the oxygen molecules. In this case large pulse energies are required (up to 3mJ) these are provided by a diode pumped solid state regenerative amplifier

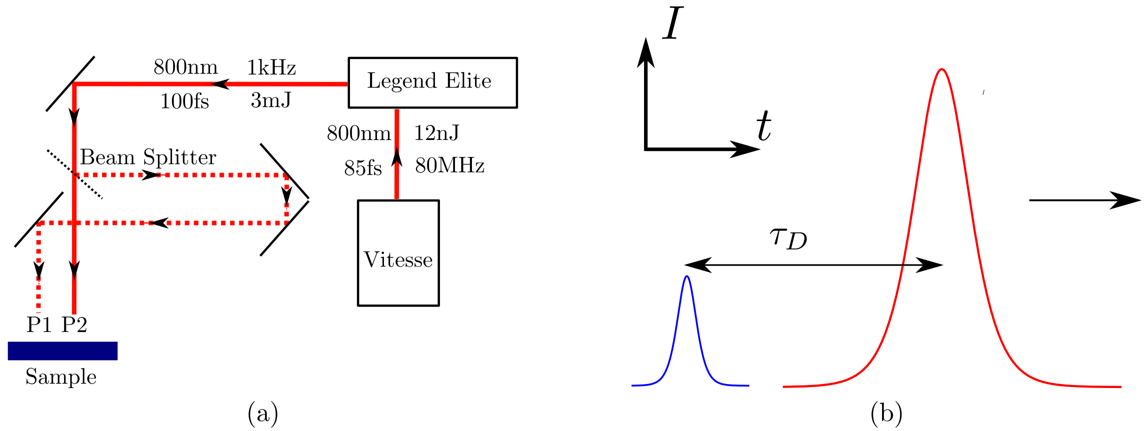

Figure 2.8: (a) Diagram of the laser amplification system with a pulse splitting and delay system showing 2 beams P1 and P2 delayed by the addtional path in P1. (b) Diagram showing the two pulses in a pump probe experiment with a delay of τ_D.

(Coherent Legend Elite) as shown in figure 2.8. A Coherent Vitesse produces 12nJ pulses of length 85fs at a repetition rate of 80kHz these are directed into the amplifier where they are stretched in time to lower the instantaneous power and single pulses are selected. These are then entered into the cavity at a much lower rate of 1kHz. Multiple passes through the optically pumped Ti:sapphire gain medium, amplify the pulse energy to 3mJ. At which point the pulses are switched out of the cavity by a polarisation change into the experimental setup.

Chapter 3

Heat Dissipation Mechanisms in Graphene

This chapter is based on the work contained in reference [37] The majority of data were taken and analysed by S.Hornett; some additional data was taken with A.S.Price. The theory was developed with A.Shytov.

3.1 Introduction

In this chapter low temperature electrical conduction in graphene monolayers on silica substrates is studied. A non-linear dependence of the resistance on applied DC bias is seen at temperatures <70K. This non-linearity mansifests itself as a peak centered around zero bias. The peak can be attributed to self heating of the charge carriers and its shape can be described by different mechanisms of heat loss. The energy loss properties have been of interest in the literature with a number of papers measuring current saturation in graphene flakes at high bias and temperature >150K. This saturation has been attributed to; ripples [36] ,remote interface phonons [38, 39] and optical phonons in the graphene sheet [40]. In this chapter these energy loss mechanisms are investigated but at much lower temperatures and biases. In order to understand the heat transport properties of graphene monolayers a thorough consideration of the different electron phonon coupling mechanisms must be made. The system under consideration is a monolayer flake on a doped silicon/300nm silicon dioxide substrate as described in figure 2.1. The samples are electrically contacted with gold wires and are mounted on a temperature probe in

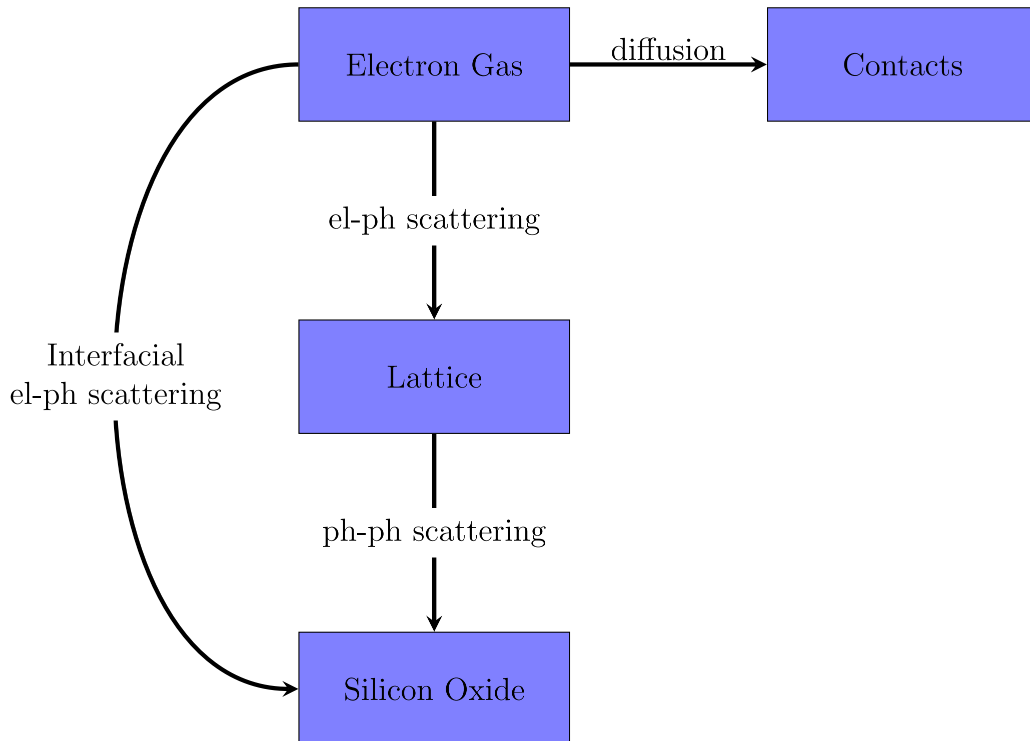

Figure 3.1: The various tis controlled byhermal reservoirs and the coupling mechanisms between them in a standard graphene sample shown in figure 2.1.

an atmosphere of helium, liquid helium or vacuum. The graphene flake on the substrate is considered as a system of connected thermal baths each with a characteristic temperature as shown in figure 3.1. By application of a current to the device heat will be generated within the electron system via the mechanism of Joule heating. The expected final temperature of that electron system can be calculated by a heat balance between Joule heat generated and heat loss mechanisms schematically in figure 3.1 the heat reservoirs are shown as blue boxes with the various heat transfer mechanisms under study defined by the arrows between the reservoirs.

By measurements of the temperature dependence of the graphene resistance $R(T)$ and of the DC bias dependence $R(V)$ the important factors governing heat dissipation through the system are ascertained.

3.2 Samples and Measurement Technique

In this chapter the results of two representative samples fabricated by electron beam lithography on the standard silicon dioxide substrate will be presented. Sample A is $3.7\mu m$ wide and $16\mu m$ long with a mobility of 5700 cm^2/Vs. Sample B is 4μm

wide and 16μm long with a mobility of 2500 cm^2/Vs. The samples were measured using a four terminal AC lock-in technique with a low current of 5nA ,determined as the point at which the voltage drop over the sample was linearly dependent on the current applied, to avoid unintentional heating.

The heating bias is applied in DC mode mixed prior to the sample using the circuit shown in figure 2.6 . The samples were confirmed to be single layer by using Raman spectroscopy and optical contrast measurements.

In order to ensure that the measurement current is not causing unintentional self heating the current is selected so that a doubling of the current causes a doubling of the voltage. The frequency of the AC voltage was selected to fulfil a number of conditions, including the avoidance of significant capacitative leakage through the pF capacitance of the coaxial cables and wiring into the probe. Additionally a noise spectrum was taken and the frequency is set at $\sim$17Hz to avoid any large noise spikes such as the 50Hz mains signal. The measurement system consisted of a long probe with the sample mounted at the very end, the current leads to the sample are thermally anchored along the probe length to ensure adequate cooling of the system. The substrate and sample were for sample A mounted within a vacuum chamber pumped to $< 10^{-5}$mbar. For sample B the sample was measured in a helium transport dewar where the atmosphere is helium gas at temperatures above 4.2K and liquid helium below 4.2K.

3.3 Contact Pinning

In this chapter a temperature profile over the flake will be calculated. In order for this calculation to be done the boundary conditions must be known. There are two scenarios; in the first the sample cooling is dominated at the large source and drain contacts with the smaller voltage probe contacts having a small effect on the temperature, secondly if all the contacts cool equally well and the boundary temperature is pinned at the voltage probes. In figure 3.2 a large multi terminal sample was measured in which the voltage probes V_A and V_B measured were kept constant and the source and drain contacts $V_{S1,S2,S3}$ were varied along the flake changing the source drain distance between 25 and 50μm. The lack of dependence of $R(V_{AB})$ on source drain distance as shown in figure 3.2 suggests that the voltage probe contacts

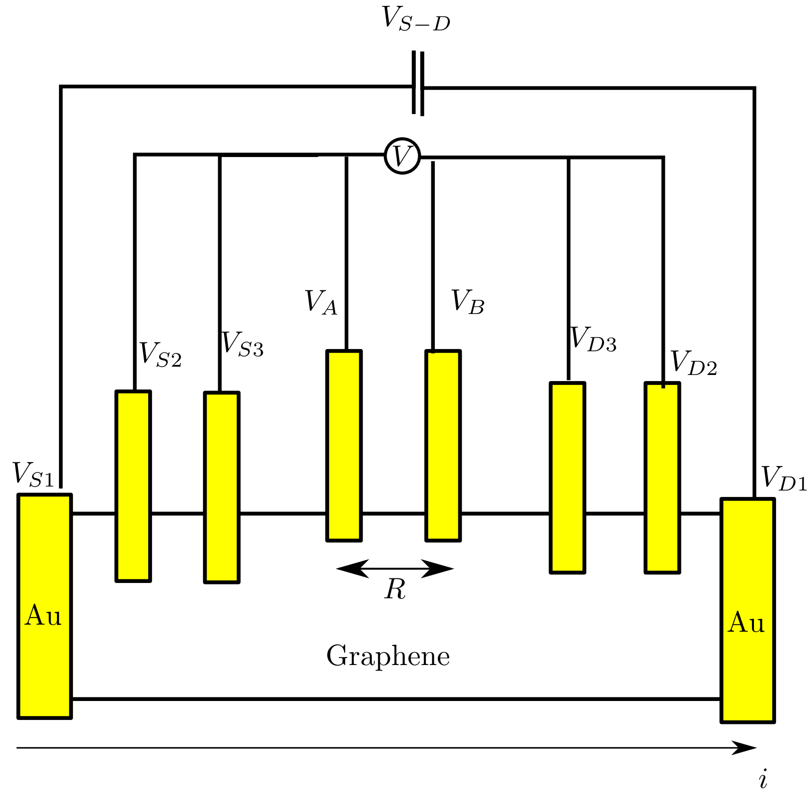

(a)

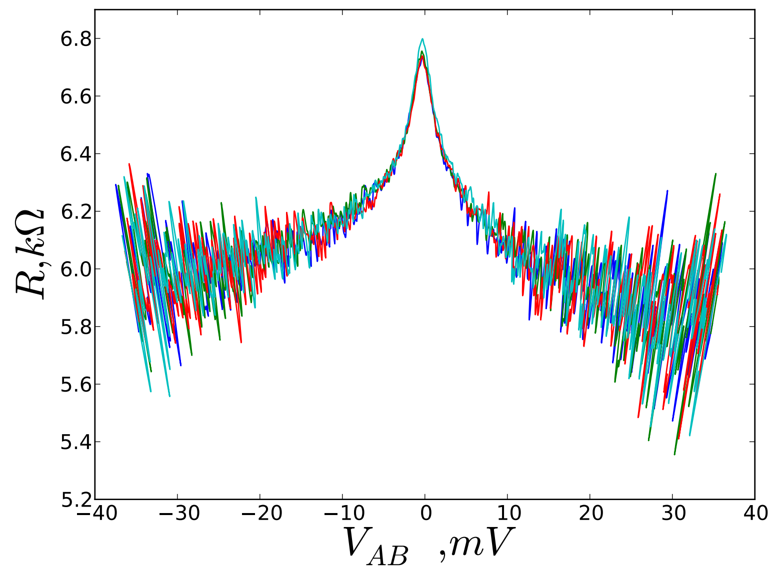

(b)

Figure 3.2: (a) Probe configuration (b) Resistance as a function of source drain bias between contacts V_A and V_B measured for different source drain contacts $S_{(1,2,3)}$ and $D_{(1,2,3)}$. Each colour denotes a different contact pair.

are perfectly cooling to the temperature of the bath: in this case $4.2K$. In the samples a dependence on the contact overlap with the graphene conductive channel did not seem to vary this picture. In general this may not be true in very large samples or samples with etched graphene leads extending far from the conductive channel because of over increased distance from the gold contact a temperature gradient can be maintained leading to a much higher temperature.

3.4 Comparison of temperature profiles with data

In figure 3.3 two broadly similar plots are shown: figure 3.3a is the voltage dependence of the resistivity and figure 3.3b the temperature dependence of the zero bias resistivity. The starting assertion is that the similarity between the two curves is related, as we increase the source drain bias Joule heating increases the temperature of the electrons. This temperature increase causes the resistance to vary in the same way as figure 3.3b. The resistance peaks in both temperature and source drain bias dependences exhibit a change of $\approx 1k\Omega$. Furthermore the peak seen in the temperature dependence (figure 3.3) is only seen in the source drain bias dependence at bath temperatures below $T = 30K$ the point at which the turnover of the $R(T)$ occurs. The similar shape of both the curves combined with the temperature dependence suggest the resistance originates from hot carriers excited by the source drain bias.

In order to interpret the curve shown in figure 3.3a we must not only develop a model to predict heat flow around the system but must be able to compare that with the resistance dependence of the applied source drain bias. The temperature dependence of the resistance (fig 3.3b) measured using a small measurement current(5nA),in order to avoid overheating, can be used as a conversion between temperature and resistance.

3.5 Simple Temperature Model

To confirm the overheated electron hypothesis both the production and distribution of Joule heat must be characterised. In our system there are a number of characteristic lengths: the elastic impurity scattering length l, electron-electron scattering length l_{e-e} and the electron-phonon scattering length l_{e-ph}. At low temperatures

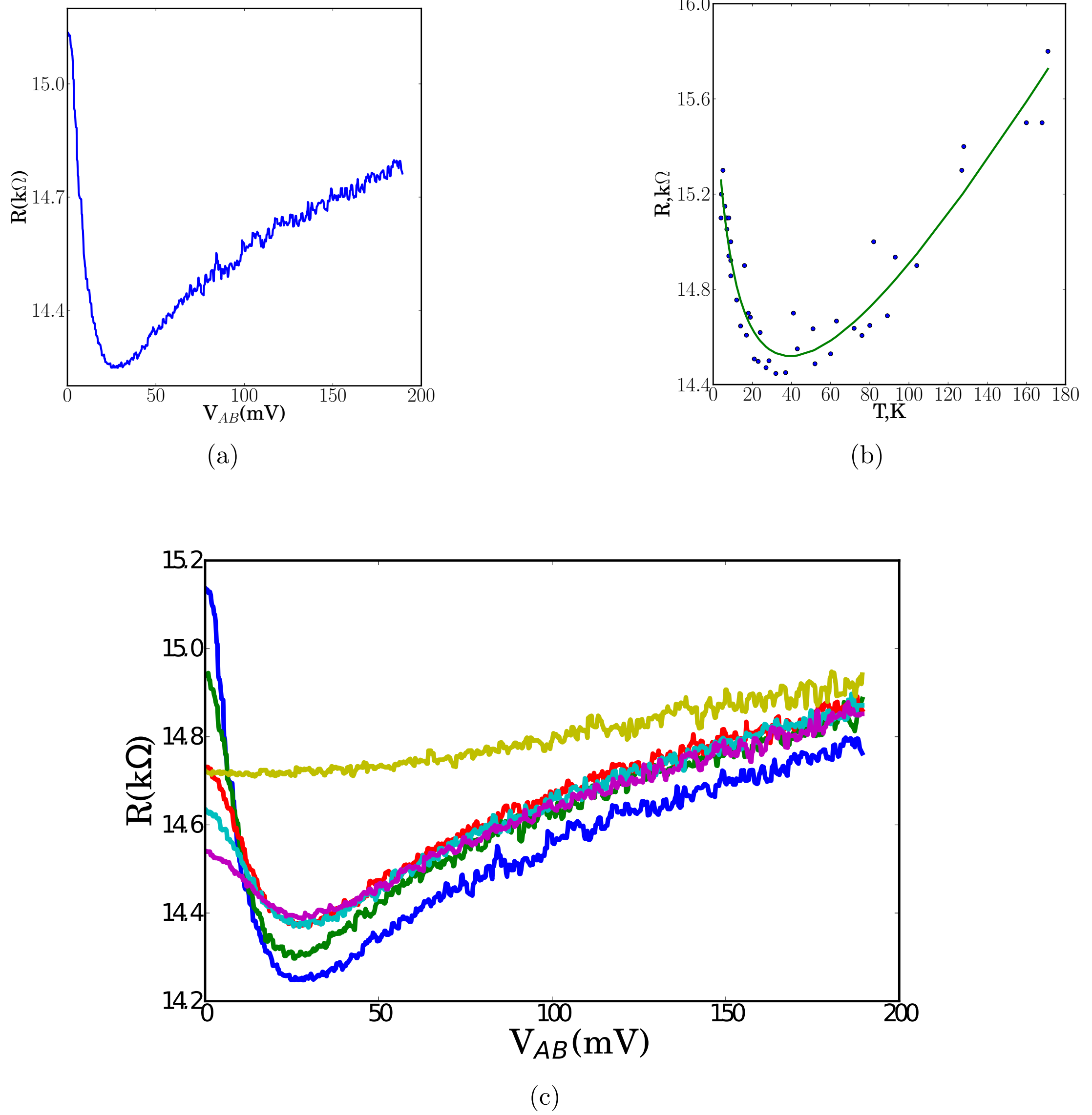

Figure 3.3: Sample A at V_g=3V. (a) Resistance as a function of applied DC bias at T_{bath} =4.2K. (b) Dependence of the zero bias resistance on bath temperature. Green line is a guide to the eye. (c)Source drain bias dependence of the resistance at multiple bath temperatures showing the suppression of the peak at higher temperatures. Different bath temperatures are shown as 4.2K(blue),15K(green),26K(red),35K(turquoise),83K(purple),107K(yellow)

inelastic processes are suppressed by the lack of available states to scatter into , Pauli blocking, and the characteristic states form a hierarchy $l \ll l_{e-e} \ll l_{e-ph}$ where $l \approx$ 10nm. l_{e-e} can be calculated from the electron-electron scattering time $l_{e-e} \approx \sqrt{D\tau_{e-e}} \approx 1\mu$m at V_G =3V where τ_{e-e} is approximated as $\hbar E_f/(k_B T)^2$

By evaluating how the sample length L compares with these scattering lengths we can determine the regime a particular sample will be in. Samples of length $L < l < 10nm$ will have no Joule heat generated as no inelastic processes can distribute energy between the electrons.

When $l < L < l_{e-e}$ Joule heat is generated within the electron bath. There is no cooling due to electron phonon scattering because $L \ll l_{e-ph}$. Assuming that the resistance profile depends solely on the electron temperature, then the minimum in resistance can be assigned a temperature. Therefore, the electron temperature at the minimum in $R(T)$has a value of T_e = 40K. This allows the minimum in $R(V)$ to tentatively be assigned the same temperature. The radiative heat loss to the environment can be calculated and be compared with the Joule heat generated to see if radiative heat loss is an important mechanism in these systems. The heat loss due to radiation from the sample assuming the sample is a black body radiator $P = \sigma A T_e^4 \approx 10^{-12}$W where σ is the Stefan-Boltzmann constant and A the area of the sample. Comparatively the Joule heat generated is $P = V_{AB}^2/R \approx (35mV)^2/14\text{k}\Omega \approx 9 \times 10^{-8}$W which is 4 orders of magnitude higher power than can be dissipated by radiative losses therefore there must be a much stronger dissipative channel present.The only source of cooling remaining in our sample is electron diffusion into the contacts. This mechanism was considered by Rudin and Kozub [41] to calculate the electron temperature under an applied bias. The first step in this process is to calculate the electron temperature distribution along the sample. This is done by using a simple quasi one-dimensional heat balance model [41].

$$T_{el}(x) = \frac{\sqrt{3}}{2\pi}\frac{e|V_{AB}|}{k_B}\sqrt{1-\left(\frac{2x}{L}\right)^2}, \tag{3.1}$$

where V_{AB} is the voltage applied, L is the length of the sample and x is the distance along the sample from $-L/2$ to $L/2$. The assumption made here is that the only cooling is through the electrical contacts. This was shown to be the case in section 3.3. This model also assumes constant temperature with width and ignores the

change of resistance with temperature and therefore distance along the flake. An interesting point to note here is that the maximum temperature at the center is only dependent on the voltage applied.

The result of eqn 3.1 in figure 3.4a must be combined with the measured zero bias temperature dependence (Fig 3.3b) in order to compare with $R(T)$. It is worth noting that the lattice temperature (T_{ph}) always equals the bath temperature T_B so in the overheated electron case $T_{el} \neq T_{ph} = T_{bath}$, whereas in the temperature dependence (Fig 3.3b), $T_{el} = T_{ph} = T_{bath}$.

The result of the combination of the temperature dependence and electron diffusion model is shown in figure 3.4b. It can be seen that as the voltage V_{AB} rises the resistance in the centre of the flake decreases. Integrating along each of the voltage steps gives the total resistance of the flake between voltage probes

$$R(V_{AB}) = \frac{1}{L} \int R[T_e(x)]dx \ . \tag{3.2}$$

The dependence of this integral on voltage is shown compared with data at V_G =3V in figure 3.4c. The asymmetry between positive and negative voltage sweeps in the curve is attributed to the additional gating effect in which the effective gate voltage varies as a function of distance along the flake $V_{\mathrm{Eff}(X)} = V_G(X) + V_{SD}(X)$. Typically in transport experiments $V_{SD} \ll V_g$ but when a larger source-drain bias is used the regime $V_{SD} \approx V_g$ can be realised. In this regime the source drain bias can modulate the concentration and the direction of asymmetry in the resistance curve will depend on the position of the Fermi level and the direction of the source-drain bias.

Figure 3.5 shows that direction of the asymmetry correlates with Fermi level position switching signs on opposite sides of the Dirac point. The asymmetry in the data is then removed by a simple symmeterization procedure in which

$$R_s(V_{AB}) = \frac{R(V_{AB}) + R(-V_{AB})}{2} \ , \tag{3.3}$$

leaving only the symmetric change in resistance note the change to V_{AB} as this is done with the voltage drop between the contacts rather than the applied bias between source and drain.

Figure 3.6 shows the comparison of $R(V_{AB})$ at different concentrations in sample

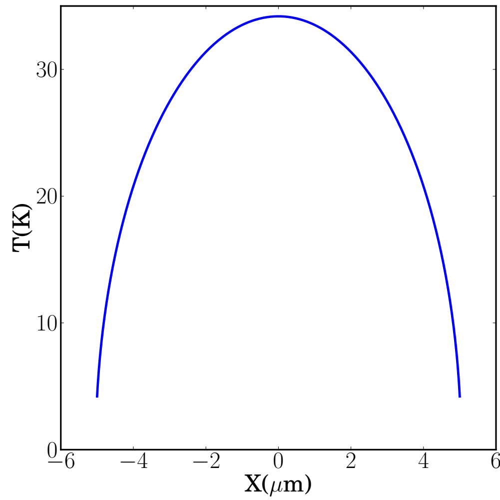

(a) Temperature profile along the sample at 2mV according to Eqn 3.1. The temperature is pinned to T_{bath}=4.2K at either end.

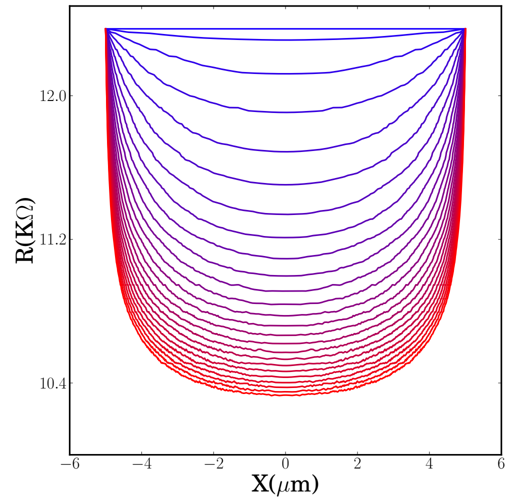

(b) Resistance profile along the sample at values of V_{AB} from 0 (blue) to 10mV(red) in 0.4mV steps.

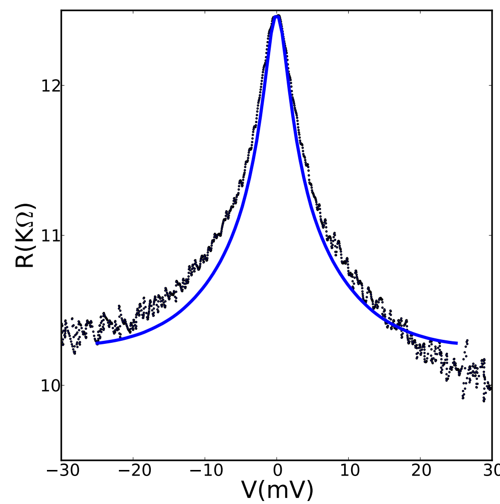

(c) Dependence of the Resistance on V_{AB} for sample B at V_g=3V (black dots). Fit due to electron diffusion (blue).

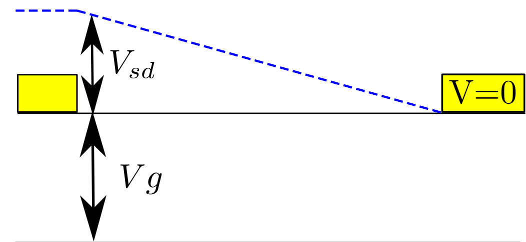

(d) Figure showing the effective gate voltage (blue dashed line) as a function of distance x along the flake.

Figure 3.4

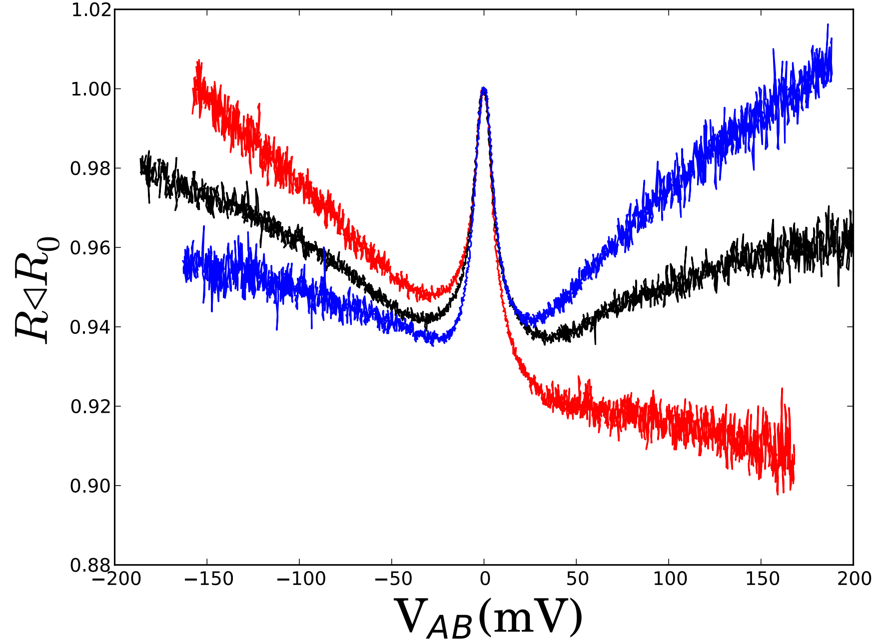

Figure 3.5: Figure showing the direction of the asymmetry in V_{AB} dependent on the gate voltage . -3V,0V and 3V with respect to the Dirac point are coloured respectively red,black and blue.

B with the fits generated by eqns 3.2 and 3.1. These describe well the central peak of the $R(V_{AB})$ This confims electron diffusion as the dominant cooling mechanism in the 10μm sample. This suggests the ineffective cooling of the carriers through electron-phonon relaxation. A poor cooling to phonon modes in turn suggests the length of the sample is small compared with the electron-phonon scattering length.

3.6 Heat Transport Model

In order to probe electron-phonon relaxation, a longer sample is taken and as can be seen in figure 3.7 the fit based on electron diffusion alone (solid blue line) is clearly inadequate to describe the data shown. The upturn in resistance in the calculated $R(V)$ in figure 3.7, increases at a much greater rate than the measured $R(V)$ curve, additionally the upturn proceeds the data in V_AB . This indicates that the electron temperature is overestimated by the purely diffusion based model and an additional source of cooling is present. To account for this disagreement cooling via electron phonon scattering can be included. The strength of the cooling will depend on two factors: the electron-phonon scattering time balanced with the number of scattering events that can take place along the sample. Transport measurements

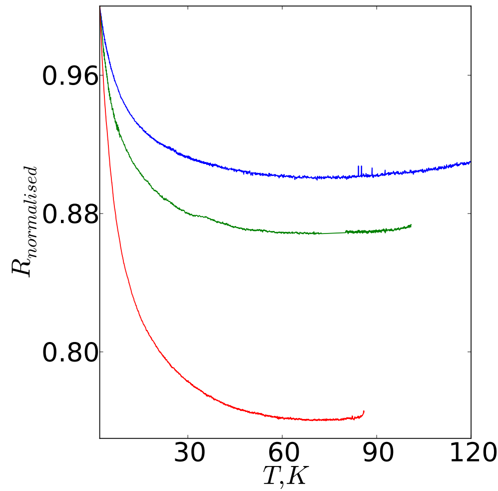

(a) Temperature dependence of the resistance at zero bias. Curves have been normalised for easy comparison between concentrations -3V (red),-10V (green),-16V (blue)

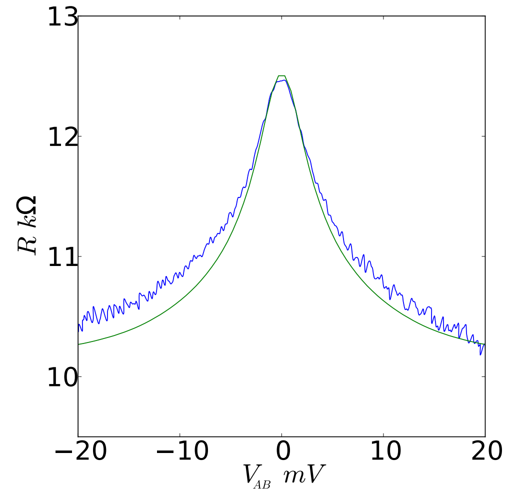

(b) -3V

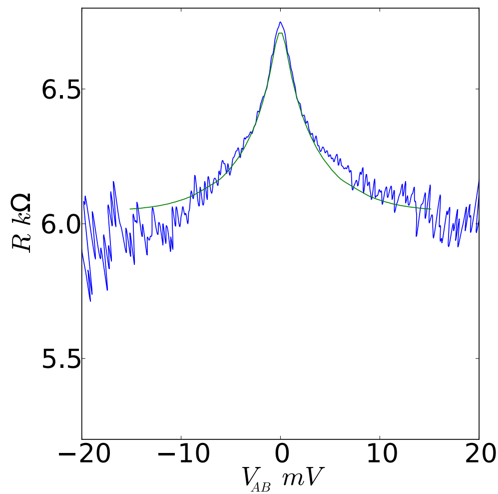

(c) -10V

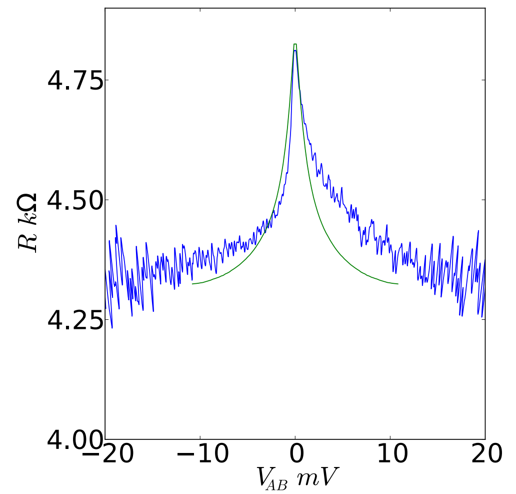

(d) -16V

Figure 3.6: Comparison of the eqn 3.1 with measured data for different concentrations in sample B

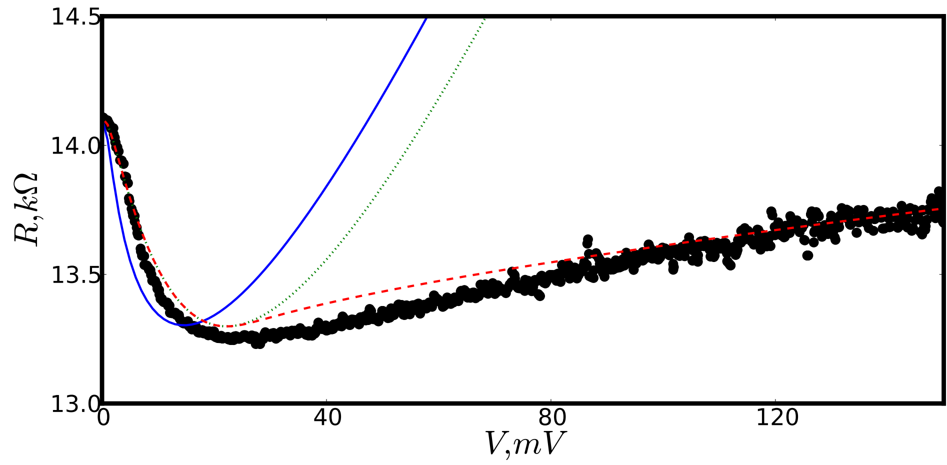

(a) 3V

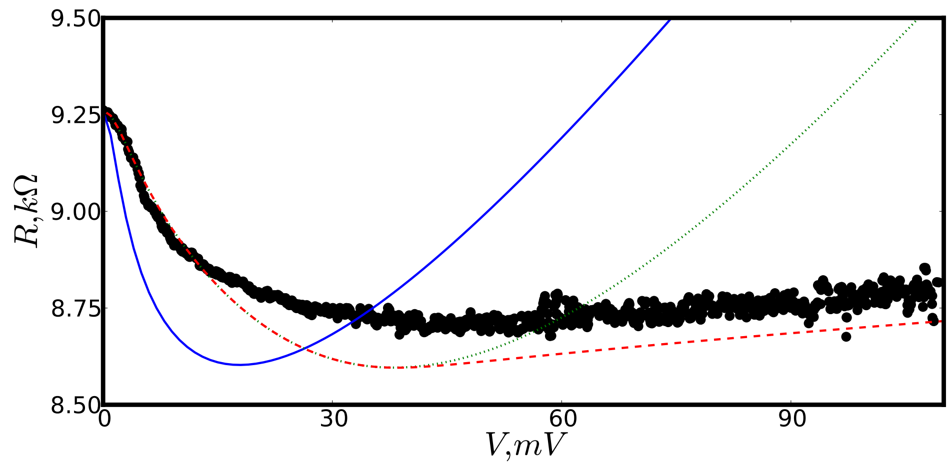

(b) -6V

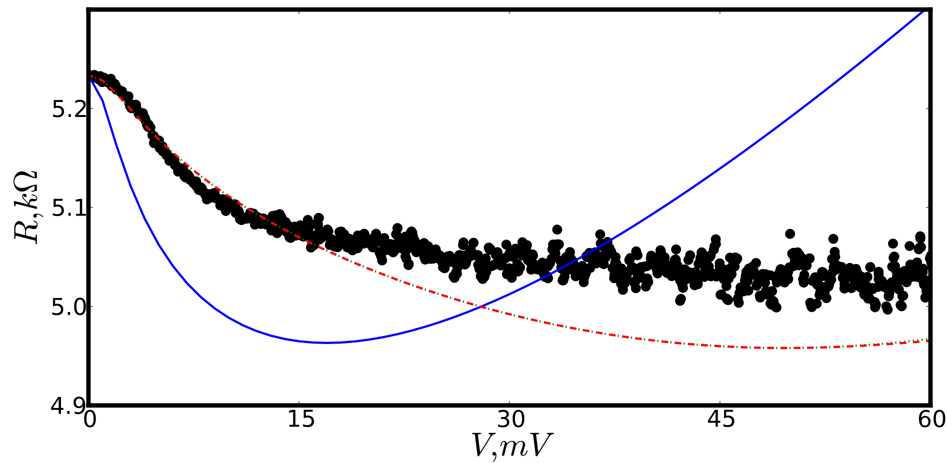

(c) -12V

Figure 3.7: Sample A (16μm) showing source drain bias dependence of the resistance at different gate voltages. Smooth curves correspond to the three different calaculations with no phonons (solid blue), acoustic phonons only (dotted green) and acoustic phonons with remote interface phonons(dashed red)

have previously shown that optical phonons either in the silicon dioxide substrate or the graphene lattice do not significantly contribute to transport properties below 200K [38]. Therefore, only acoustic phonons will be initially considered.

To calculate the temperature in the sheet including phonon scattering a heat balance equation is used in which the flow along the sheet will be calculated with an additional loss term to phonons

$$\frac{\delta Q}{\delta x} = \frac{V^2}{\rho L^2} + \left(\frac{dE}{dt}\right)_{\mathrm{ph}} , \tag{3.4}$$

where Q is the heat flux, $V^2/\rho L^2$ is the Joule heat generated, ρ is the electrical resistivity and $(dE/dt)_{\mathrm{ph}}$ is the energy dissipation to phonons. The boundary conditions $T_e(x = \pm L/2) = T_{\mathrm{bath}}$ are imposed assuming complete cooling at the contacts. The heat flux is defined as

$$Q = \kappa(T)\frac{dT_e}{dx} , \tag{3.5}$$

where $\kappa(T)$ is the electronic thermal conductivity given by the Widermann-Franz law: $\kappa = \pi^2 k_B^2 T_e / 3e^2\rho$.

Equation 3.5 cannot be solved analytically as the heat flux to phonons now depends on the current electron temperature. Therefore, a heat equation is given as

$$\frac{\delta U_e}{\delta t} + \frac{\delta Q}{\delta x} = \frac{\sigma V_{\mathrm{sd}}^2}{L^2} + \frac{dE}{dt} \tag{3.6}$$

with the boundary conditions given by $T_e(-L/2) = T_e(L/2) = T_{\mathrm{bath}}$ which describes the clamping of the electron temperature by the gold contacts. The equation is then solved by an iterative procedure on a 100 point grid. The differences between the voltage overheated electrons and the temperature dependence with a thermalised bath must be a appreciated. In the voltage overheated case, the thermal heat capacity of the electrons, calculated in section 1.2.1, is smaller than the phonon heat capacity $C_e(\propto T) \ll C_{ph}(\propto T^2)$ at all relevant temperatures. This leads to some simplification as a heat will only flow from the electron bath into the lattice which will remain in thermal equilibrium with the substrate at the bath temperature T_{bath}.

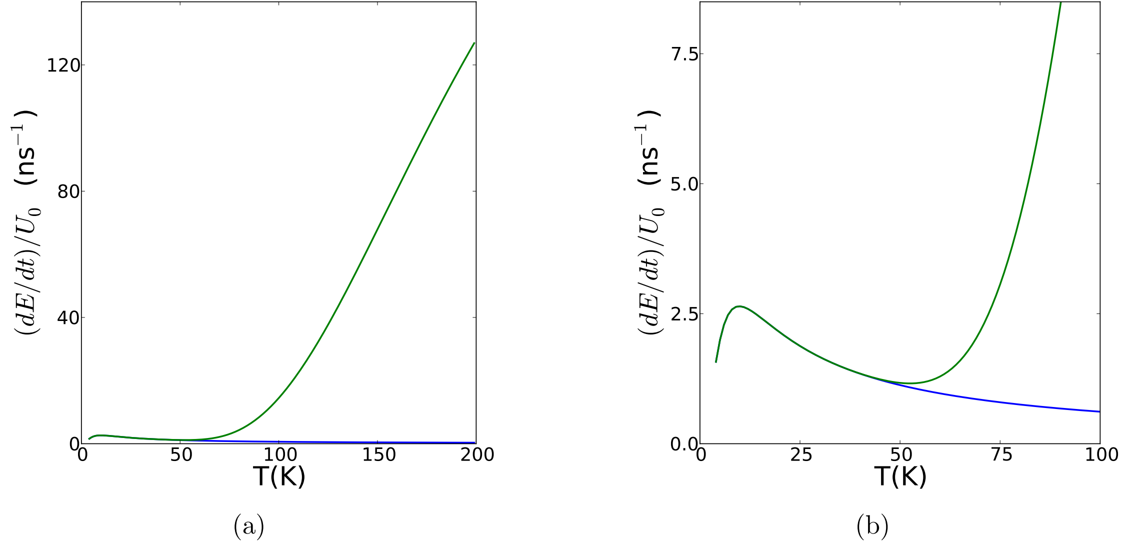

Figure 3.8: The rate of energy loss to phonons as a function of temperature. Blue curve shows the rate of energy loss to acoustic phonons in the graphene sheet. Green curve shows the rate of energy loss to acoustic phonons and remote interface phonons. These processes happen on different timescales (b) showing the low temperature region in greater detail than (a).

3.6.1 Acoustic Phonons

The heat balance the energy dissipation due to acoustic phonons is [42, 43]

$$\left(\frac{dE}{dt}\right)_{\text{ac}} = -\frac{D_a^2 K_B E_f^5}{2\varrho\hbar^5 v_F^8} \,, \tag{3.7}$$

where D_a is the deformation potential, $\varrho = 7.6\times10^{-7}kgm^{-2}$ is the areal mass density and $v_s = 2\times10^4 ms^{-1}$ is the speed of sound in graphene. The ratio of equation 3.7 to the total energy in the electron bath $U_e \propto T_e^2$ gives a characteristic timescale over which the system relaxes. Figure 3.8 shows this ratio as a function of temperature, the peak that can be seen around 10K is due to acoustic phonons. The peak is determined by the maximal energy that can be lost by an electron in an electron phonon scattering event . Normally in 3D metals all populated phonon modes below the Debye temperature determined by $k_{ph} = k_BT/\hbar v_s$ can scatter with electrons [44]. In graphene the maximal momentum is limited by backscattering events crossing the entire Fermi surface, $2\hbar k_F$ [45]. This limits the scattering potential to a much smaller fraction of the total phonon population. The temperature at which the scattering changes from being Fermi surface size limited to phonon population limited is known

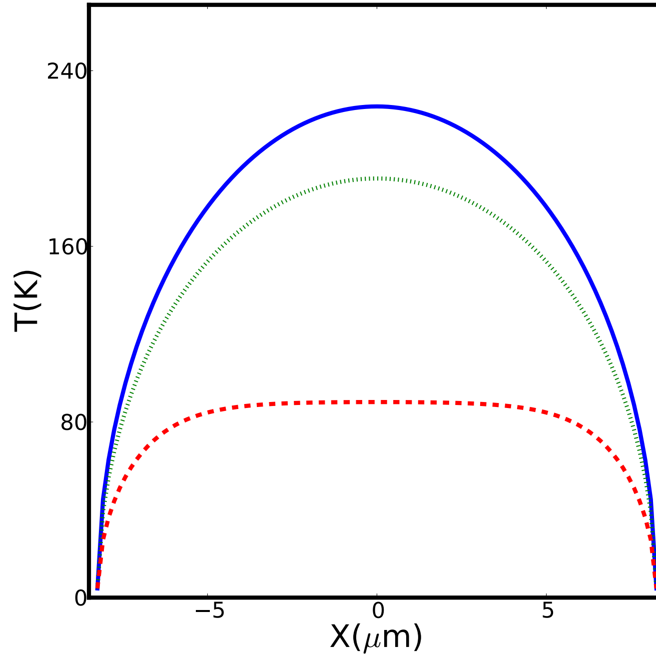

Figure 3.9: Temperature profile along the length of the sample for the three separate models; no phonons (solid blue), acoustic phonons only (dotted green) and acoustic phonons with remote interface phonons(dashed red) at an applied source drain bias of 70mV, a gate voltage of 3V and a bath temperature of 4.2K.

as the Bloch-Grüneisen temperature, and is given by

$$T_{BG} = 2\hbar v_s k_F / k_B \ . \tag{3.8}$$

At temperatures below T_{BG} the cooling is very effective and as the temperature rises the number of available phonon modes increases. Above the saturation point at T_{BG} the total energy in the system continues to rise with the temperature whilst the bottleneck in phonon relaxation causes the energy loss mechanism to become increasingly inefficient. Cooling then relies on multiple scattering events which are limited by the length of samples and the electron phonon scattering time.

Taking Eqs. 3.4 and 3.7 the temperature dependence including phonons can be calculated and is plotted in figure 3.9. The largest additional cooling occurs in the center of the flake far from the contacts. The temperature profiles are calculated including acoustic phonons and the resulting $R(V_{AB})$ curves are plotted in figure 3.7(dotted green) at a number of different concentrations. When calculating the electronic temperature two values of the deformation potential D_a are used for the low concentration ($V_g = 3V$) regime $D_a = 18$eV and at higher concentrations $V_g =$

$-6V, -12V$ a value of $D_a = 21eV$ is taken [46].

3.6.2 Remote Optical Substrate Phonons

Figure 3.7 shows that in comparison to the pure electronic diffusion model including acoustic phonon scattering improves the fit in the low bias regime correctly identifying the upturn in resistance. However as the bias increases a much sharper upturn is seen in the model compared with the data. This suggests an additional cooling mechanism at higher electron temperatures $T_e > 70$K. Optical phonons in the graphene have already been discounted due to the ≈ 200 meV energy scale required to excite them. In this system there are also optical phonons at the silicon dioxide interface which have a lower energy, 59meV. Due to the two dimensional nature of the graphene sheet the exponentially decaying fringing electric field associated with these remote interface phonons (RIPs) extends through the graphene sheet giving a coupling mechanism with which to lose energy. Scattering from these RIPs has been proposed to explain the temperature dependence of the graphene resistance at temperatures exceeding 200K [38].

In order to correctly include the energy loss to the RIPs the scattering probability must be considered. Reference [39] describes a method for calculation of the scattering rate and this is taken as a starting point for the calculations. Additionally the effect of screening due the graphene charge carriers on the RIPs is considered. They are included by introduction of an effective dielectric constants $\epsilon_s, \epsilon_\infty$ at low and high frequencies respectively in the region directly above the SiO_2 surface which modifies the dispersion of the RIPs and gives an angular dependent scattering correction.

The energy loss term can be written as an integration over all energy as

$$\left(\frac{dE}{dt}\right)_{\text{opt}} = -\int \frac{4d^2\mathbf{p}}{(2\pi\hbar)^2}\frac{d^2\mathbf{p}'}{(2\pi\hbar)^2}\hbar\omega_{\text{eff}}(k)W_{\mathbf{p}\to\mathbf{p}'}f_{\mathbf{p}}(1-f_{\mathbf{p}'})\ , \tag{3.9}$$

where $W_{\mathbf{p}\to\mathbf{p}'}$ is the scattering rate and $f_{\mathbf{p}}(1-f_{\mathbf{p}'})$ gives the availability of the final state due to thermal broadening of states around the Fermi energy. The first two terms deal with the energy change associated with beginning and final states finally $\hbar\omega_{\text{eff}}$ is the energy associated with the interfacial phonon mode . Also note the lack of a phonon absorption term has been ignored due to the low temperature of

the substrate. By integration over all energy states the scattering angle dependent energy loss is found:

$$\left(\frac{dE}{dt}\right)_{\text{opt}} = -\frac{\pi\nu^2 e^2 v_s \beta(\hbar\omega_s)^3}{\epsilon_F}\int_0^{\pi}\frac{2\sin\frac{\theta}{2}\cos^2\frac{\theta}{2}d\theta}{e^{\hbar\omega_{\text{eff}}(2k_F\sin\frac{\theta}{2})/k_BT_e}-1}\times\frac{(2\sin\frac{\theta}{2}+\frac{q_s}{\epsilon_s+1})^{1/2}}{(2\sin\frac{\theta}{2}+\frac{q_s}{\epsilon_\infty+1})^{5/2}}, \tag{3.10}$$

where ω_s is the surface optical phonon frequency,q_s the surface optical phonon momentum and β is a coefficient dependent on the effective dielectric constant. The energy loss term is dominated by an exponential T_e dependence vanishing at low T_e but at high temperatures (≈70K) the RIP loss term becomes dominant, as shown in figure 3.8. The screening affects the results through a suppression of ω_{eff} at small θ. This acts to enhance the scattering at small k leading to an approximate twofold change in the cooling rate. Figure 3.6 shows the $R(V)$ curve (dashed red) including all the phonon modes indicating that the inclusion of the screening is necessary to fully describe the thermal properties of the graphene and gain good agreement with experiment.

3.7 Conclusions

In this chapter it has been shown that in order to accurately describe the electron temperature of an overheated system there are a number of regimes that must be considered. A low temperature regime where the dominant cooling mechanism can be described by electron diffusion to contacts. As the temperature rises graphene acoustic phonons become important. At larger temperatures substrate scattering from RIPs dominates due to the proximity of the electrons in the graphene to the substrate. This suggests that choice of substrate is important when constructing graphene devices and choosing a material with a high substrate interfacial phonon energy could reduce the coupling leading to higher electron temperatures.

Chapter 4

Quantum Corrections to the Conductivity in a High Electric Field

It has been suggested that the quantum corrections to the conductivity at low temperatures (which in Chapter 3 were the origin of the temperature dependence) could have a direct dependence on the electric field used to drive the current [47] in addition to the overheating effect. In this chapter measurements of the graphene conductivity at temperatures from 300mK to 20K under the application of an electric field are made. In two samples shown in table 4.1 measurements of the magnetoresistance will isolate the effect of the weak localisation effect from the other quantum corrections and careful analysis of the weak localisation will allow the dephasing length L_ϕ to be extracted. In the scaling theory of localisation [48] each of the length scales discussed in this section will modify the nature of the conductivity correction. Some such as intravalley scattering preserve the coherence of the electron concerned whereas the dephasing length is linked with inelastic processes such as el-ph scattering putting an upper bound on the distance a coherent electron may travel. Previously in the lit-

Sample	A	B
Length	11μm	7.13μm
Width	4μm	4.2μm

Table 4.1: Table showing width and length between the voltage contacts for the two samples presented.

erature contradictory statements have been made. In reference [49] it was suggested that the electric field could directly dephase the electron over a characteristic length scale L_E. This measurement is dependent on the rate of heating of the electron gas to be small enough so that a large field can be applied without overheating the electron gas to a temperature at which the weak localisation is suppressed. These measurements were done in bismuth [47] and a silicon MOSFET [49] and in both these cases the experimental conditions under which an electric field induced dephasing were not reached due to overheating. In graphene, however, the weak localisation persists to much higher temperatures 30K [50] so even with the weak coupling to phonons in the substrate this direct field effect could be experimentally accessible. Additionally in the literature in sudies on two dimensional indium oxide films [51] a discrepancy was seen in two measures of the electron temperature suggesting a suppression of the dephasing length. This is contrasted with work by Altshuler et.al [52, 53] where consideration of the weak localisation problem under time reversal was considered. As the electric field does not break the symmetry between the forward and time reversed paths any additional phase shift due to the electric field should not cause dephasing even at very high values. Both these simple considerations do not include any higher order electron interaction effects and therefore may not fully describe the problem [54]. Therefore in this chapter measurements of the weak localisation under a large electric field will be made to attempt to reconcile these different ideas.

4.1 Field Dependent Weak Localisation model

The value of the electronic length L_E can be derived by comparison of two energy scales. The first is the energy acquired by an electron travelling in an electric field F over a distance L

$$E_E = eFL \ . \tag{4.1}$$

The second is the Thouless energy defined as the energy scale associated with the diffusion of electrons over distance L

$$E_T = \frac{\hbar D}{L^2} \ . \tag{4.2}$$

By equating these two terms a characteristic length can be defined above which the energy gained from the electric field must be considered

$$L_E = \left(\frac{\hbar D}{eF}\right)^{1/3} . \tag{4.3}$$

The possibility to see this length realised in experiment depends on its size relative to the dephasing length. An added complication is the increase of the electron temperature with the electric field as this will act to reduce the dephasing length. In graphene there are a number of advantages over the previous measurements in the literature that fail to see the effect [49, 55]. Firstly the electron temperature is well defined and can be described by the work in the previous chapter and secondly graphene quantum effects show a surprising robustness at high temperatures above 30K [50] and even up to room temperature [56].

The first part of this chapter will deal with the intricacy of the measurement setup in order to get high quality magnetoresistance data. This will improve upon current techniques for separating the weak localisation from UCF in small samples. The second part of the chapter will use the Hall effect to define the exact carrier concentration in the sample and allow an accurate value of the diffussion coefficent D to be ascertained. The third and final part of the chapter will extract the dephasing length L_ϕ for the magnetoresistance data at different values of the bath temperature and applied electric field in an attempt to realise the condition $L_E \gg L_\phi$.

4.2 Averaging of the Universal Conductance Fluctuations (UCF)

Once the temperature of the system drops below a few Kelvin the effect of UCF becomes very strong. These reproducible fluctuations in the conductance of the sample can change the resistance by the same order as the weak localisation signal. As a coherent phase effect like the weak localisation the fluctuations will appear in any measurement which changes the nature of the coherent regions such as applying a magnetic field (changes phase), changes in the Fermi level (changes scattering centres) and changes in temperature (reduces coherent area). The effect of the UCF can be seen with reducing temperature in Figure 4.1a. To average the UCF cannot be

done by time averaging as the UCF is robust as a function of time therefore a variable must be changed over which the UCF fluctuates. By varying the Fermi level over a number of fluctuations the average can be taken suppressing the UCF. Traditionally this is done by in weak localisation measurements sweeping the gate and averaging at a number of discrete points of magnetic field to produce the magnetoresistance curve. In this chapter the same effect was achieved by adding a small ac voltage (<1V,5Hz) to the gate voltage applied to the sample. This allows for the continuous curves seen in figure 4.1b with the only restriction that the sweep rate is small compared with the frequency at which the gate oscillates.

In doing this there are a couple of experimental challenges to overcome. By applying an AC gate voltage to the gate capacitor there is an increased leakage current due to the finite impedance of the gate which could overheat the electrons in the flake.

$$I_{\text{Leakage}} = V_{\text{ac}} C_{\text{gate}} \omega_{\text{ac}} \ , \tag{4.4}$$

where the capacitance of the gate can be calculated from the parallel plate capacitor model as

$$C = \frac{\epsilon_{\text{SiO}_2} \epsilon_0 A}{d} \ , \tag{4.5}$$

where $\epsilon_{\text{SiO}_2} = 3.9$ [57] is the relative permittivity of silicon dioxide, $d = 300nm$ the thickness of the silicon oxide layer. A is the area of the parallel plate capacitor which is naively the area of the graphene flake in the system $A = L_{\text{flake}} W_{\text{flake}} = 18\mu m \times 4\mu m = 7.2 \times 10^{-11} m^2$ in this case

$$I_{\text{Leakage}} = 8.3 \times 10^{-14}\text{A} \ . \tag{4.6}$$

The area could also be considered to include the contacts and the associated bonding pads this then gives a leakage area for a typical six terminal sample of $\sim 6 \times 10^{-8}\text{m}^2$ leading to a much greater leakage current of $I_{\text{Leakage}} = 7 \times 10^{-11}\text{A}$,which is still an order of magnitude under the lowest current used. The averaging effect of the AC gate bias is seen in Figure 4.1b where a small bias of 0.5V averages the UCF. Additionally no reduction in the peak height at the highest bias levels suggests no additional heating from any leakage current.

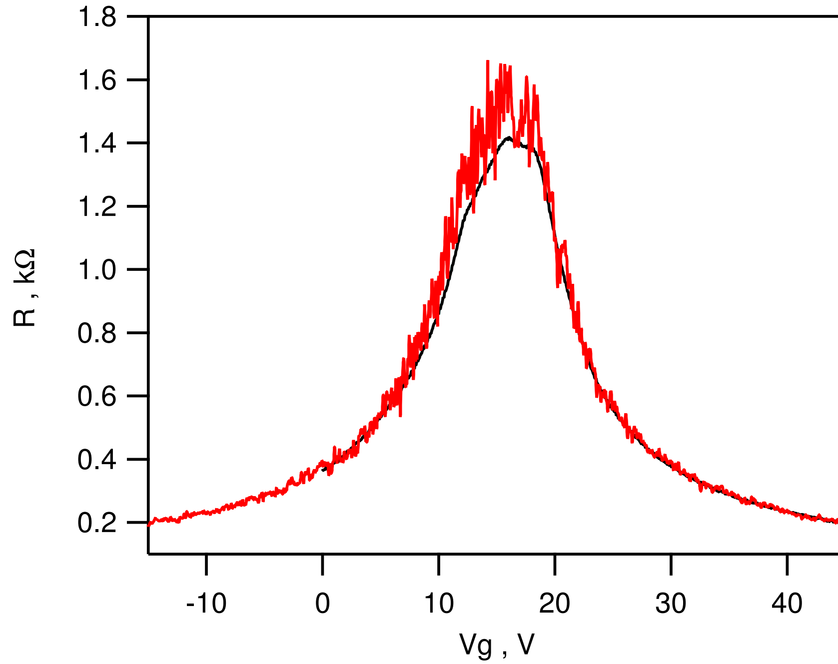

(a) Gate voltage dependence of the resistance at 7K(Black) and 50mK(Red) showing the appearance of strong universal conductance fluctuations.(Sample A)

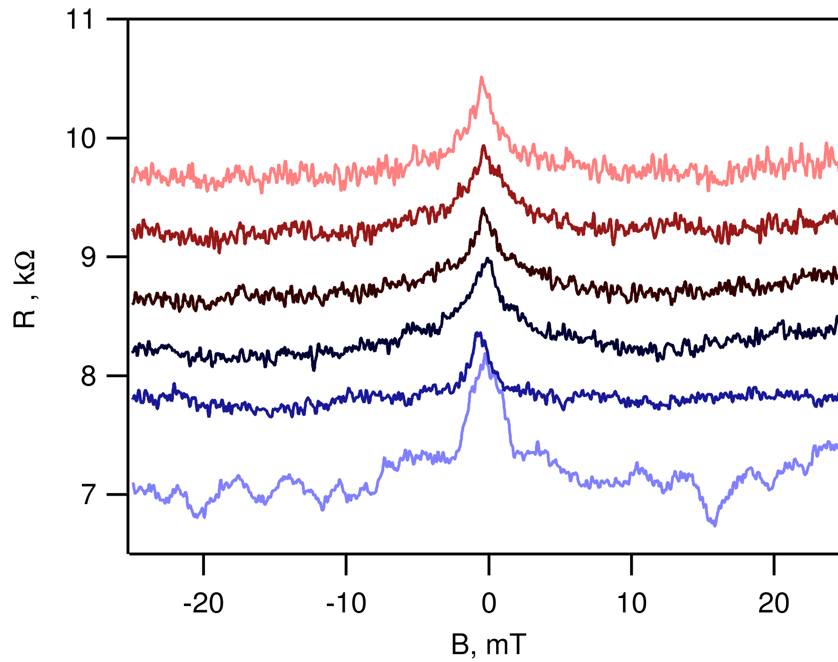

(b) Magnetoresistance curves at 50mK showing the averaging effect of applying an additional AC gate bias (5Hz). Increasing bias is shown in increasing steps of 0.5V from blue to pink with an offset of 0.5$k\Omega$ for clarity. A applied measurement current of 1.5nA was used. (Sample A)

Figure 4.1

4.3 Sample Characterisation

Measurements of the conductivity were performed at temperatures between 250mK and 50K using a pumped liquid He_3 system. This system must be warmed to room temperature approximately once a week to replenish the He_4 bath. Between cooling cycles there are small changes to the sample which are refected in changes in the UCF and small changes in the dephasing length. Where a specific measurement spans more than a single cooldown it will be noted in the text.

In these experiments the samples are measured in a constant current configuration figure 2.6 where a large ballast resistor $R_{\text{Ballast}} \gg R_{\text{Sample}}$ sets the current and any change in sample resistance during the measurement has a negligible effect on the size of the current flowing. In the previous chapter there a voltage bias dependent noise was present in the data. This is attributed to noise from the DC voltage source. This causes problems in the measurements, increasing noise combined with the shrinking magnitude of the quantum corrections makes extraction of important quantities difficult. In this chapter in order to provide a better signal to noise in the experiment the large electric field was applied AC. This gives a large signal to measure with the lock-in amplifier and significantly improves signal to noise. The AC nature of the excitation voltage can be discounted during analysis due to the large timescale associated with the change $1/17Hz = 55ms$. Using the relation $L = \sqrt{D\tau}$ gives a characteristic length of mm compared with the μm of the dephasing length and therefore in the timescales of interest the electric field experienced by an electron is essentially static.

To correctly analyse the quantum corrections to the resistivity there are a number of quantities that must be extracted. This section deals with each in turn starting with a determination of the carrier concentration and a check that the oscillating gate voltage does not significantly alter the carrier concentration. The carrier concentration is important to determine in graphene due to the dependence of the diffusion coefficient on the Fermi energy due to the changing distance travelled by carriers as the diffusion coefficient changes. This changing distance affects the flux enclosed by the weak localisation loops as well as the area of the minimum loop.

Figure 4.2a shows the transverse resistance of the graphene as a function of the magnetic field. In the classical Hall effect voltage builds up across the direction of

motion due to a transverse force applied by a perpendicular magnetic field. The Hall resistance is given as

$$R_H = \frac{V_y}{I_x} = \frac{B}{en} \tag{4.7}$$

so the Hall resistance should depend linearly on B and should have a gradient dependent on the carrier concentration n. There is a small offset in figure 4.2a due to two effects: residual magnetic field in the superconducting magnet and a small component of the longitudinal resistivity caused by an offset in the two voltage probes. Neither of these effects impact on the gradient and therefore are removed by the linear fit with an arbitrary offset. The observation that the offset remains constant with repeated magnetic field sweeps suggests the offset in the voltage probes as the likely cause. In figure 4.2b the extracted values of n are shown as a function of the gate voltage V_G applied. The $n = 0$ point is an independent measure of the position of the Dirac point which compares favourably with the peak in resistance seen in figure 4.1a. The coefficient between gate voltage and concentration can be measured and compared with the value from a parallel plate capacitor model of the gate which gives

$$\frac{n}{V_G} = \frac{\epsilon_{\mathrm{SiO_2}}\epsilon_0}{ed} \tag{4.8}$$

this leads to an extracted gate thickness of 325nm which is consistent with that suggested by the manufacturers of the substrate. The diffusion coefficient D needed for the magnetoconductance fits is then calculated using

$$D = \frac{\sigma\sqrt{\pi}\hbar v_f}{2\sqrt{n}e^2} \,. \tag{4.9}$$

4.4 Magnetoconductivity

Application of a magnetic field perpendicular to the sample using a superconducting magnet allows the weak localisation component to be isolated. The seperation is possible due to the independence of the Drude conductivity and the electron electron interaction on the magnetic field. The first effect which could affect the conductivity is the onset of Shubnikov de Haas(SdH) effect at fields above $\sim$0.5T. Although in

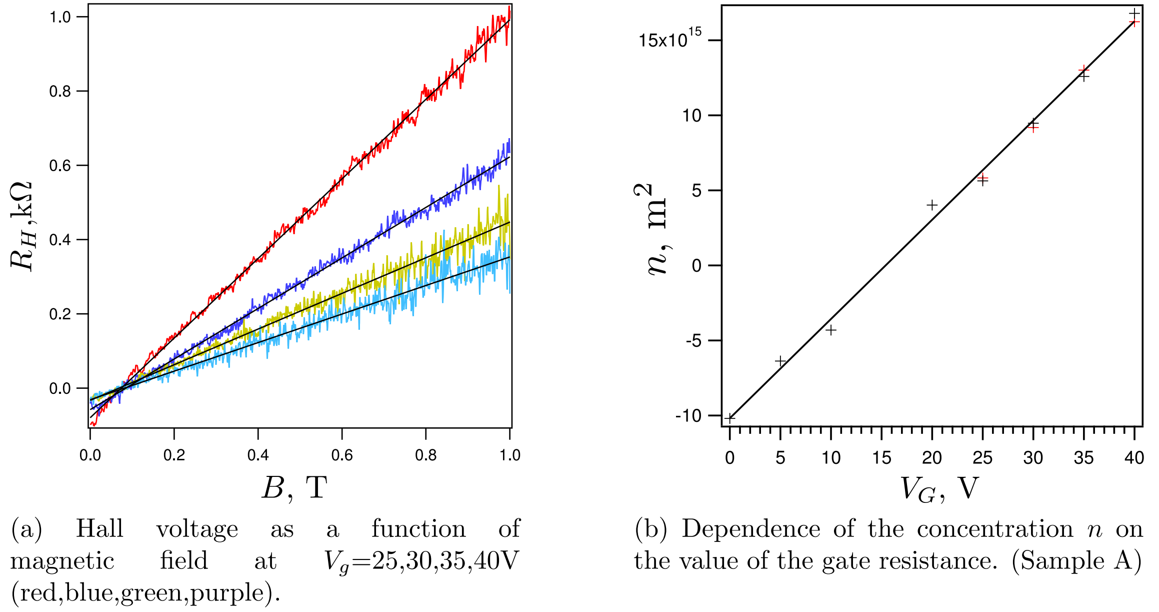

(a) Hall voltage as a function of magnetic field at V_g=25,30,35,40V (red,blue,green,purple).

(b) Dependence of the concentration n on the value of the gate resistance. (Sample A)

Figure 4.2: Using the Hall effect to determine carrier concentration by measurements of the Hall resistance at different values of the gate voltage V_G the slope of the dependence gives the carrier concentration shown in (b) as a function of the applied voltage. Crosses show the concentration derived from the gradient of the linear fit to the Hall resistance. Red and black crosses are taken with the oscillating gate on and off respectively. The black solid line shows a linear fit with a gradient of 6.6×10^{-14}m^{-2}/V. (Sample A)

practice the weak localisation is fully suppressed at the point a full quantum of magnetic flux is contained within the smallest weak localisation loop. This value of magnetic field is called the transport field and has a typical value of ∼20mT and within the range of samples tested is always smaller than the onset of the SdH oscillations.

Figure 4.3a shows the change of the magnetoconductivity as a function of bath temperature T_B. The change in conductivity is taken to isolate the effect of weak localisation from the constant Drude and electron electron interaction (EEI) terms. Raising the bath temperature in turn raises the electron temperature and leads to dephasing. As L_ϕ is suppressed there is a reduction in size of the central peak. Whereas the slope of the dependence at higher magnetic fields depends on the L_i and $L_\star$ lengths which are independent of temperature. Extraction of the dephasing length is done by first fitting using equation 1.38with the three characteristic lengths L_ϕ,L_i and $L_\star$ as free parameters with initial values of $L_\phi \sim 1{\times}10^{-6}$m, $L_i \sim 1{\times}10^{-6}$m and $L_\star \sim 300 \times 10^{-9}$m. This fitting is performed at the lowest temperature and then the values of L_i and $L_\star$ are fixed for the higher temperature curves. This gives

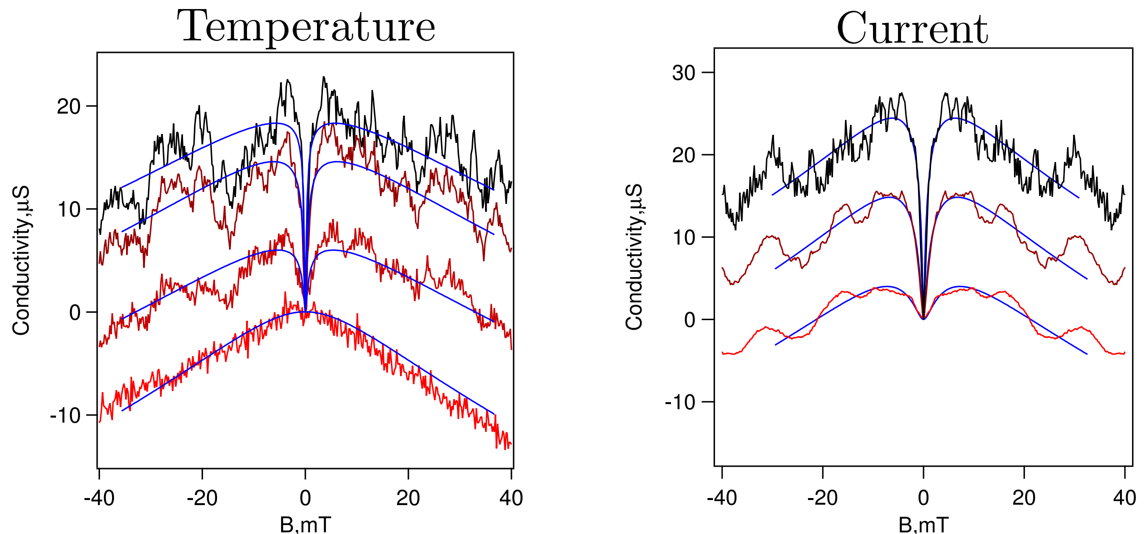

(a) Temperature Dependence (T_{Bath}) of the magnetoconductivity at a range of temperatures 0.25K,1K,4.2K and 24K(from black to red) showing the quenching of the weak localisation effect at high bath temperatures. Data was recorded with a excitation current of 1.3nA.

(b) Current dependence of the conductivity increasing from black to red (0.65nA,83nA,320nA) taken at the temperature of 0.25K.

Figure 4.3: Weak localisation in Sample B at a gate voltage of -3V.

a better fit throughout the temperature range and improves the error of extracting L_ϕ. Values of $L_i = 1.6\mu$m and $L_\star = 120$nm are extracted and compare well to values found in the literature [50, 58]. The same process is performed for each of the curves in figure 4.3b as the current is increased giving values of $L_\phi(T, I)$. Figure 4.4 shows the extracted values of L_ϕ as a function of the bath temperature at different excitation currents. A suppression of the dephasing length is seen with increasing current. If this is interpreted as an increase in electron temperature the temperature can be roughly estimated as the point where the a high current curve diverges from the 0.65nA curve. An important point here is that no saturation of the dephasing length is seen at the lowest values of the current suggesting there may be overheating even at these small currents. Another explanation for the large difference between 0.65nA and 1.3nA curves could be an shift due to a cycling of the temperature from room temperature back to 250mK that may have increased the dephasing length due to changes in the impurity configuration on the surface or a different occupation of charge traps in the substrate. Assuming an electron diffusion with phonon contributions as described in the previous chapter an effective electron temperature can be calculated for each of the current and base temperature configurations. By

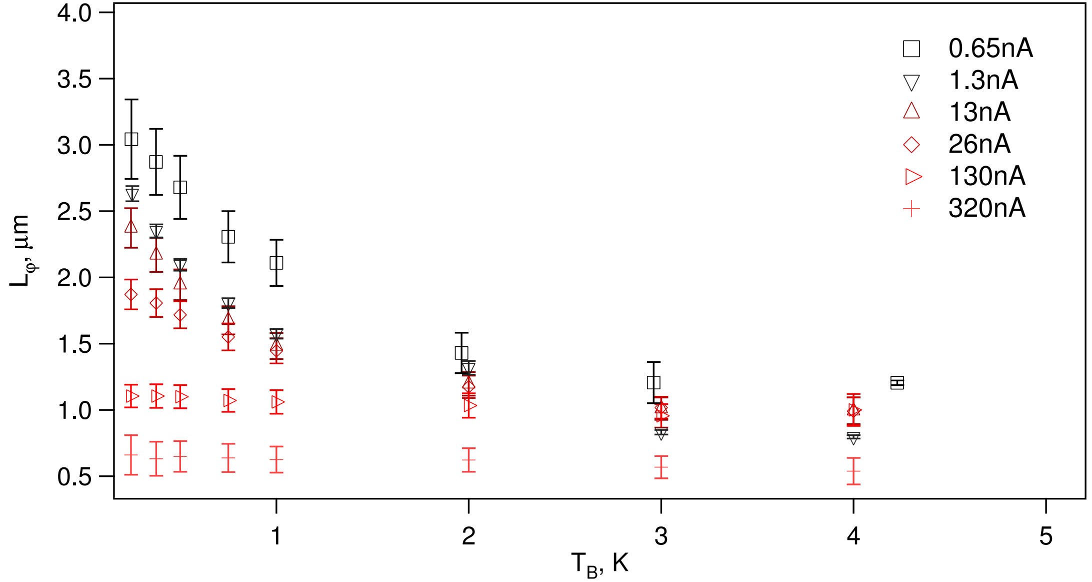

Figure 4.4: Extracted values of L_ϕ,L_i and $L_\star$ for the bath temperature dependence.

assuming an average resistance as the mean of the change in resistance between -40mT and 40mT in the 0.25K and 0.65nA case the electron temperature is calculated. Although the electron temperature is dominated by the electron diffusion contribution ($> 98\%$) both substrate and acoustic phonons are included. Figure 4.5 shows the dephasing length as a function of the calculated electron temperature for a purely overheated electron effect: the points should collapse onto a single curve defined by the lowest current. In this data set the points mostly collapse onto the curve suggesting the effect is mainly due to overheated electrons as expected. There are two main discrepancies: the large shift between 0.65nA and 1.3nA discussed before and a slight reduction in the dephasing length at large currents best shown in the 320nA curve. When compared with the length scale associated with the electric field (dashed line) L_E suggests this may be a limiting length scale in the system although the dashed lines associated with the lower currents suggest that L_E does not act to suppress the dephasing length at lower currents.

4.5 Conclusions and Future Work

Clearly a larger set of measurements are required in order to clarify any direct effect of the electric field on the weak localisation. The first obvious extension would be to increase the temperature range to include the transition to weak anti localisation as this would allow much greater currents to be applied although the

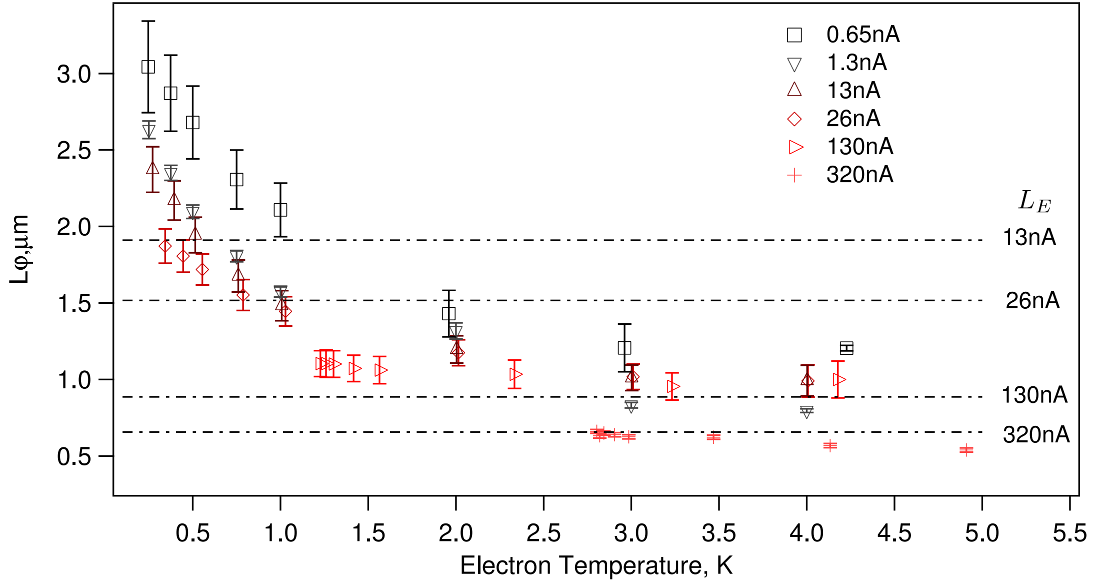

Figure 4.5: Dephasing length against calculated electron temperature. Increasing current is denoted by a change in colour from black to red. Dotted lines show the value of L_E for the different currents. A small reduction in the dephasing length is seen for larger currents.

extraction of the dephasing length would be difficult in the transition where no modulation of the conductivity with magnetic field is seen. At the current stage of development the evidence for the existence of L_E as a valid length is lacking despite the tantalising hint in the temperature normalised dephasing data. This is not an unexpected result as there have been many theoretical studies predicting a lack of an electric field effect [52, 53] due to time reversal considerations. An electric field effect was seen experimentally but assigned to overheating, directly in [59] and indirectly through modification of drift velocity in [54, 60]. Experimentally no effect was seen in thin gold films immersed in liquid helium [55]. The heating could be quantified at the lowest temperature by analysing the period of the UCF fluctuations from which a temperature could be extracted [61] as a dephasing effect any suppression of the dephasing length would also be seen in the UCF independently of the weak localisation effect. The downside to the UCF is a reduction in the magnitude of the effect with rising temperature [61] and requirement small samples $L \lesssim L_\phi$. Work has also begun on looking at the effect of a large electric field on the other quantum effect present in the temperature dependence of the resistivity the electron-electron interaction [53] which can isolated by suppressing the weak localisation with a magnetic field. Some indications of an electric field effect in the electron-electron interaction was seen in bismuth [62].

Chapter 5

Hot Phonon Decay in Graphene

In this chapter the phonon dynamics of graphene are probed in a regime much higher up the temperature scale from chapter 3. By using ultrafast laser excitation large amounts of energy are deposited into the electron bath. Using differential absorption techniques with ultrafast pulses the dynamics of phonon decay on very short time-scales is probed. By fitting the data with a coupled rate equation describing the temperature of both the electronic and optical phonon systems, anharmonic decay times of the graphene optical phonons are extracted. Measurements are taken on flakes with different numbers of layers, in both supported and suspended samples. From the extracted optical phonon decay time the nature of the optical modes involved can be examined.

There have been a number of previous pump probe studies showing the nature of excited carriers in graphene systems this interest has ranged from exfoliated flakes [63–66] to silicon carbide [67] and reduced graphene oxide [68]. Furthermore it has previously been shown in the literature that the cooling dynamics for photo excited carriers go through a number of different cooling regimes. It was theoretically shown in [69] then experimentally confirmed in [65] that the photo excited electrons thermalise through electron-electron scattering events in the tens of femtoseconds. On longer timescales a cooling bottleneck was seen in [70] to occur with a decay time of 2.5ps attributed to optical phonons in the graphene sheet. It is also reported that substrate phonons have no effect. Single layers are not measured in [70] and any substrate phonon effect could be screened in thicker flakes. In contrast coupling to substrate phonons were suggested as a mechanism in [71] which showed enhanced

cooling in transfered CVD graphene and epitaxial graphene.

5.1 Measurements of the Differential Reflection

Measurements of the electron temperature were performed by Peter Hale using near infra-red differential absorption pump probe techniques. The samples were exfolliated flakes on both silicon oxide substrates and suspended over etched holes. This allows the effect of any remote interfacial phonons from the silicon substrate to be removed. The thickness of the flakes was mainly determined by contrast measurements. For single and double layer flakes Raman spectroscopy was used to confirm the thickness. The pump pulse was generated at 830nm with a pulse width of $\approx$ 180fs this was used to optically excite the electrons within the graphene. A second probe pulse delayed in time by a variable path length with respect to the pulse was generated within a Optical Parametric Oscillator giving wavelength control from 1100-1400nm. In order for the probe pulses to have no significant excitation the intensity ratio was kept >10:1. As the flakes of graphene are on the scale of a few microns the beam spot size is set at 1.5μm by a water immersion lens (requiring the samples to be fabricated on transparent substrates) and can be rastered over the flake area by oscillating mirrors with a 250μm field of view. Figure 5.1 shows a typical dependence of the differential absorption as a function of probe delay for a 10 layer sample. There are two exponentially decaying curves with different characteristic timescales. Previously these two timescales have been attributed to electron-electron and electron-phonon interactions [67]. Initially a very fast decay happens within the first few hundred femtoseconds, which is of the same order as the excitation pulse and therefore the dynamics cannot be clearly separated out. The second timescale on the order of picoseconds is clearly resolved and has been attributed to cooling of hot phonons [67] .The temperature of the electron bath T_e can change the time dependant reflectivity by

$$\delta R(t) \propto \tanh\left(\frac{E_{\mathrm{pr}}}{4k_B T_0}\right) - \tanh\left(\frac{E_{\mathrm{pr}}}{4k_B T_{\mathrm{el}(t)}}\right) \; . \tag{5.1}$$

The effect of changing the probe energy E_{pr} can be seen in figure 5.1 this is a result of probing a different part of the tail of the electron distribution.

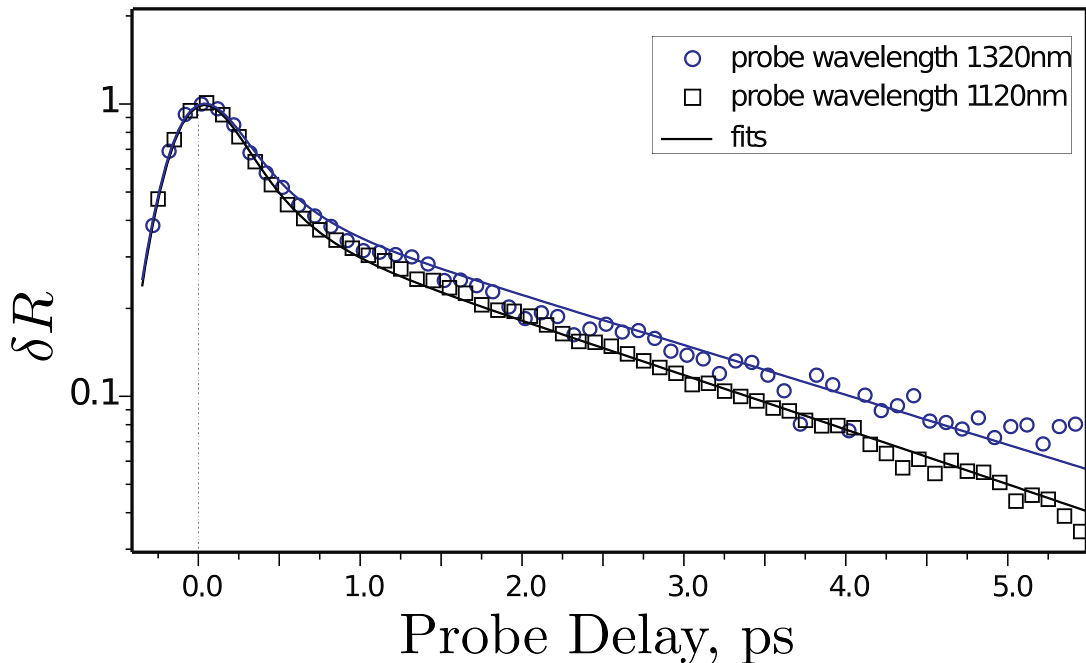

Figure 5.1: Figure showing the wavelength dependence of the differential absorption. Figure taken from [72]

5.2 Two Temperature Model

In the literature it has been suggested that the thermalisation of the excited electrons occurs within $\approx$ 10fs [65, 66]. This is well below the pulse length and therefore the assumption is made that during excitation there is always a thermalised electron system with a characteristic temperature T_e. Therefore the first timescale can be attributed to the thermalisation of the electrons with the optical phonons T_{op}. The timescales reported in the literature are of the order of $\approx$ 100fs. In order to describe the results show in the previous section a two temperature model describing an electron temperature and an optical phonon temperature based on the work in references [73] and [74].

The two temperatures can be described by a two coupled differential equations

$$\frac{dT_{\text{el}}}{dt} = -2\frac{\Gamma_{\text{ph}}\hbar\omega}{C_{\text{el}}} \,, \tag{5.2}$$

where C_{el} is the electronic heat capacity and Γ_{ph} is the phonon generation rate. The factor 2 is due to creation of phonons at the Γ and K points these technically could be described by two separate rates taking into account the small difference in phonon frequencies. For simplicity in this model a single phonon generation rate and

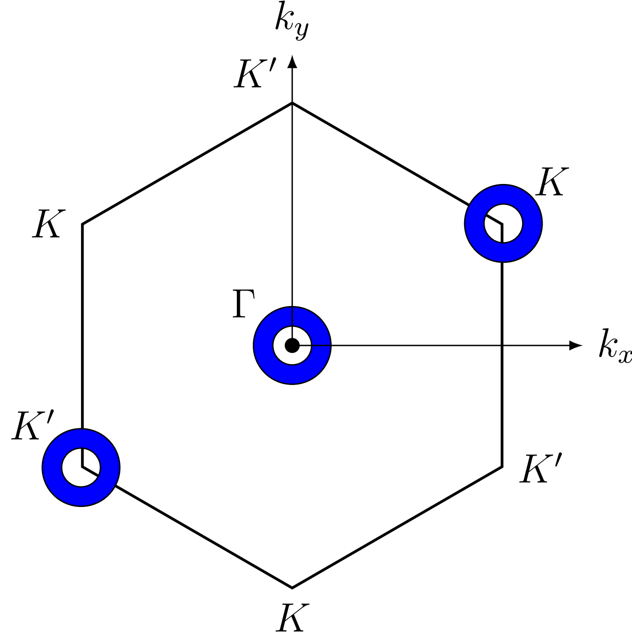

Figure 5.2: Graphene Brillioun zone showing the three inequivalent points Γ,K,K'. The blue annuli around the three inequivalent points show the area allowed for phonon scattering encompassed by M_{ph} (not to scale). The outer bound of the annuli is given by the maximum energy of electrons within the system. The lower bound is given by the maximum momentum lost by a phonon of energy $\hbar\omega_{\text{ph}}$.

frequency are taken. Secondly, the change of optical phonon population is governed by the equation

$$\frac{dn_{\text{ph}}}{dt} = \frac{\Gamma_{\text{ph}}}{M_{\text{ph}}} - \frac{n_{\text{ph}} - n_{\text{ph}}^0}{\tau_{\text{ph}}} , \tag{5.3}$$

where n_{ph}^0 is the phonon occupation at room temperature and τ_{ph} is the phonon decay rate. M_{ph} is the number of phonons per unit area that can couple to the hot electrons [74]

$$M_{\text{ph}} = \frac{2}{4\pi}\left[\left(\frac{\sqrt{2}E_{\text{max}}}{\hbar v_F}\right)^2 - \left(\frac{\omega_{\text{ph}}}{v_F}\right)^2\right] , \tag{5.4}$$

where E_{max} is the maximum energy of an electron in the system and the factor of $\sqrt{2}$ comes from the suppression of backscattering due to the chiral nature of the electrons. The are two separate definitions of M_{ph} for the K and Γ point phonons fortunately for simplicity they are equivalent $M_{\text{ph}} = M_K = M_\Gamma$. At the Γ point the factor of two comes from the two degenerate LO and TO modes whereas in M_K factor of two comes from the K and K' valleys.

To complete the picture the phonon generation rate can be defined by first writing

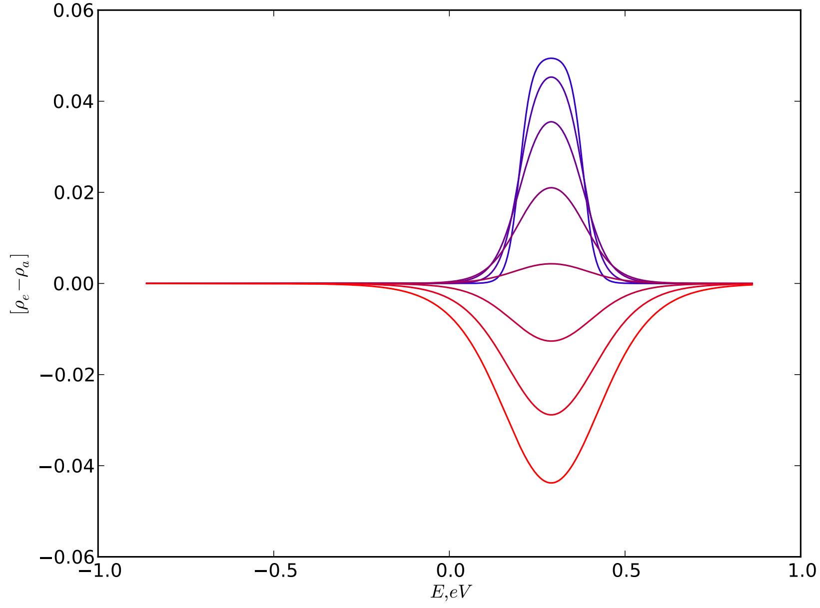

Figure 5.3: Probability of scattering $[\rho_e - \rho_a]$ as a function of energy for E_f = 0.2eV,$n_{\mathrm{ph}} = 0.05$ and temperature from 200K to 1000K (blue to red)

the probability of phonon emission at an energy E in terms of the Fermi function $f(E, T_{\mathrm{el}})$

$$\rho_e = f(E)(1 - f(E - \hbar\omega_{\mathrm{ph}}))(n_{\mathrm{ph}} + 1) \;, \tag{5.5}$$

which captures an electron transition from $E \to E - \hbar\omega_{\mathrm{ph}}$ and the creation of a phonon. Similarly for phonon absorbtion using

$$\rho_a = f(E - \hbar\omega_{\mathrm{ph}})(1 - f(E))n_{\mathrm{ph}} \;. \tag{5.6}$$

The dependence of overall scattering rate on temperature is shown in figure 5.3 in which the window around the Fermi energy in which there are both free states and electrons is clearly seen. Introducing of the electron-phonon coupling strength α and by integration over all energy states the phonon generation rate is given

$$\Gamma_{\mathrm{ph}} = \alpha \int_{-\infty}^{\infty} E(E - \hbar\omega_{\mathrm{ph}}) \times [\rho_e - \rho_a] \, dE \;, \tag{5.7}$$

in which α is given by

$$\alpha = \frac{9\left(\frac{dB}{dt}\right)^2}{2\pi\rho\omega_{\mathrm{ph}}\hbar^4 v_F^4}; , \tag{5.8}$$

where ρ is the density of graphene ($\approx 7.6 \times 10^{-7}$kg/m^2) and $\frac{dB}{dt}$ is the deformation

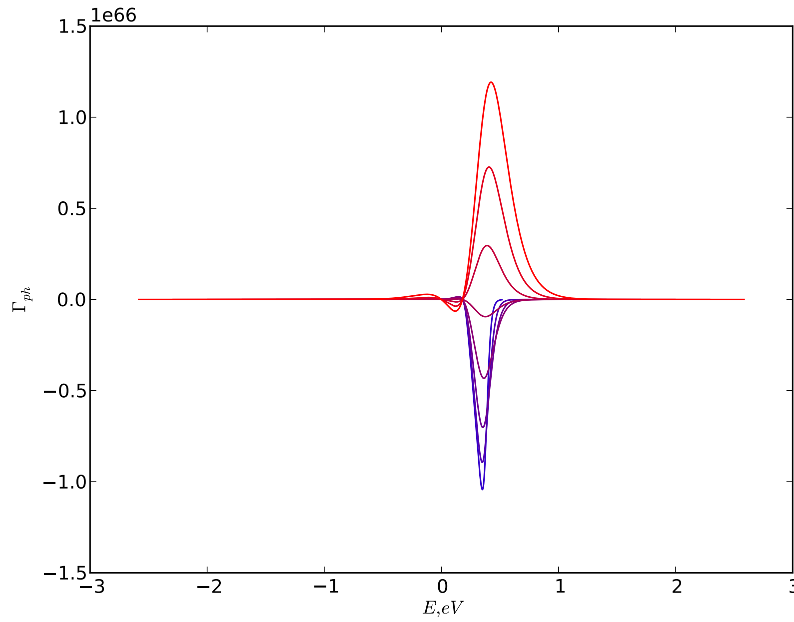

Figure 5.4: The value of the integrand in Γ as a function of energy $E_f = 0.2$eV,$n_{\rm ph} = 0.05$ and temperature from 200K to 1000K (blue to red)

potential (45 eV/nm [73]).

5.2.1 Excitation Pulse

The energy input to the electrons is included within the model by adding to eqn 5.2 an additional irradience term

$$I(t) = \frac{F}{2\tau_{\rm ex}} \frac{1}{\cosh^2(t/\tau_{\rm ex})} \ , \tag{5.9}$$

where F is the total fluence of a pulse and $\tau_{\rm ex}$ is the full width half maximum of the excitation pulse typically 100fs. This term is dominates the rise time of the electron temperature in figure 5.5

$$\frac{dT_{\rm el}}{dt} = -2\frac{\Gamma_{\rm ph}\hbar\omega + I(t)}{C_{\rm el}} \ . \tag{5.10}$$

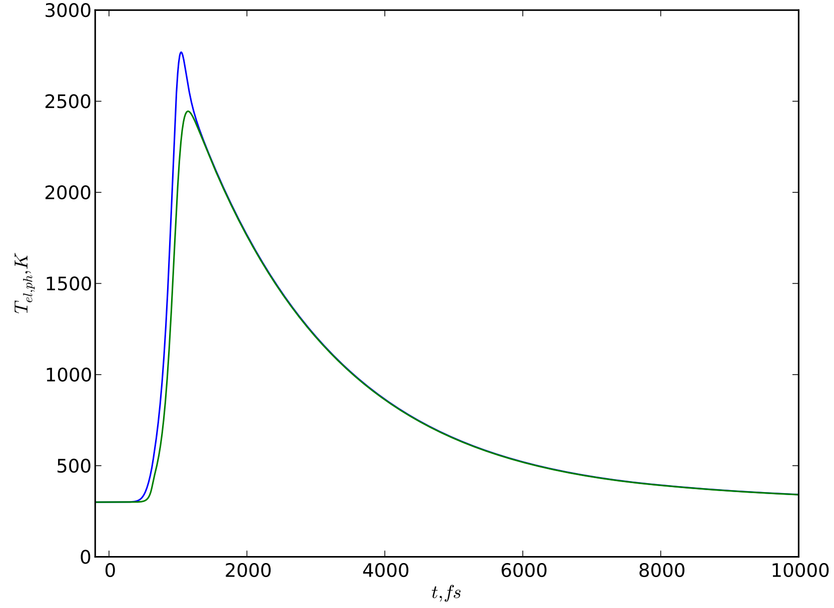

Figure 5.5: The electron (blue) and phonon(green) temperatures as a function of time t from excitation pulse (centred around $t = 0$) calculated for a τ_{ph} of 2ps and a fluence $F = 0.128 \times 10^{15}$.

5.2.2 Computation of the Model

To compute the time varing solution of the simultaneous eqns 5.10 and 5.3 Euler's method is used in which the the differential can be written

$$\frac{dT}{dt} \approx \frac{T(T_0 + \Delta T) - T(t_0)}{\Delta t} \tag{5.11}$$

as long as Δt is small compared with changes in the function. Typically 2200 points are used to calculate the curve in Figure 5.5. At this point it is convenient to plot the temperature of the phonon modes rather than the occupation number using the Bose-Einstein distribution function

$$n_{\text{ph}} = \frac{1}{e^{E_{\text{ph}}/k_B T_{\text{ph}}} - 1} \,. \tag{5.12}$$

Each step in the calculation recalculates the important quantities of Γ_{ph} and C_{el} using the value of $T_{\text{el}}(t - \Delta t)$. Figure 5.5 shows the evolution of the system from a initial overheated electron state $T_{\text{el}} > T_{\text{ph}}$ transitioning to $T_{\text{el}} = T_{\text{ph}}$ through fast optical phonon generation. The decay of the second timescale is therefore dominated by the loss of energy from the optical phonons presumably through anharmonic

decay into acoustic phonon modes.

5.2.3 Fitting the Data

Any comparison of the calculated temperature values with the differential reflectivity must include broadening associated with the probe pulse. The rise time of the temperature is already accounted for by the rise time included in $I(t)$. Therefore the resultant temperature profile is convoluted with a probe pulse of the same form as equation 5.9 with a FWHM of 100fs to give the expected response. Taking the convolution of $T_{\mathrm{el}}(t)$ converted to reflectivity via eqn 5.1 the data is compared with experiment. All the values required for the calculation are known apart from τ_{ph} and the absorbed fluence which can be estimated using a laser power meter to get the power of the beam. The exact value of the fluence is dependent on the exact size of the spot which can vary with focusing and losses inside the confocal microscope which can vary dependant on alignment. Therefore the fluence is taken as an adjustable parameter and is observed to converge on a sensible value.

A least squares fit of the calculated $\delta R(t)$ performed to minimise the chi-squared value

$$\sum_t \left(\frac{\delta R(t) - \delta R_{\mathrm{exp}}(t)}{\sigma_t} \right)^2 \tag{5.13}$$

where σ_t is the standard deviation of the experimental points.

A exponential fit to the experimental data in Figure 5.1 gives values of $\tau_{\mathrm{exp}} = 3.35 \pm 0.1$ps and $\tau_{\mathrm{exp}} = 3.6 \pm 0.05$ps for probe wavelengths of 0.94eV and 1.11eV respectably. Using the full model produces similar values for the phonon decay times .

5.3 Layer Dependence of the Phonon Decay Time.

Measurements of the differential reflectivity are performed in samples with varying numbers of layers. The phonon decay time is extracted for each of these measurements which are taken on a number of different flakes and in different areas of those flakes. A set of example decays and the extracted values for all flakes measured are shown in figure 5.6. τ_{ph} can clearly be seen to saturate above four layers despite the large scatter in the data. Averaging of the measurements for each layer gives

a characteristic relaxation time for the monolayer* of 2.05ps ± 0.42ps increasing to 3.30ps ± 0.28ps at 6 layers where it reaches an asymptote. This saturation suggests above four layers the decay dynamics are behaving the same as bulk graphite. The reduction in phonon decay times at low layer numbers suggests an additional loss mechanism which is suppressed at large number of layers. There are two possibilities for this additional loss mechanism. Firstly, coupling with interfacial phonon modes in the substrate which are not available to layers higher in the stack due to the greater distance and screening of substrate electric fields by the graphene electrons. Second is through additional coupling to out of plane phonon modes which are suppressed by the increasing stiffness of the thicker graphene sheets. Although the presence of a substrate could suppress out of plane phonon modes, the roughness of the glass substrate can allow these modes, due to the roughness being on the order of the phonon wavelength. There can also be decoupling of the substrate due to ripples and bubbles as seen in the AFM image in figure 5.7. The scatter in the data in figure illustrates a problem with measurements of graphene in general, as an exposed thin sheet being measured in ambient conditions it is susceptible to gas adsorbtion [75] and stress and strain applied during fabrication.

5.3.1 Layer Dependence of the Phonon Decay Time in Suspended samples.

In the previous section two possible mechanisms were suggested to explain the layer dependence of the relaxation rate. The role of the substrate can easily be isolated by suspension of the graphene flakes over 3.5μm holes in a glass cover slip. The fabrication method consisted of creation of a large array of holes by oxygen plasma etching to a depth of 300nm confirmed by AFM. Exfoliation was then performed onto the pre-patterned substrate. Figure 5.7a shows a AFM image of a flake suspended over the hole measurements can be taken purely on suspended regions due to a spot size of >1.5μm. To be convinced that 300nm is a large enough distance for the flake to be truly suspended the interaction distance of the substrate phonon's in graphene should be considered. The maximum wavelength of of an interfacial

*These decay times are compare well with extracted from anti-stokes raman measurements on carbon nanotubes which reported values of 1.1ps for the decay of hot optical phonons.

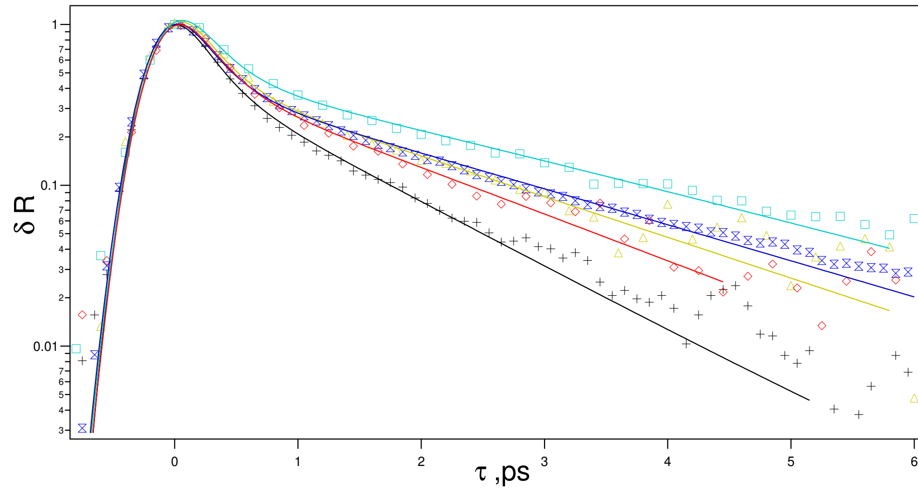

(a) Normalised differential reflectivity as a function of probe delay for different layer samples. The fits are generated by the two temperature model with fluence and τ_{ph} as free parameters. The different layer numbers are 1,2,3,4 and 6 denoted by black,red,green,purple and blue respectively.

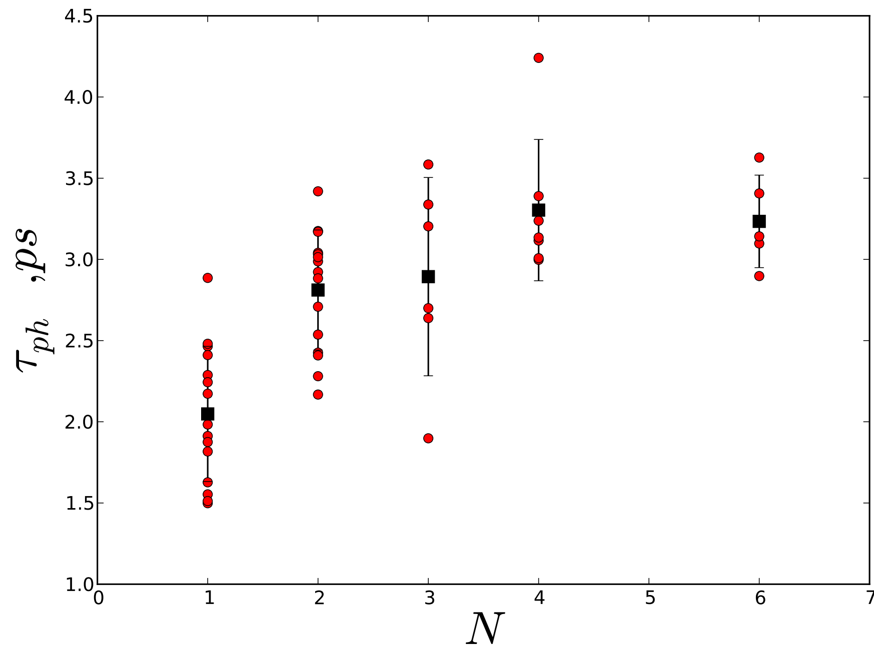

(b) Extracted phonon lifetime as a function of layer number. Note the large spread associated with the different samples measured the average for each layer is show by the black squares and the error bars are the standard deviation.

Figure 5.6: Supported Graphene

phonon of energy f_s is equal to

$$\lambda_s = \frac{2\pi v_F}{f_s} \ , \tag{5.14}$$

where f_s is the optical phonon frequency.Therefore taking the optical phonon energy to be that of the interfacial silicon oxide mode (59meV) the interaction distance can be shown to decay on lengths <100nm. Figure 5.7b shows the layer dependence for the suspended layers which are clearly similar to the supported layer dependence. The comparison between the two suggests strongly that the substrate does not play a role in the relaxation rate. There may even be a faster relaxation time in the monolayer flake all the points measured sit below the standard deviation of the supported times. This would support the hypothesis that the out of plane phonon modes contribute to the additional relaxation in the thinner flakes as they cannot be suppressed by the presence of a substrate whilst suspended.

5.4 Conclusions

In conclusion by near infrared measurements of the differential reflectivity using a pump probe configuration the ultrafast carrier dynamics in graphene can be measured. Two distinct timescales are seen of which the longer ps timescale has been associated with phonon relaxation. A model has been developed to extract the phonon relaxation time in a multitude of different flakes. A timescale of phonon relaxation is shown to depend on layer with the fastest relaxation occurring within monolayer graphene. This fast relaxation pathway is attributed to out of plane phonon modes through measurements of suspended and supported flakes.

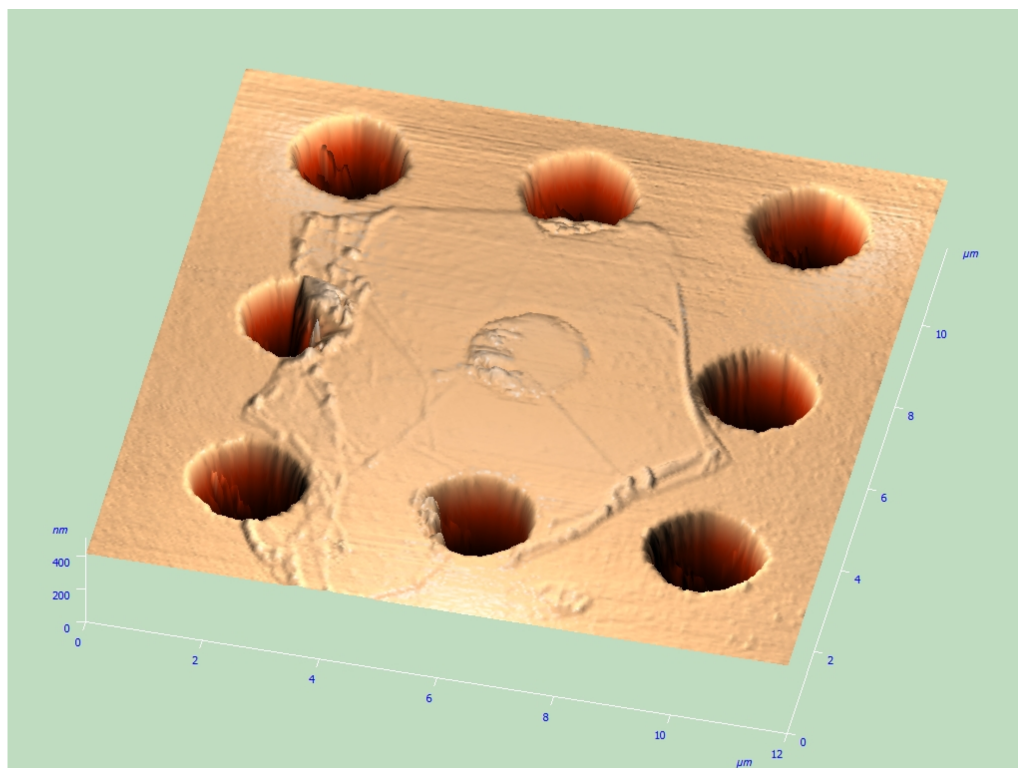

(a) AFM height map of the graphene flake and substrate clearly showing the graphene suspended above the etched holes.

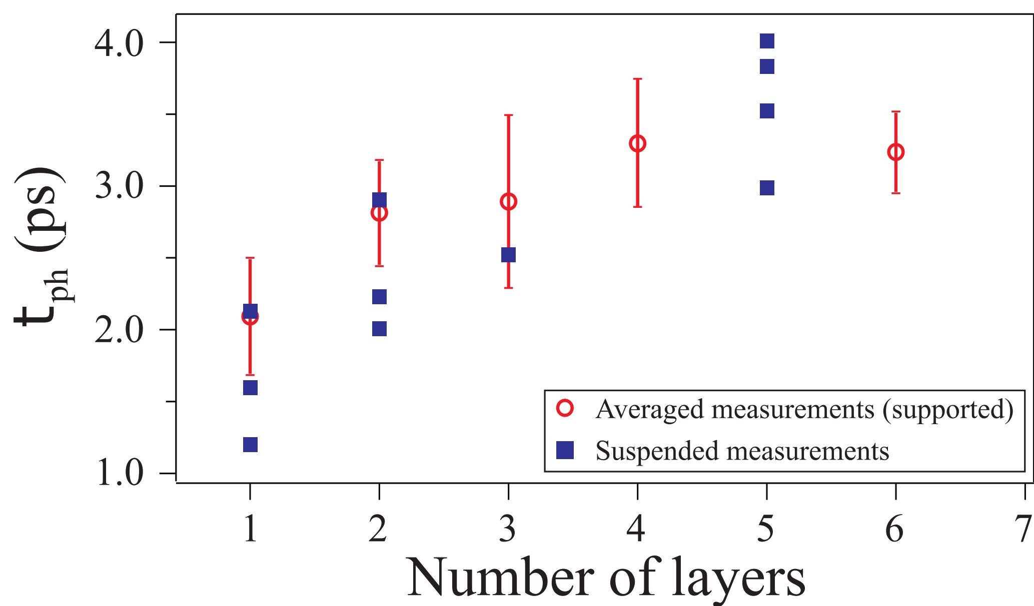

(b) Comparison of the average supported and suspended τ_{ph} as a function of layer number.

Figure 5.7: Suspended Graphene

Chapter 6

Desorption of Oxygen from Graphene by Femtosecond Laser Pulses

Ultrafast laser measurements on graphene have given insight into relaxation mechanisms and timescales in this material as seen in chapter 5. After ultrafast photoexcitation of the electrons in graphene, energy relaxation occurs through mechanisms with markedly different timescales: first through energy redistribution from electron-electron scattering (∼30fs [76]), then by thermalisation with optical phonons (∼100fs). Energy is lost from the electron-phonon bath through annharmonic decay of optical phonons and/or coupling to substrate phonons (∼1ps) [72,74]. This picture has subsequently been corroborated by theoretical models [77]. More recently, ultrafast spectroscopies have been used to probe the timescales of charge transfer to graphene from photoexcited absorbed molecules [78, 79]. However, relatively little is known about the timescales associated with molecular processes, such as absorption and desorption of absorbed molecular species [80], or of reactions taking place at the interface [81]. Molecular species absorbed at graphene interfaces can have a huge influence on the properties of the graphene film. Graphene, being essentially a two dimensional conductive surface with no bulk component, can display incredible sensitivity to the environment to which it is exposed. These simple properties have led to single molecule sensitivity [24], an understanding of the molecular orientation of absorbed species [82] and a large number of sensor

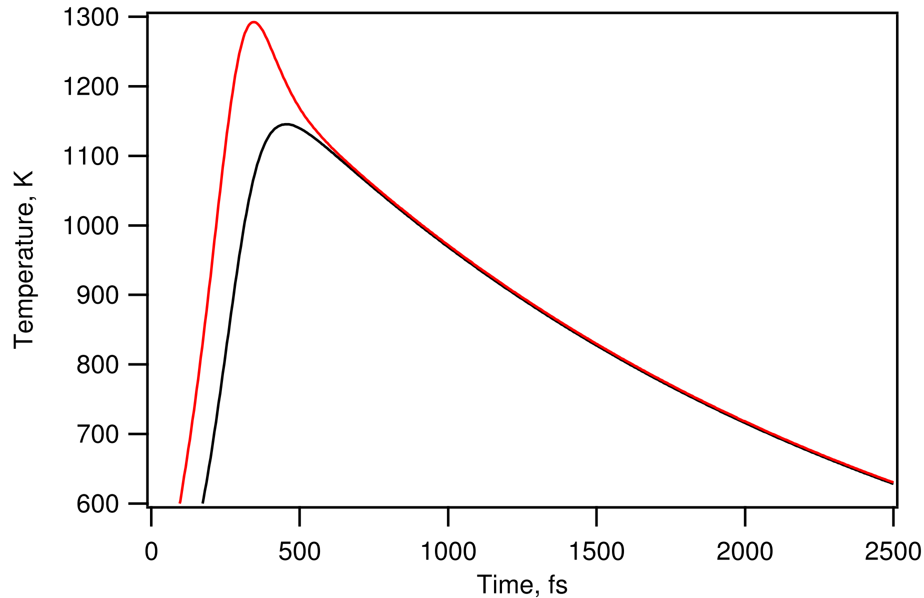

Figure 6.1: Time dependence of the electron (red) and optical phonon (black) temperatures due to an absorbed fluence of 0.1 J/m^2 calculated using the two temperature model from chapter 5.

applications [21–23, 83, 84]. Absorbed gases have also been shown to affect a number of fundamental investigations such as the THz conductivity of graphene [75]. Oxygen adsorbates in particular are known to perturb the electronic structure of graphene [85], by fractional charge transfer from the graphene sheet to the oxygen molecule (thereby reducing the graphene carrier density). Recent studies have shown the importance of the substrate and conditions on this charge transfer [86, 87].

In this chapter, two-pulse ultrafast correlation spectroscopy is applied to investigate the mechanisms, energies and timescales relevant for the molecular absorption of oxygen molecules on graphene flakes. This is the first time this technique has been applied to study chemical processes on a graphene interface. It will be shown that by monitoring the conductivity of graphene, (as a probe of charge transfer to the molecules on the graphene surface) and varying the time delay between correlated pulses, one can gain insight into the timescales relevant for the processes involved. For photo-desorption of oxygen molecules, a non thermal mechanism is suggested as the dominant desorption pathway, as the process exhibits a relaxation timescale that is much faster than the timescale for the decay of hot optical phonons.

The advantage of using femtosecond pulses for optical illumination is the large instantaneous power combined with control of the timescale over which energy transfer occurs. As seen in the previous chapter there are two important timescales to

consider: these are shown again in figure 6.1 for an absorbed fluence of 0.1 Jm^{-2} per pulse and a τ_{ph} of 2ps from which an electron temperature of >1000K is achieved. The cooling of the carriers in the first 100fs is limited by the rate of cooling to optical phonons until thermal equilibrium between electrons and optical phonons is achieved. The rate is then limited by phonon decay on a timescale τ_{ph}. On longer (∼100ps) timescales , diffusion of lattice heat through the graphene and substrate leads to equilibration with surroundings [88]. There is therefore a clear distinction in the timescales expected to be relevant for optically stimulated chemical processes on graphene interfaces: <100fs for processes mediated by hot electrons, ∼1ps for hot optical phonons, and ∼100ps for thermal lattice heating.

6.1 Experimental Method

To investigate the relevant timescales, graphene flakes were mechanically exfoliated onto conductive silicon substrates covered by a 300nm-thick SiO_2 layer, allowing Fermi level control by application of a gate voltage between flake and substrate. Flakes were identified as single layers by optical contrast measurements and Raman spectroscopy. Electrical contacts were made with Cr/Au(5/50nm) to allow four-probe measurement of the differential resistance. This resistance, dV/dI , was measured at room temperature by a low-frequency (∼3kHz) lock-in technique at 6μA. Oxygen exposure has been shown in previous measurements [89] to affect contacts to carbon nanotubes. Therefore a four point probe resistance measurement technique was used to avoid contact resistance. By an AC modulation(3Hz) of the gate voltage the position of minimum conductivity (Dirac point) as a function of applied gate voltage can be tracked giving a real time measurement of the level of doping in our sample (shown in figure 6.2b).

In figure 6.2 the effect of adding oxygen (99.5% purity) at 1atm to the vacuum chamber (previously pumped to $\sim 10^{-6}$ mbar) for multiple doping events is shown. There is a fractional charge transfer to the oxygen from the graphene evidenced by a shift of the Dirac point to greater positive voltages. This shift eventually saturates to a value which is repeatable on multiple redoping steps after oxygen removal. A shift in the saturation voltage is observed after an exposure to atmosphere and this is attributed to increased doping due to water, as described in [87]. This is

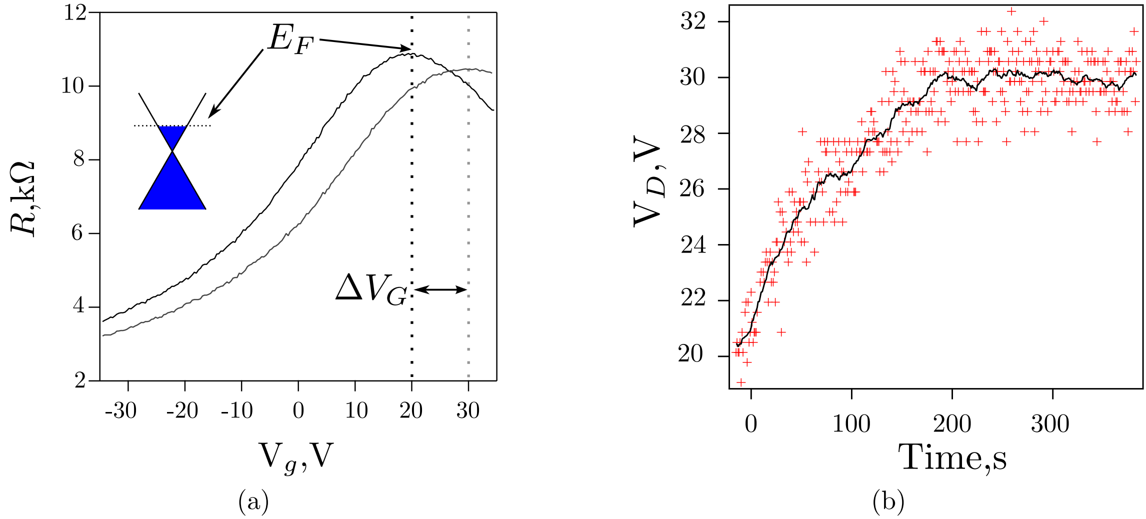

Figure 6.2: (a) Resistance versus voltage curve (RVg) as a function before and after exposure to 1atm of oxygen(black and grey respectively). The positions of the extracted Dirac points are indicated by the dotted lines. The change in Dirac point position is given by ΔV_g. (b) Shows the extracted Dirac point position as a function of time after oxygen exposure at time=0. The scatter in the points is caused by the extraction process the black line shows a 20 point moving average giving a better comparison with the averaging used later.

in contrast with the exposure of dry-N2 gas which shows no such doping effect. During the oxygen doping process the gate is constantly swept to track the gate position. The Dirac point position is extracted via two methods. The simplest is by taking the maximum value of the resistance and calculating the corresponding gate voltage value: this leads to the large amount of scatter seen in figure 6.2b caused by the broadening of the peak. Better precision can be achieved by fitting linear slopes to the conductivity in the electron and hole regions in the linear part of the conductivity away from the Dirac point. The disadvantage to the fitting method is artefacts caused by the Dirac point approaching the edge of the measurement window defined by the maximum gate voltage that can be applied to the sample without risking damage. The number of oxygen molecules on the surface can be calculated from the Dirac point shift, taking into account the capacitance of the gate to give the electron concentration change

$$n = \frac{\epsilon_0 \epsilon_{sio2} \Delta V_g}{te} , \tag{6.1}$$

where t is the thickness of the gate and V_g the voltage across the silicon dioxide gate. Each oxygen molecule transfers a charge to the flake approximately 0.01-0.02e

based on DFT calculations [90], though this is strongly dependent on the nature of the calculation, and the transferred charge will also depend on the density of states in the graphene [82]. Making the assumption that at full coverage there is a single oxygen molecule per hexagonal cell of area $(3\sqrt{3}/2)a^2 = 5.24 \times 10^{-20}\text{m}^2$ where the intercarbon distance $a = 1.42$ Å, a carrier concentration shift of 7×10^{15} m^{-2} can be calculated from a maximum gate voltage shift observed of Vg$\sim$10V assuming a transferred electron charge of 0.02e, an approximate coverage per unit cell of two percent is estimated. This suggests a weak bonding mechanism such as chemisorbtion. (Physisorption can be discounted as a bonding mechanism at room temperature due to the low binding energy [82]).

6.2 Laser Desorption of Oxygen

Once the gaseous absorption onto the graphene surface has saturated, the chamber is pumped down to a pressure of $\sim10^{-6}$ mbar. The sample is then exposed to ultrafast laser irradiation using a Coherent Legend amplified lasers system (800 nm; 1 kHz repetition rate; pulse fluences from 1.7 Jm^{-2} to 9.5 Jm^{-2}, varied using a neutral density filter). The spot size is considerably bigger than the graphene flakes, $\sim$ 4 mm and 10 μm, respectively. Assuming that $\sim$2.3% of the incident fluence is absorbed by the graphene flake, this corresponds to a range of absorbed energy densities of 0.04 Jm^{-2} to 0.22 Jm^{-2}.

Under ultrafast laser excitation a reversal of the Dirac point shift is observed, attributed to the photo desorption of the oxygen from the graphene surface. This behaviour can be clearly seen in Fig. 6.3, which shows the minimum conductance point shifting back towards zero gate voltage. A number of measurements have been carried out using four terminal devices which show similar behaviour, indicating that the photoexcited changes are due to flake conductance and not to changes in electrode contact resistance. By using the Fermi level position of the graphene flake as a sensor only molecules directly interacting with the graphene electronic structure are observed. This allows the measurement to be performed in high vacuum rather than the ultra-high vacuum needed for mass spectrometry techniques [80]. The gate voltage is set to zero during exposure to the laser to exclude any effect on the desorption process directly though the electric field or by changing the orientation of

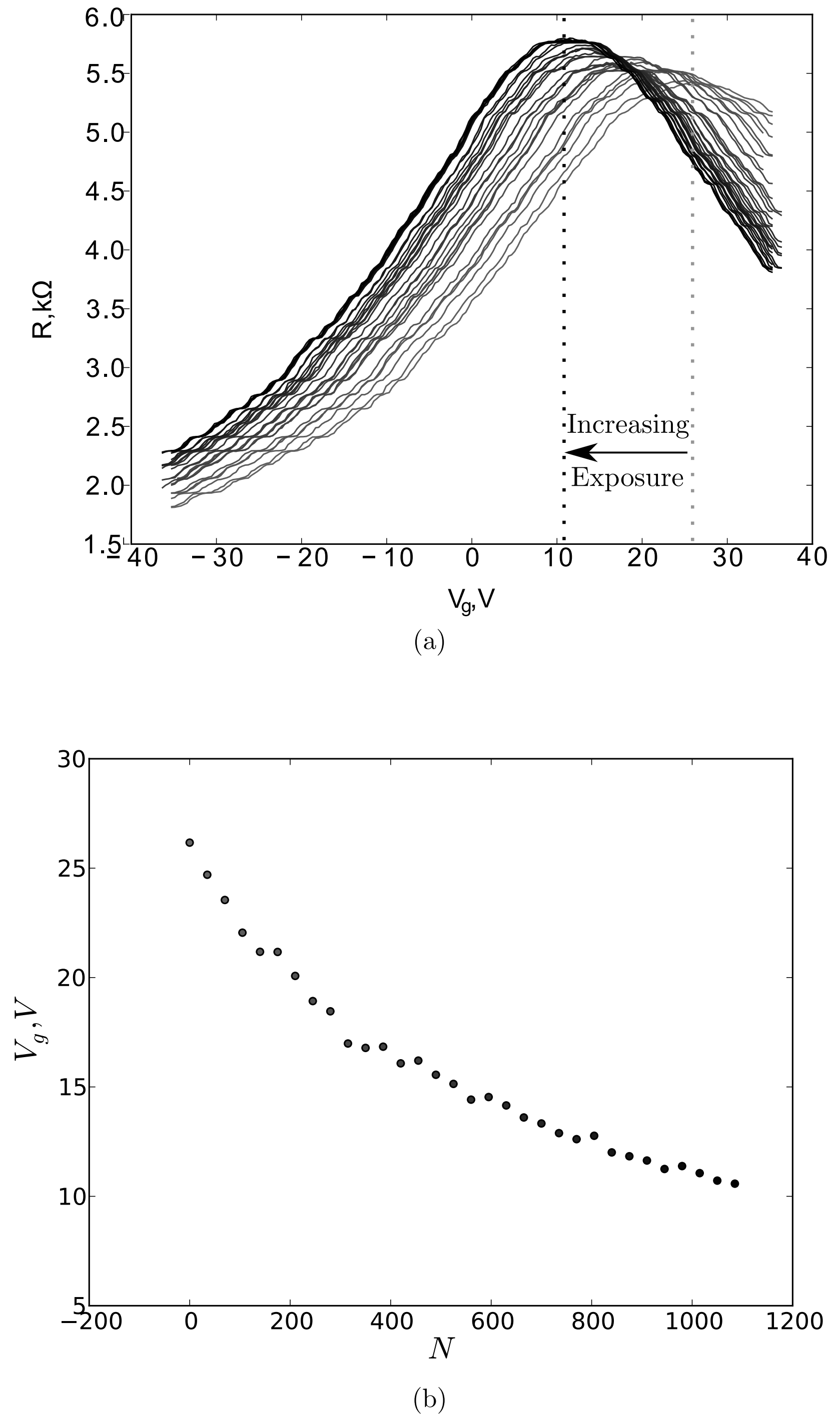

(a)

(b)

Figure 6.3: Figure showing the evolution of the doping level with increasing number of pulses N (0.11Jm^{-2}),160fs delay between pulse pairs). (A) shows the gate voltage dependence of the resistance with increasing number of pulses (from gray to black). The initial and final Dirac point positions are marked by gray and black dotted lines respectively. (B) Shows the absolute position of the Dirac point extracted from (A) by taking the maximum resistance point as a function of the number of incident pulses. The reduction in the gradient is attributed to the reduction in number of oxygen molecules absorbed.

molecules [82] and therefore, the binding energy [82]. Over extended pumping times in vacuum a negligible change of the Dirac point with time is observed, suggesting that the effect measured is solely dependent on photo-activated processes and not vacuum annealing. Indeed it was shown in [82] that elevated temperatures well above room temperature are needed to return the graphene to a pristine undoped state. Therefore, the position of the Fermi level on the plot shown in figure 6.3 can be used to track the number of absorbed oxygen molecules on the graphene interface.

Figure 6.3 shows the evolution of the Dirac point with increasing number of femtosecond pulses (In this case a pair of separated pulses are used.) Each data point consists of 60 averaged resistance versus gate voltage curves between which the sample is exposed to a train of pulses at 1kHz. Each additional pulse train (0.11Jm^{-2}) removes more oxygen from the surface, but as the coverage decreases the gradient of the slope decreases. As the number of pulses incident on the sample approaches 500, there can be observed the beginning of the saturation of the voltage change per pulse. This saturation effect leads to a gradual decrease in gate voltage change per pulse, as a function of exposure. In order to minimize this decrease in the Dirac point shift as a function of absolute gate voltage, measurements were taken in a small window of gate voltage corresponding to the linear part of the slope in figure 6.3. Furthermore, under prolonged exposure to the femotosecond radiation, permanent changes to the graphene samples are observed through a reduced desorption for a given intensity and irreversible p-doping of the graphene. A number of mechanisms may be responsible for this effect; higher binding energy of the oxygen to the graphene due to defects [90] (though there is no significant onset of a defect peak in the Raman spectrum [91]), cleaning of the graphene surface through the removal of fabrication residues or adsorbed water [87] or modification of the graphene and its conformation to the SiO_2 substrate. It is important to note that the fluences with which the graphene flake are exposed are significantly smaller than in some reported ultrafast measurements of graphene [91, 92]. The long term exposure effects observed in these sensitive experiments suggest that one should be somewhat careful when exposing graphene samples to ultrafast laser irradiation.

Figure 6.4 shows the gate voltage shift per femtosecond pulse. A strong nonlinear dependence on the intensity is shown. This non-linearity could originate from either

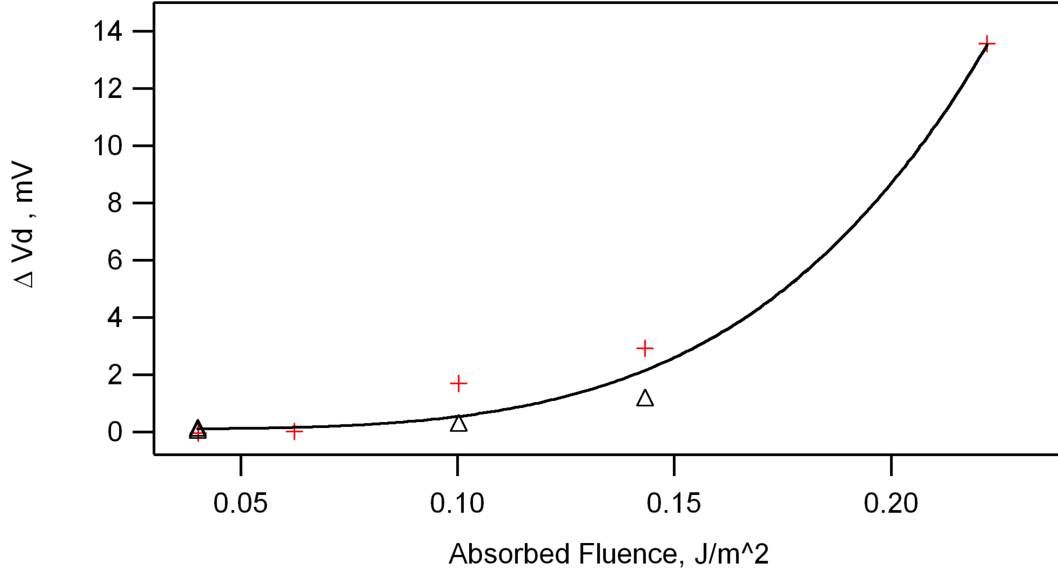

Figure 6.4: Gate voltage shift per pulse as a function of integrated power. Data points were taken with different lengths of exposure. Fit of a power law dependence (black) of the form $x^{4.2}$ (the factor can vary by a large amount between samples)

an activated energy effect [93] or a non-linear optical process requiring multiphoton excitation [93]. The points in figure 6.4 are separated into crosses and triangles which indicate the increasing and decreasing intensity sweeps respectively. The hysteresis shown is indicative of the slow degradation of the shift magnitudes with increasing exposure discussed previously. As a result, we can only surmise that the photo-desorption process exhibits a power law dependence on the fluence with orders ranging between $x^{2.2}$ and $x^{4.2}$. Moreover, from the intensity dependence alone it is difficult to conclude anything about the mechanisms and timescales involved in the process. Therefore a two pulse correlation method is used and described in the next section.

6.3 Two Pulse Correlation

The relevant timescales of the process can be investigated by using a two pulse correlation experiment. Similar two pulse correlation measurements have been used to study oxygen desorbtion from Pt111 surfaces [80]. As shown in figure 6.5, two pulses are made coincident on the graphene sample, and we record the Fermi level shift associated with excitation by both pulses. Then, by varying the time delay between the arrival of the pulses, we obtain information about the relaxation timescale of

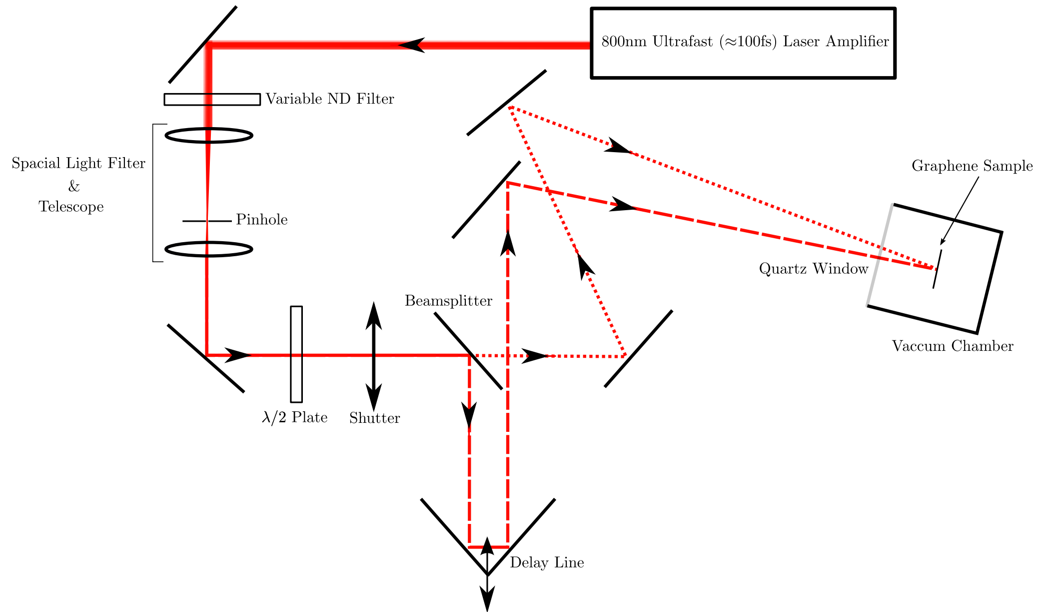

Figure 6.5: The experimental setup for the measurement of graphene under irradiation of ultrafast pulses.

the mechanism responsible for photo-desorption. Figure 6.5 shows the schematic of the setup used for laser desorption measurements. It allows two pulses of equivalent energy to be separated at the beam splitter and shifted with respect to each other in time by τ_d dependent on the difference in path length set by the delay line. The total power of the two beams are set depending on the variable neutral density filter. Fluctuations in the beam intensity across the beam create an uncertainty in the power used due to the large beam to sample ratio. Also shown in figure 6.5 is the spatial light filter used to homogenise the beam, which acts by passing the beam through a focus, and by doing so only the parts of the beam which correspond to a perfect plane wave are focused to the central point. The non-planar light forms an Airy disk around the central point, and by placing a pinhole around the focal point of the lens this light is blocked and a cleaner beam better approximating a plane wave is allowed to pass. A second lens re-collimates the expanding beam at the spot size required.

Figure 6.6 shows the change in the Dirac point position as a function of the number of laser pulse pairs used to photoexcite the sample for different delays between the two autocorrelation pulses. The signals are inherently noisy due to pulse to pulse variations in the intensity profile of the beam. These fluctuations are moderated by fitting a gradient to the linear part of the curve (see lines in figure 6.6), allowing

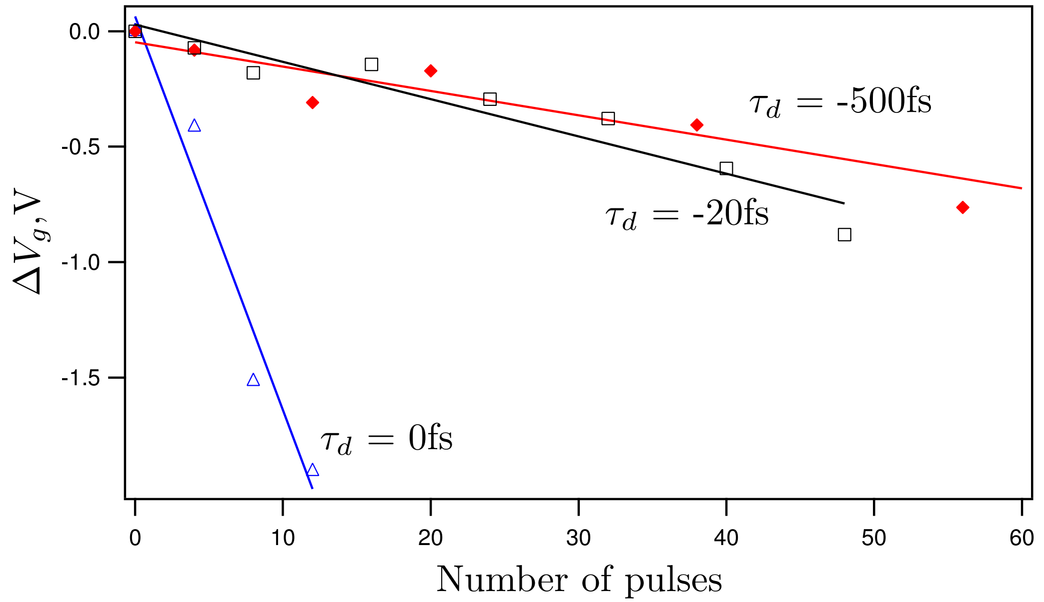

Figure 6.6: Typical change in the Dirac point position (doped position is $V_D = 10.7 \pm 0.2$V) as a function of the number of pulses incident upon the flake at varying pulse delays. Linear gradient fits are taken to the determine the strength of the effect. Combined incident power of the two pulses was 2.4Jm^{-2}

an approximate quantification of the strength of the effect for each delay time. In order to avoid the depletion saturation in figure 6.3 only small shifts are made to the Dirac point position before redoping to keep in the linear part of the curve. Figure 6.6 shows very strong dependence of the signal on the pulse delay time. The greatest change per pulse (the gradient of the signal in figure 6.6) is observed when the pulse pair are overlapped in time (at delay time of 0 fs*), and the effect per pulse diminishes very quickly as the correlated pulses are displaced in time. This effect is not due to coherent interference between the laser pulses when overlapped in time: coherent artefacts are in fact minimised by using orthogonal polarisations for the two pulses and by averaging signals over many different pulse pairs. The relevant relaxation timescale for the photo-desorption process can be estimated by comparison to the autocorrelation of the laser pulse (solid line in fig 6.7) to be less than 100fs.

There are several possible mechanisms for photo-desorption from the surface: direct photoexcitation of the oxygen molecules [94], or indirect desorption mediated through hot electrons in graphene [80], or mediated by the heating of the lattice (from electron-phonon thermalisation processes [95]). These different mechanisms

*Determined by second harmonic generation in a BBO crystal.

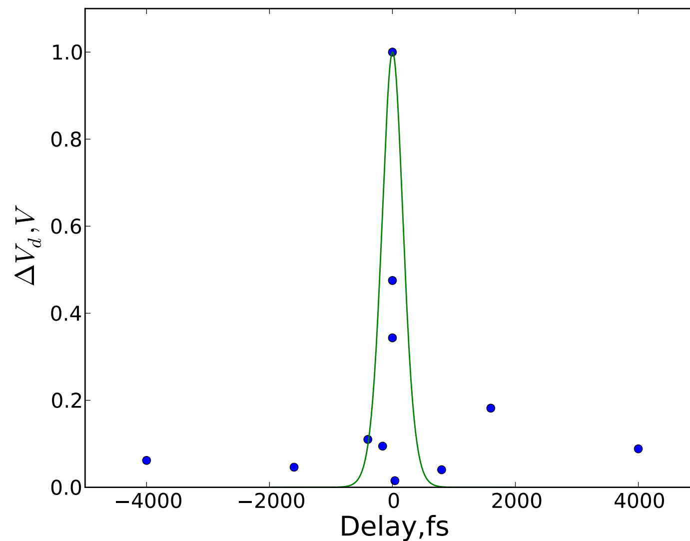

Figure 6.7: Normalised average change per pulse as a function of pump probe delay. Points are produced by a linear fit of absolute Dirac point position as a function of number of exposures.

have different characteristic timescales, ranging from the very fast decay of hot electron states in graphene (dependent on electron phonon coupling and occurring on <100 fs timescales), the slower decay of hot phonons (occurring on >1ps timescales [72]), and through to the much slower decays of molecular excitation states [78, 79]. The very fast (<100 fs) timescale relevant for the photo-desorption process studies here suggests that it is not mediated by heating of the lattice, which would exhibit significantly slower (>1ps) timescale. The direct desorption process would have the signature seen in the two pulse correlation if the process depended on multiphoton absorption. However values of the binding energy of oxygen to graphite in the literature suggests E =200meV [87]. These values suggest that the photon energy at 800nm of 1.5eV makes this a single photon process and therefore should not depend on delay between the two pulses.

The most likely mechanism therefore involves hot electronic states in the graphene. Indirect desorption can occur through non-equilibrium hot electron states generated prior to electron-electron thermalization (which occurs on a timescale of ∼30fs [76]), or indeed the hot-thermalised states formed prior to electron-phonon thermalisation (which occurs on a timescale of ∼ 100fs [74]). Currently the time resolution of the laser pulses ∼100fs , prohibits distinguishing between these two possibilities.

6.4 Conclusion

In conclusion, a new ultrafast, two-pulse correlation measurement suitable for studying molecular processes at a graphene interface has been developed. By monitoring photo-induced changes in the Fermi level of the graphene, we are able to deduce the timescales relevant for the desorption of doping oxygen molecules from the interface. The timescale associated with the photo-desorption is observed to be <100fs, indicating that heating of the lattice is not responsible for desorption. The time and energy scales involved suggest indirect excitation via hot electronic states in the graphene is the mechanism for desorption, though the relevent timescale, either before electron thermalisation or during electron optical phonon thermalisation, is currently unclear.

Chapter 7

Conclusions and Future Work

In this thesis a presentation of different mechanisms of carrier cooling at different temperatures is shown. From measurements at high temperatures such as those induced by optical excitations the dynamics of optical phonon modes can be probed. By varying the number of layers of graphene, an increase in the anharmonic decay time of optical phonon modes is seen with increasing number of layers. This suggests an additional decay route in thinner sheets of which the most likely candidate is out of plane modes in the graphene which are suppressed by the addition of extra layers. Further insight into this decay mode could be made by attempting to suppress the decay by shifting the Fermi level reducing the number of states available for scattering. Transport measurements allow similar phenomena to be examined but in a much lower energy regime. By using a measurements of the resistance with varying applied source drain bias the cooling mechanism of charge carriers at energies below the optical phonon energies has been investigated. The importance of sample construction has been shown with scattering between optical phonons in the substrate becoming an important energy loss mechanism in larger samples. Additionally it has been shown that screening due to electrons in the graphene must be considered to correctly describe the energy loss to optical phonons in the substrate.

Chapter 3 confirms an assumption made in the previous chapter that the application of an electric field does not effect the quantum corrections. The weak localisation correction to the conductivity is shown only to depend on the temperature of electrons and not on the size of the field even at energies exceeding the diffusion energy. The maximum electric field that could be applied during these

measurements was limited by the maximum temperature of the cryostat can achieve combined with the maximum temperature of the weak localisation signal. Chapter 4 a technique is outlined for tracking the Dirac point in real time and extracting the dynamics of oxygen absorbed on the graphene surface. A fast timescale for the desorption is shown using a two pulse excitation experiment. Currently the limiting factor for this experiment is reproducibility which can be attributed to differences in the fabrication process. The current exfoliation process produces samples on the order of 10μm in size by using chemical vapour deposition (CVD) on copper samples on the scale of mm can be produced. These will then cover a significant portion of the beam giving a much greater surface area for adsorbtion of the oxygen. CVD graphene will also allow the batch producing of samples all exposed to the same fabrication process, additionally resist free evaporation of contacts could reduce the contamination of the surface. Finally the mechanism of desorption can be probed using polarisation of the two incoming pulses at overlap. If the desorbtion is due to an multiphoton excitation of the graphene oxygen complex a polarisation dependence of the desorbtion intensity could be seen due to the momentum selection rules. In the other case where the hot electron population in the graphene excites the desorption electron-electron scattering in the hot electron bath will randomise the momentum.

Bibliography

[1] A. H. Castro Neto, F. Guinea, N. M. R. Peres, K. S. Novoselov, and A. K. Geim. *Reviews of Modern Physics* **81**(1), 109–162 (2007).

[2] C. Thomsen, S. Reich, and J. Maultzsch. *Carbon Nanotubes.* Wiley-VCH Verlag GmbH, Weinheim, Germany, January (2004).

[3] S. Das Sarma, Shaffique Adam, E. Hwang, and Enrico Rossi. *Reviews of Modern Physics* **83**(2), 407–470 May (2011).

[4] Yuanbo Zhang, Victor W. Brar, Caglar Girit, Alex Zettl, and Michael F. Crommie. *Nature Physics* **5**(10), 722–726 August (2009).

[5] Masa Ishigami, J H Chen, W G Cullen, M S Fuhrer, and E D Williams. *Nano letters* **7**(6), 1643–8 June (2007).

[6] A Fasolino, J H Los, and M I Katsnelson. *Nature materials* **6**(11), 858–61 November (2007).

[7] S. Das Sarma, Shaffique Adam, E. Hwang, and Enrico Rossi. *Reviews of Modern Physics* **83**(2), 407–470 May (2011).

[8] N Mermin and N Ashcroft. *Solid State Physics.* Saunders College, (1972).

[9] C W J Beenakker and H Van Houten. *Solid State Physics* **228**(1-2), 1–111 (1991).

[10] Sudip Chakravarty and Albert Schmid. *Physics Reports* **140**(4), 193–236 July (1986).

[11] S. V. Morozov, K. S. Novoselov, M. I. Katsnelson, F. Schedin, L. A. Ponomarenko, D. Jiang, and A. K. Geim. *Physical Review Letters* **97**(1), 016801 July (2006).

[12] E. McCann, K. Kechedzhi, Vladimir I. Falko, H. Suzuura, T. Ando, and B. L. Altshuler. *Physical Review Letters* **97**(14), 14–17 October (2006).

[13] Tsuneya Ando, Takeshi Nakanishi, and Riichiro Saito. *Journal of the Physics Society Japan* **67**(8), 2857–2862 August (1998).

[14] M. S. Dresselhaus and G. Dresselhaus. *Advances in Physics* **51**(1), 1–186 January (2002).

[15] F. V. Tikhonenko, D. W. Horsell, R. V. Gorbachev, and a. K. Savchenko. *Physical Review Letters* **100**(5), 056802 February (2008).

[16] D.W. Horsell, A.K. Savchenko, F.V. Tikhonenko, K. Kechedzhi, I.V. Lerner, and V.I. Falko. *Solid State Communications* **149**(27-28), 1041–1045 July (2009).

[17] P. Anderson, E. Abrahams, and T. Ramakrishnan. *Physical Review Letters* **43**(10), 718–720 September (1979).

[18] L.M. Malard, M.a. Pimenta, G. Dresselhaus, and M.S. Dresselhaus. *Physics Reports* **473**(5-6), 51–87 (2009).

[19] K S Novoselov, A K Geim, S V Morozov, D Jiang, Y Zhang, S V Dubonos, I V Grigorieva, and A A Firsov. *Science (New York, N.Y.)* **306**(5696), 666–9 (2004).

[20] Goki Eda, Giovanni Fanchini, and Manish Chhowalla. *Nature nanotechnology* **3**(5), 270–4 May (2008).

[21] Sergey Rumyantsev, Guanxiong Liu, Michael S Shur, Radislav A Potyrailo, and Alexander A Balandin. *Nano letters* **12**(5), 2294–8 May (2012).

[22] Yaping Dan, Ye Lu, Nicholas J Kybert, Zhengtang Luo, and A T Charlie Johnson. *Nano letters* **9**(4), 1472–5 April (2009).

[23] Ganhua Lu, Leonidas E Ocola, and Junhong Chen. *Nanotechnology* **20**(44), 445502 November (2009).

[24] F Schedin, a K Geim, S V Morozov, E W Hill, P Blake, M I Katsnelson, and K S Novoselov. *Nature materials* **6**(9), 652–5 September (2007).

[25] Z H Ni, H M Wang, J Kasim, H M Fan, T Yu, Y H Wu, Y P Feng, and Z X Shen. *Nano letters* **7**(9), 2758–63 September (2007).

[26] C. V. Raman and K. S. Krishnan. *Nature* **121**(3048), 501–502 March (1928).

[27] A. C. Ferrari, J. C. Meyer, V. Scardaci, C. Casiraghi, Michele Lazzeri, Francesco Mauri, S. Piscanec, Da Jiang, K. S. Novoselov, S. Roth, and A. K. Geim. *Physical Review Letters* **97**(18), 1–5 (2006).

[28] Zhen Hua Ni, Ting Yu, Yun Hao Lu, Ying Ying Wang, Yuan Ping Feng, and Ze Xiang Shen. *ACS Nano* **3**(2), 483–483 February (2009).

[29] a Ferrari. *Solid State Communications* **143**(1-2), 47–57 (2007).

[30] C. Casiraghi. *Energy* , 31–34 (2009).

[31] L G Cançado, A Jorio, E H Martins Ferreira, F Stavale, C A Achete, R B Capaz, M V O Moutinho, A Lombardo, T S Kulmala, and A C Ferrari. *Nano letters* **11**(8), 3190–6 August (2011).

[32] Alexander A Balandin, Suchismita Ghosh, Wenzhong Bao, Irene Calizo, Desalegne Teweldebrhan, Feng Miao, and Chun Ning Lau. *Nano letters* **8**(3), 902–7 (2008).

[33] Fabian M Koehler, Arnhild Jacobsen, Klaus Ensslin, Christoph Stampfer, and Wendelin J Stark. *Small (Weinheim an der Bergstrasse, Germany)* **6**(10), 1125–30 May (2010).

[34] Andrea C. Ferrari. *Solid State Communications* **143**(1-2), 47–57 July (2007).

[35] Roman V Gorbachev, Alexander S Mayorov, Alexander K Savchenko, David W Horsell, and Francisco Guinea. *Nano letters* **8**(7), 1995–9 July (2008).

[36] S. Morozov, K. Novoselov, M. Katsnelson, F. Schedin, D. Elias, J. Jaszczak, and A. Geim. *Physical Review Letters* **100**(1), 11–14 January (2008).

[37] A. Price, S.M Hornett, A. Shytov, E. Hendry, and D.W Horsell. *Physical Review B* **85**(16), 1–4 April (2012).

[38] Jian-Hao Chen, Chaun Jang, Shudong Xiao, Masa Ishigami, and Michael S Fuhrer. *Nature nanotechnology* **3**(4), 206–9 April (2008).

[39] S. Fratini and F. Guinea. *Physical Review B* **77**(19), 195415 May (2008).

[40] Amelia Barreiro, Michele Lazzeri, Joel Moser, Francesco Mauri, and Adrian Bachtold. *Physical review letters* **103**(7), 076601 August (2009).

[41] V. Kozub and A. Rudin. *Physical Review B* **52**(11), 7853–7856 September (1995).

[42] Wang-Kong Tse and S. Das Sarma. *Physical Review B* **79**(23), 235406 June (2009).

[43] R. Bistritzer and a.H. MacDonald. **78712**(4), 1–4 (2009).

[44] Gruneisen E. *Ann, Phys., Lpz* **16**(530) (1933).

[45] Dmitri K Efetov and Philip Kim. *Physical Review Letters* **105**(25), 256805 December (2010).

[46] C R Dean, A F Young, I Meric, C Lee, L Wang, S Sorgenfrei, K Watanabe, T Taniguchi, P Kim, K L Shepard, and J Hone. *Nature nanotechnology* **5**(10), 722–6 October (2010).

[47] V. Yu. Kashirin and Yu. F. Komnik. *Low Temp. Phys.* **20**(11), 902 (1994).

[48] E. Abrahams. *Physical Review Letters* **42**(10), 673–676 March (1979).

[49] Kaveh M, Uren M.J, Davies R.A, and Pepper M. *J. Phys. C* **14**, 413–419 (1981).

[50] F. V. Tikhonenko, A. A. Kozikov, A. K. Savchenko, and R. V. Gorbachev. *Physical Review Letters* **103**(22), 226801 November (2009).

[51] Z. Ovadyahu. *Physical Review B* **63**(23), 235403 May (2001).

[52] B. Altshuler, A. Aronov, and P. Lee. *Physical Review Letters* **44**(19), 1288–1291 May (1980).

[53] BL Altshuler and AG Aronov. *Electron-Electron Interaction in Disordered Conductors.* Elsevier Science Publishers, (1985).

[54] GY Hu and RF O'Connell. *Solid-state electronics* **32**(12), 1253–1257 (1989).

[55] Gerd Bergmann. *Zeitschrift fr Physik B Condensed Matter* **49**(2), 133–138 June (1982).

[56] Z Jiang, Y Zhang, Y Tan, H L Stormer, and P Kim. **143**, 14–19 (2007).

[57] Paul R. Grey, Paul J. Hurst, Stephen H. Lewis, and Robert G. Meyer. *Analysis and Design of Intergrated Circuits.* Wiley, New York, fifth ed. edition, (2009).

[58] A. A. Kozikov, D. W. Horsell, E. McCann, and V. I. Fal'ko. *Physical Review B* **86**(4), 045436 July (2012).

[59] Selman Hershfield and Vinay Ambegaokar. *Physical Review B* **34**(4), 2147–2151 August (1986).

[60] G Hu and R Oconnell. *Physica A: Statistical Mechanics and its Applications* **153**(1), 114–128 November (1988).

[61] K. Kechedzhi, D. W. Horsell, F. V. Tikhonenko, A. K. Savchenko, R. V. Gorbachev, I. V. Lerner, and V. I. Falko. *Physical Review Letters* **102**(6), 066801 February (2009).

[62] Yu. Kashirin, F Komnik, and V Yu. *Low Temp. Phys.* **20**(12), 983 (1994).

[63] Ryan W. Newson, Jesse Dean, Ben Schmidt, and Henry M. van Driel. *Optics Express* **17**(4), 2326 February (2009).

[64] Xingquan Zou, Da Zhan, Xiaofeng Fan, Dongwook Lee, Saritha K. Nair, Li Sun, Zhenhua Ni, Zhiqiang Luo, Lei Liu, Ting Yu, Zexiang Shen, and Elbert E. M. Chia. *Applied Physics Letters* **97**(14), 141910 (2010).

[65] Daniele Brida, Cristian Manzoni, Giulio Cerullo, Andrea Tomadin, Marco Polini, Rahul R. Nair, Andre K. Geim, Kostya S. Novoselov, Silvia Milana, Andrea Lombardo, and Andrea C. Ferrari. In *Conference on Lasers and Electro-Optics 2012*, QTh3H.1. Optical Society of America, May (2012).

[66] M. Breusing, S. Kuehn, T. Winzer, E. Malić, F. Milde, N. Severin, J. P. Rabe, C. Ropers, A. Knorr, and T. Elsaesser. *Physical Review B* **83**(15), 153410 April (2011).

[67] Jahan M. Dawlaty, Shriram Shivaraman, Mvs Chandrashekhar, Farhan Rana, and Michael G. Spencer. *Applied Physics Letters* **92**(4), 042116 (2008).

[68] Brian A. Ruzicka, Lalani K. Werake, Hui Zhao, Shuai Wang, and Kian Ping Loh. *Applied Physics Letters* **96**(17), 173106 (2010).

[69] Chun Hung Lui, Kin Fai Mak, Jie Shan, and Tony F. Heinz. *Physical Review Letters* **105**(12), 127404 September (2010).

[70] Haining Wang, Jared H. Strait, Paul a. George, Shriram Shivaraman, Virgil B. Shields, Mvs Chandrashekhar, Jeonghyun Hwang, Farhan Rana, Michael G. Spencer, Carlos S. Ruiz-Vargas, and Jiwoong Park. *Applied Physics Letters* **96**(8), 081917 (2010).

[71] Libai Huang, Bo Gao, Gregory Hartland, Michelle Kelly, and HuiLi Xing. *Surface Science* **605**(17-18), 1657–1661 September (2011).

[72] P. Hale, S. Hornett, J. Moger, D. Horsell, and E. Hendry. *Physical Review B* **83**(12), 121404 March (2011).

[73] Farhan Rana, Paul a. George, Jared H. Strait, Jahan Dawlaty, Shriram Shivaraman, Mvs Chandrashekhar, and Michael G. Spencer. *Physical Review B* **79**(11), 1–5 (2009).

[74] Haining Wang, Jared H. Strait, Paul A. George, Shriram Shivaraman, Virgil B. Shields, Mvs Chandrashekhar, Jeonghyun Hwang, Farhan Rana, Michael G. Spencer, Carlos S. Ruiz-Vargas, and Jiwoong Park. *Applied Physics Letters* **96**(8), 081917 (2010).

[75] Callum J Docherty, Cheng-Te Lin, Hannah J Joyce, Robin J Nicholas, Laura M Herz, Lain-Jong Li, and Michael B Johnston. *Nature communications* **3**, 1228 January (2012).

[76] Markus Breusing, Claus Ropers, and Thomas Elsaesser. *Physical Review Letters* **102**(8), 086809 February (2009).

[77] B. Y. Sun, Y. Zhou, and M. W. Wu. *Physical Review B* **85**(12), 125413 March (2012).

[78] Xian-Fu Zhang and Qian Xi. *Carbon* **49**(12), 3842–3850 October (2011).

[79] Zhong De Liu, Heng Xin Zhao, and Cheng Zhi Huang. *PloS one* **7**(12), e50367 January (2012).

[80] F.-J. Kao, D. G. Busch, D. Cohen, D. Gomes da Costa, and W. Ho. *Physical Review Letters* **71**(13), 2094–2097 September (1993).

[81] C. Hess, S. Funk, M. Bonn, D.N. Denzler, M. Wolf, and G. Ertl. *Applied Physics A: Materials Science & Processing* **71**(5), 477–483 November (2000).

[82] Yoshiaki Sato, Kazuyuki Takai, and Toshiaki Enoki. *Nano letters* **11**(8), 3468–75 August (2011).

[83] R. Arsat, M. Breedon, M. Shafiei, P.G. Spizziri, S. Gilje, R.B. Kaner, K. Kalantar-zadeh, and W. Wlodarski. *Chemical Physics Letters* **467**(4-6), 344–347 January (2009).

[84] E. H. Hwang, S. Adam, and S. Das Sarma. *Physical Review B* **76**(19), 195421 November (2007).

[85] Tim O. Wehling, Alexander I. Lichtenstein, and Mikhail I. Katsnelson. *Applied Physics Letters* **93**(20), 202110 (2008).

[86] Sunmin Ryu, Li Liu, Stephane Berciaud, Young-jun Yu, Haitao Liu, Philip Kim, George W Flynn, and Louis E Brus. *Nano letters* , 10–13 November (2010).

[87] Yinxiao Yang and Raghu Murali. *Applied Physics Letters* **98**(9), 093116 (2011).

[88] Kin Fai Mak, Chun Hung Lui, and Tony F. Heinz. *Applied Physics Letters* **97**(22), 221904 (2010).

[89] S. Heinze, J. Tersoff, R. Martel, V. Derycke, J. Appenzeller, and Ph. Avouris. *Physical Review Letters* **89**(10), 106801 August (2002).

[90] P. Giannozzi, R. Car, and G. Scoles. *The Journal of Chemical Physics* **118**(3), 1003 (2003).

[91] Adam Roberts, Daniel Cormode, Collin Reynolds, Ty Newhouse-Illige, Brian J. LeRoy, and Arvinder S. Sandhu. *Applied Physics Letters* **99**(5), 051912 (2011).

[92] Marc Currie, Joshua D. Caldwell, Francisco J. Bezares, Jeremy Robinson, Travis Anderson, Hayden Chun, and Marko Tadjer. *Applied Physics Letters* **99**(21), 211909 (2011).

[93] Christian Frischkorn, Martin Wolf, Ulrich Hofer, Jens Gudde, Peter Saalfrank, Mathias Nest, Tillmann Klamroth, Frank Willig, Ralph Ernstorfer, Lars Gundlach, Volkhard May, Luxia Wang, Walter R. Duncan, and Oleg V. Prezhdo. In *Analysis and Control of Ultrafast Photoinduced Reactions,* O Kühn and L Wöste, editors, chapter 5, 387–484. Springer Berlin-Heidelberg (2007).

[94] J.W. Gadzuk, L.J. Richter, S.A. Buntin, D.S. King, and R.R. Cavanagh. *Surface Science* **235**(2-3), 317–333 September (1990).

[95] J.M Gottfried, K.J Schmidt, S.L.M Schroeder, and K Christmann. *Surface Science* **525**(1-3), 184–196 February (2003).